Development and characterization of piezoelectric AlScN-based alloys for electroacoustic applications

Yuan Lu

Dissertation zur Erlangung des Doktorgrades der

Technischen Fakultät der

Albert-Ludwigs-Universität Freiburg im Breisgau

2019

Dekanin

Prof. Dr. Hannah Bast

Referenten

Prof. Dr. Oliver Ambacher

Prof. Dr. Michael Fiederle

Datum der Promotion

21.05.2019

Erklärung

Ich erkläre, dass ich die vorliegende Arbeit ohne unzulässige Hilfe Dritter und ohne Benutzung anderer als der angegebenen Hilfsmittel angefertigt habe. Die aus anderen Quellen direkt oder indirekt übernommenen Daten und Konzepte sind unter Angabe der Quelle gekennzeichnet. Insbesondere habe ich hierfür nicht die entgeltliche Hilfe von Vermittlungs- oder Beratungsdiensten (Promotionsberaterinnen oder Promotionsberater oder anderer Personen) in Anspruch genommen. Niemand hat von mir unmittelbar oder mittelbar geldwerte Leistungen für Arbeiten erhalten, die im Zusammenhang mit dem Inhalt der vorgelegten Dissertation stehen. Die Arbeit wurde bisher weder im In- noch im Ausland in gleicher oder ähnlicher Form einer anderen Prüfungsbehörde vorgelegt.

Ich erkläre hiermit, dass ich mich noch nie an einer in- oder ausländischen wissenschaftlichen Hochschule um die Promotion beworben habe oder gleichzeitig bewerbe.

Yuan Lu

Freiburg im Breisgau, den 30. Januar 2019

Abstract

The mobile communication standard of the 5th generation (5G) is nowadays a great technological innovation for both industry and consumers. To meet the requirement of higher data rates in 5G, a higher electromechanical coupling of electro-acoustic devices is needed. One of the most successful piezoelectric materials in electro-acoustic applications is aluminum nitride (AlN). However, AlN-based devices have a rather low piezoelectric coefficient d_{33} = 5.5 pC/N, and the electromechanical coupling of AlN is limited to 7%. These parameters can be significantly enhanced by incorporating scandium (Sc) in the wurtzite structure AlN, making AlScN a promising material for future mobile communication applications.

This work aims at the development of wurtzite AlScN thin films with homogenous microstructure, high crystalline quality and high Sc-concentration (x > 0.4) to achieve a large piezoelectric coefficient and electromechanical coupling in electro-acoustic resonators.

Therefore, $Al_{1-x}Sc_xN$ thin films on Si(001) substrates were grown by reactive DC-pulsed magnetron co-sputtering, which is capable of adjusting the Sc-concentration. By tuning process pressure and target-to-substrate distance, AlN thin film with straight columnar microstructure along substrate normal was achieved, which served as a reference for sputtering AlScN films. Replacing Al by Sc degraded the crystal quality and resulted in misoriented grains and localized non-piezoelectric areas. Optimized gas ratio eliminated misoriented grains and enabled the growth of a homogenous piezoelectric phase, maximizing the piezoelectric coefficient at Sc concentration x = 0.13. Later on, the Sc concentration was further increased without phase separation. Finally, a state-of-the-art $Al_{0.54}Sc_{0.46}N$/Si thin film was synthesized with columnar microstructure, excellent crystalline quality (FWHM $< 2°$) and high piezoelectric coefficient of d_{33} = 44 pC/N. Furthermore, epitaxial $Al_{1-x}Sc_xN$ ($0 \leq x \leq 0.46$) thin films were also synthesized on Al_2O_3(0001) substrates.

The mechanical and optical properties of AlScN/Al_2O_3 samples were thoroughly analyzed. The elastic modulus E and the coefficient of thermal expansion α were experimentally determined by thermal-cycling up to 400°C. The sample with a composition of $Al_{0.59}Sc_{0.41}N$ showed E = 270 GPa and $\alpha = 4.29 \times 10^{-6}$ K^{-1}, respectively. The evolution of the band gap in higher Sc concentration was determined by spectroscope ellipsometry, indicating the band gap can be tuned from 5.8 eV in AlN to 4.4 eV in $Al_{0.59}Sc_{0.41}N$, which makes AlScN also promising material in the optoelectronics.

Finally, AlScN-based surface acoustic wave (SAW) resonators were fabricated and an effective electromechanical coupling of 2.2% at around 2 GHz could be obtained for $Al_{0.68}Sc_{0.32}N$-based resonators, more than 4 times higher compared to the 0.5% of conventional AlN-resonators. The enhanced piezoelectric coefficient and electromechanical coupling underlined the outstanding quality of AlScN and its huge potential in electro-acoustic applications.

Kurzfassung

Der Mobilfunkstandard der 5. Generation (5G) ist in der heutigen Zeit sowohl für die Industrie wie auch die Verbraucher eine wichtige technologische Innovation. Um die Voraussetzungen der hohen Datenraten von 5G zu erfüllen, wird eine höhere elektronisch-mechanischer Kopplung der elektroakustischen Bauteile benötigt. Eines der erfolgreichsten piezoelektrischen Materialien in elektroakustischen Anwendungen ist Aluminiumnitrid (AlN). Bauteile, welche auf AlN basieren, besitzen jedoch eine relativ niedrige piezoelektrischen Koeffizienten d_{33} = 5,5 pC/N und die elektromechanische Kopplung ist auf 7% beschränkt. Durch den Einbau von Scandium (Sc) in die wurtzitische Phase des AlN lassen sich diese Parameter signifikant erhöhen und machen AlScN zu einem vielversprechenden Material in zukünftigen Anwendungen der mobilen Kommunikation.

Diese Arbeit zielt auf die Entwicklung von wurtzitischem AlScN Dünnschichten ab, welche mit einer homogenen Mikrostruktur, hoher kristalliner Qualität und Sc-Konzentration (x > 0,4) einen großen piezoelektrischen Koeffizienten und elektromechanische Kopplung in elektroakustischen Bauteilen erreichen sollen.

Hierfür wurden $Al_{1-x}Sc_xN$ Dünnschichten auf Si(001) Substrate mittels reaktivem DC-gepulstem Magnetron-Co-Sputtern gewachsen, welches ein Einstellen der Sc-Konzentration erlaubt. Durch eine Anpassung des Prozessdrucks sowie der Abstand zwischen Target und Substrat, konnten AlN Dünnschichten mit einer senkrecht zur Substratnormalen ausgebildeten kolumnaren Mikrostruktur gezüchtet werden, die als hervorragende Referenz für das AlScN-Wachstum dienten. Der Austausch von Al durch Sc führt jedoch zu einer Degradation der Kristallqualität und im Weiteren zu fehlorientierten Körnern und lokalen Bereichen ohne piezoelektrische Eigenschaften. Optimierte Verhältnisse zwischen den Prozessgasen eliminierte die Fehlorientierung der Körner und ermöglichte das Wachstum einer homogenen piezoelektrischen Phase, welche bei einer Zusammensetzung von x = 0,13 einen maximalen piezoelektrischen Koeffizienten $d_{33,clamp}$ = 12,3 pC/N aufwies. Im weiteren Verlauf der Arbeit konnte die Sc-Konzentration ohne Phasenseparation weiter erhöht werden. Dies resultierte in einer state-of-the-art $Al_{0.54}Sc_{0.46}N$ Dünnschicht auf Silizium, welche eine kolumnare Mikrostruktur, exzellente Kristallqualität (FWHM < 2°) und einen hohen piezoelektrischen Koeffizienten mit d_{33} = 44 pC/N aufwies. Zusätzlich wurden epitaktische Dünnschichten mit $Al_{1-x}Sc_xN$ ($0 \leqslant x \leqslant 0.46$) auf Al_2O_3(0001) aufgewachsen.

Die mechanischen und optischen Eigenschaften von AlScN/Al_2O_3 Proben wurden eingehend analysiert. Das Elastizitätsmodul E und der thermische Ausdehnungskoeffizient α wurden experimentell durch thermische zyklische Belastung bis 400 °C bestimmt, welche bei einer Zusammensetzung von $Al_{0.59}Sc_{0.41}N$ in E = 270 GPa und $\alpha = 4{,}29 \times 10^{-6}\ K^{-1}$ resultierte. Die Abhängigkeit der Bandlücke von der Sc-Konzentration wurde über spektroskopische Ellipsometrie bestimmt. Diese zeigte eine Einstellbarkeit der Bandlücke von 5,8 eV für AlN zu 4,4 eV in $Al_{0.59}Sc_{0.41}N$, welches AlScN auch für optoelektronische Anwendungen interessant macht.

Zuletzt wurden AlScN-basierte elektronische Bauteile hergestellt, sogenannte *surface acoustic wave* (SAW) *resonators*, die eine effektive elektromechanische Kopplung von 2.2% bei etwa 2 GHz und einer

Zusammensetzung von $Al_{0.68}Sc_{0.32}N$ besaßen. Dies entspricht einer Erhöhung von mehr als dem 4-fachen im Vergleich zu den 0,5% in konventionellen AlN-Bauteilen. Der verbesserte piezoelektrische Koeffizient und die elektromechanische Kopplung unterstreichen die herausragende Qualität von AlScN und sein immenses Potential für den Einsatz in elektroakustischen Anwendungen.

Publications

Some ideas, results, and figures have been published previously in the following publications:

1. **Y. Lu,** M. Reusch, N. Kurz, A. Ding, T. Christoph, L. Kirste, V. Lebedev, and A. Žukauskaitė, Surface morphology and microstructure of pulsed DC magnetron sputtered piezoelectric AlN and AlScN thin films, Physica Status Solidi (A). 215, 1700559 (2018).
2. **Y. Lu,** M. Reusch, N. Kurz, A. Ding, T. Christoph, M. Prescher, L. Kirste, O. Ambacher, and A. Žukauskaitė, Elastic modulus and coefficient of thermal expansion of piezoelectric $Al_{1-x}Sc_xN$ (up to x = 0.41) thin films, APL Mater. 6, 076105 (2018).
3. A. Ding, M. Reusch, **Y. Lu**, N. Kurz, R. Lozar, T. Christoph, R. Driad, O. Ambacher, and A. Žukauskaitė, Investigation of Temperature Characteristics and Substrate Influence on AlScN-Based SAW Resonators, in 2018 IEEE Int. Ultrason. Symp. (IEEE, Kobe, 2018), pp. 1–9.

Table of contents

1 Introduction 1

1.1 Motivation 1

1.2 The aim of this work 3

1.3 Outline 4

2 Piezoelectric AlScN thin films for electro-acoustic applications 7

2.1 Piezoelectricity 7

2.2 Aluminum scandium nitride, a novel piezoelectric material 10

2.3 Sputter deposition 15

2.4 Growth mechanism 16

2.5 Sample preparation and sputtering procedure 19

3 Characterization methods 21

3.1 X-ray diffraction (XRD) 21

3.2 Scanning electron microscopy (SEM) 25

3.3 Atomic force microscopy (AFM) 27

3.4 Berlincourt method 30

3.5 Raman spectroscopy 31

3.6 Spectroscopic ellipsometry (SE) 32

3.7 Summary 35

4 AlN thin film deposition 37

4.1 Influence of the process pressure 37

4.2 Influence of the target-to-substrate distance (TSD) 44

4.3 Influence of the N_2 concentration (N_2 / (Ar + N_2)) 49

4.4 Summary 53

5 AlScN thin film deposition 55

5.1 Abnormal grains in AlScN 55

5.2 Sc concentration variation 63

5.3 AlScN on Al_2O_3 (0001) substrates 70

5.4 Discussion and summary 74

6 Mechanical and optical properties of AlScN 75
6.1 Elastic modulus and coefficient of thermal expansion 75
6.2 Phonon modes 79
6.3 Band gap of AlScN 83
6.4 Summary 84
7 AlScN based SAW resonators 87
7.1 Results and discussion 90
7.2 Summary 91
8 Conclusion and outlook 93
8.1 Conclusion 93
8.2 Outlook 94
References 97
Publications 113
Journal papers related to this work 113
Conference contributions 113
Acknowledgements 115

1 Introduction

1.1 Motivation

Since 60 years ago, electro-acoustic devices have been used in the telecommunication industry, such as surface acoustic wave (SAW) resonators, in which they are acting as bandpass filters in radio frequency (RF) and intermediate frequency (IF) section [1]. Nowadays, due to the increasing requirement of the multiple frequency bands in the worldwide, including LTE (long time evolution), CDMA (code division multiple access), UMTS (universal mobile telecommunications service) or the 5G (5th generation) bands in the future, the cellular filter market reached 7.700 billion US dollars in 2017 and is predicted to reach more than 20 billion in 5 years. The market volume is increased from less than 40 billion units up to 65 billion units in 2023, as predicted (Figure 1-1). The electro-acoustic devices are facing new challenges because of the upcoming standards of telecommunication, e.g., smaller size; higher conversion efficiency; better thermal management; higher frequency to meet the requirements of the 5G band standards and data exchange speed.

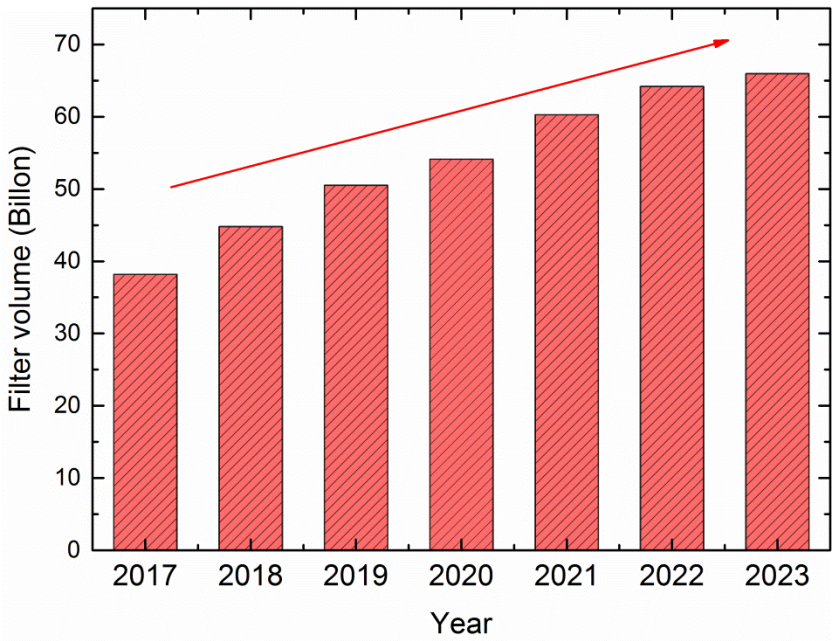

Figure 1-1 The market volume of the RF filter by the cellular band standard and the Wi-Fi standard, analysis and estimated by Yole [2].

The electro-acoustic resonators are the transducers that convert between electrical charge and mechanical movement in the acoustic waves. In Figure 1-2 the structure of the SAW resonator is shown, on the substrate the thin film piezoelectric material is deposited. The interdigital transducer (IDT) and reflectors are normally made from metal to excite or sense the surface acoustic wave, the wavelength of the wave λ is defined by the width of the IDT. Due to the piezoelectric effect, the acoustic wave is generated in the piezoelectric material. The common piezoelectric materials used in the sensor applica-

tion are: quartz (SiO_2), lithium tantalite ($LiTaO_3$) and aluminum nitride (AlN), other materials such as GaAs, SiC, ZnO, PZT, $LiNbO_3$ have also the commercial potential [1].

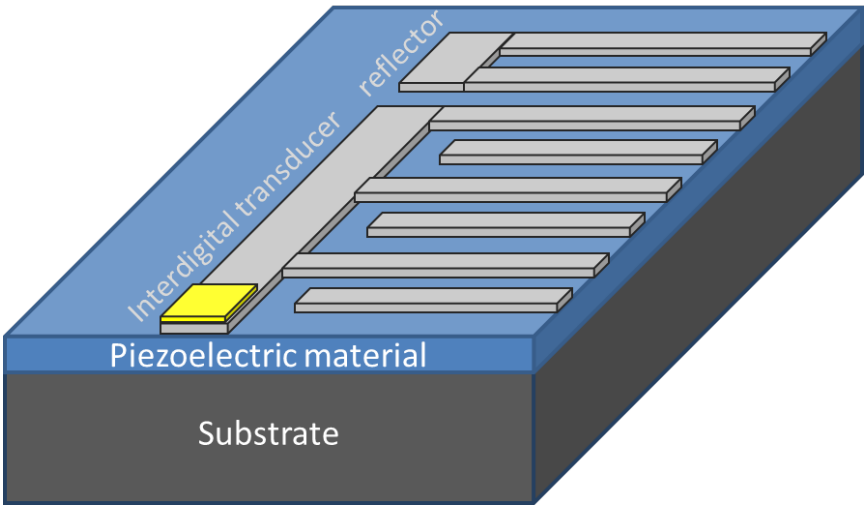

Figure 1-2 Schematic figure of the surface acoustic wave resonator

The electromechanical coupling coefficient is defining the filter bandwidth and thus influences the data exchange speed of the resonators. As shown in Equation 1-1, the coupling coefficient k_t^2 is directly correlated to the piezoelectric stress coefficient e_{33}^2, relative stiffness constant c_{33}^D and relative dielectric constant ε_{33}^2, therefore, improving the electromechanical coupling is to increase the piezoelectric stress coefficient or decrease stiffness constant and dielectric constant.

$$k_t^2 = e_{33}^2/(c_{33}^D \varepsilon_{33}^S) \qquad 1\text{-}1$$

There are many factors to influence the electromechanical coupling of the resonator, such as choice of metal contact, operating frequency and piezoelectric material. In this work, the focus is on the piezoelectric materials. To quantify the piezoelectric effect, the piezoelectric coefficient d_{33} is used and expressed as follow:

$$d_{33} = e_{33}/c_{33}^E \qquad 1\text{-}2$$

where e_{33} is piezoelectric stress coefficient and c_{33}^E is relative stiffness constant. The piezoelectric AlN draws a lot of attention for the researchers and the industry, due to the advantage of the stability of the growth method and the performance of AlN-based RF resonators. For the piezoelectric properties, the AlN is usually with c-axis crystallographic orientation by reactive sputtering. This process is also applicable on the Si substrates so that most of the existing fabrication tools for the Si technology can be utilized, which enables a smaller package size of the device chips. The BAW devices based on AlN thin films could guarantee an effective electromechanical coupling coefficient k_{eff}^2 (combination of material and device design) about 6% and material electromechanical coupling k_t^2 about 6.8%, which indicates a conversion coefficient between mechanical and electrical signal. The phase velocity of the AlN is also as high as 10600 m/s. In contrast, ZnO as another piezoelectric material has a higher coupling coefficient, but it has lower phase velocity and is not compatible with the Si technology.

It was shown recently, that the incorporation of Sc into AlN allows an increase up to 400% of the piezoelectric coefficient d_{33} [3]. Moreover, the material electromechanical coupling k_t^2 of the $Al_{1-x}Sc_xN$ is expected to have 200% increase with Sc concentration x = 0.3 [4]. The piezoelectric AlScN will remain the same hexagonal wurtzite structure as AlN with c-axis orientation up to x = 0.5 [5], so that it benefits from almost all the advantage of AlN. These facts make AlScN as a perfect alternative of AlN in the electro-acoustic applications. Therefore, the work to synthesize the AlScN thin films and adjust the process parameter to fit the electro-acoustic devices is of high interest.

1.2 The aim of this work

As already mentioned, AlScN is a novel material for next-generation transducers due to its high piezoelectric response and electromechanical coupling. However, replacing Al atoms with Sc atoms leads to the softening of the material and a distortion of the hexagonal atomic structure [5]; the metastability of AlScN will cause microstrucutre defects and inhomogenous piezoelectric domains, even phase separation.

This dissertation is aimed to develop wurtzite $Al_{1-x}Sc_xN$ thin films with homogenous microstructure and high crystalline quality up to Sc concentration x = 0.46, to achieve a high piezoelectric response and electromechanical coupling in electro-acoustic resonators. The three key words in the goal-microstructure, crystalline quality, and high piezoelectric response are discussed in detail:

Microstructure:

The sputtered piezoelectric AlN thin film is normally with columnar microstructure [6,7], when it is grown as highly c-axis oriented hexagonal wurtzite crystal structure. Considering the piezoelectric polarization is contributed by each individual grains, the direction of the grains has to be well aligned to substrate normal direction for maximum piezoelectric polarization. In this Ph.D. work, a new magnetron co-sputtering setup was used for all of the depositions, the first step was to find process window to obtain piezoelectric AlN thin film with columnar microstructure towards substrate normal.

Crystalline quality:

Crystalline quality here refers to crystal orientation and crystal structure. Misoriented grains in AlN and AlScN [8–10] are not only causing roughness and thus wave attenuation in the SAW devices, but also reduce the piezoelectric response and electromechanical coupling in the device. $Al_{1-x}Sc_xN$ was reported to have cubic phase when the Sc concentration is more than x = 0.5, leading a huge influence of piezoelectric response [3]. In this dissertation, the goal is to have wurtzite $Al_{1-x}Sc_xN$ thin film with c-axis orientation.

Piezoelectric response:

It was reported that the metal-polar and N-polar could co-exist and influence piezoelectric response [11]. Therefore, a homogenous piezoelectric phase should also be investigated.

At last, the fabrication and characterization of the AlScN-based resonators provides a better view of a novel material in the electro-acoustic applications compared to AlN. Through the resonance frequency

and electromechanical coupling of the AlScN-based resonators, further improvements concerning material deposition as well as the device design can be guided.

1.3 Outline

The topic of the dissertation is: Development and characterization of piezoelectric AlScN-based ternary alloys for electroacoustic applications. In the first chapter, the introduction and aim of the work are presented.

Chapter 2 is focusing on the materials AlN and AlScN, the research background and state-of-the-art. The sputtering deposition method and mechanism are discussed. In this part, the basics of reactive pulsed-DC magnetron co-sputtering are illustrated. The growth mechanism, especially the evolution of structure zone model, is introduced due to the importance in the optimization: The theory of the structural zone model is essentially guiding the optimization of the sputtering deposition with crystal microstructure, and also a foundation of the models illustrated in Chapter 4. Lastly the sputtering equipment used to deposit AlN and AlScN thin films is discussed.

Chapter 3 explains the characterization methods used for process optimization to determine other material properties of AlScN. Characterizations such as X-ray diffraction, scanning electron microscopy, Belincourt method are introduced and their mechanism is discussed.

Chapter 4 and Chapter 5 present the most important parts in this work: Chapter 4 is focused on optimization of AlN sputtering process. The piezoelectric AlN thin film shares the same hexagonal wurtzite structure as piezoelectric AlScN, sputtering recipe of high-quality thin film AlN is also an important reference for AlScN. In Chapter 4, AlN/Si thin film sputtering with sample series of different process pressure, target-to-sample distance (TSD) and N_2 gas concentration are discussed in detail. The optimizations are concentrated on the crystalline quality and microstructure, which are also the important factors for the piezoelectric AlN thin films. Models of the microstructure evolution with the process pressure and TSD are established to guide the growth of AlScN in the following part.

Chapter 5 is mainly focused on the AlScN. In this chapter, the piezoelectric response is the most important parameter of the sputtered AlScN thin films. The goal is achieved by reducing the misoriented grains and sputtering of high crystalline quality AlScN up to Sc concentration $x = 0.46$. First the misoriented grains were observed during the sputtering of AlN and AlScN, the mapping of piezoelectric domain indicated its influence on the piezoelectric response. The systematic study of N_2 gas concentration and TSD eliminated the misoriented grains. Homogenous surface morphology, as well as piezoelectric domains were obtained, piezoelectric response for Sc concentration $x = 0.13$ were maximized. Besides, this work has been published as one of the first publications to detect and solve the misoriented grains in AlScN. Second, AlScN thin films with Sc concentration up to $x = 0.46$ were sputtered. Phase instability issues were first observed when the Sc concentration is up to $x > 0.4$, by optimizing the heater temperature c-axis oriented hexagonal wurtzite $Al_{0.54}Sc_{0.46}N$/Si were achieved. The piezoelectric response of the sputtered thin films was comparable or even higher than the state-of-the-art AlScN. Last but not the least, the process of AlScN/Al_2O_3 was established and crack issue caused by the high stress in the as-deposited films was solved, the sputtered AlScN is observed to have an epitaxial relationship to the c-plane Al_2O_3. As a result, the optimized sputtering process for highly

c-axis oriented, AlScN/Si and AlScN/Al_2O_3 with homogenous microstructure up to x = 0.46 was established.

Chapter 6 introduces the characterization of the mechanical and optical properties of the AlScN. Elastic modulus and CTE of AlScN (Sc concentration up to x = 0.4) were analyzed by thermal cycling up to 400°C. Another part of this chapter is the optical measurement, Raman spectroscopy and spectroscopy ellipsometry were used to determine the phonon modes and the reflectance of the AlScN/Al_2O_3, and preliminary results are discussed in this part.

Chapter 7 demonstrates the SAW resonators based on AlScN/Si thin film. The crystalline quality of the AlScN grown on the high resistivity Si(001) wafers was investigated. AlScN-based SAW resonators with resonance frequency up to 2 GHz was fabricated, electromechanical coupling was compared between AlN and $Al_{0.68}Sc_{0.32}N$.

Chapter 8 summarizes the whole work presented in this dissertation and gives a short outlook of the future direction of the research, including other AlN based ternary alloys for electro-acoustic applications, the combination of AlScN thin films with graphene electrodes, and the integration in other electro-acoustic resonators to reach the higher resonance frequencies.

2 Piezoelectric AlScN thin films for electro-acoustic applications

This chapter is discussing the theoretical background of the piezoelectric material AlScN and the deposition method of thin film AlScN. It starts with the principle of the piezoelectric effect, as the most important property of AlScN and basic in the electro-acoustic applications. A detailed explanation of these piezoelectric components is necessary for understanding the correlation of these components and the conditions of measured values, which will be used in the deposition optimization of the sputtered AlScN, characterization of the AlScN thin films, and the AlScN-based resonators.

Following the piezoelectricity and piezoelectric materials, the physical properties of AlN, ScN and AlScN are introduced. In this part the physical parameters and the theoretical background of the material AlN and ScN are explained; the mechanism of piezoelectric coefficient increase, the research progress and state-of-the-art of the AlScN are also included in this part. Afterwards, the theory of magnetron sputtering and the growth mechanism from nucleation to the evolving of the microstructure are discussed in detail, the relationship between the kinetic energy of the sputtering species and microstructure of the deposited film helps the optimization of the sputtering process.

2.1 Piezoelectricity

The piezoelectric effect is defined as "the electric field or electric polarization is produced by pressure." or "the material is deformed when in an electric field", these phenomena were describing the direct effect and the converse effect, respectively. In 1880, the piezoelectricity was initiated as a research field in crystal physics by brothers Curie, the temperature at which material losses the ferroelectric properties is also called Curie temperature [12]. They discovered the tension and compression generated electric field are proportional to the applied load, and Hankel named it piezoelectric effect [13]. Voigt described later the crystal classes which is correlated to the piezoelectricity using tensor analysis [14]. When the applied stress or load is applied on the piezoelectric material, the polarization P could be expressed mathematically as:

$$P = d_{ijk}\sigma_{jk} \tag{2-1}$$

Here the d_{ijk} and σ are defined as the piezoelectric coefficient (or piezoelectric modulus in some literature) and stress tensor, respectively. The indices i, j, k stand for the components of the tensor. Since the piezoelectricity is the third-rank tensor, the 27 components make the piezoelectric coefficient cubic array of 3 by 3. A Voigt notation is introduced to simplify the tensor components [14]:

Tensor (*jk*)	11	22	33	23, 32	13, 31	12, 21
Voigt (*k*)	1	2	3	4	5	6

As the tensor $\sigma_{111} = \sigma_1$, but the $2\sigma_{123} = \sigma_{14}$, which should be noticed. According to the Voigt notation, Equation 2-1 is derived as:

$$\begin{pmatrix} P_1 \\ P_2 \\ P_3 \end{pmatrix} = \begin{pmatrix} d_{11} & d_{12} & d_{13} & d_{14} & d_{15} & d_{16} \\ d_{21} & d_{22} & d_{23} & d_{24} & d_{25} & d_{26} \\ d_{31} & d_{32} & d_{33} & d_{34} & d_{35} & d_{36} \end{pmatrix} \cdot \begin{pmatrix} \sigma_1 \\ \sigma_2 \\ \sigma_3 \\ \sigma_4 \\ \sigma_5 \\ \sigma_6 \end{pmatrix}. \quad 2\text{-}2$$

From the matrix above, it is more compact than the previous tensor notation in 2-1. As the direct effect of the piezoelectricity is already discussed previously, the converse effect it is expressed as:

$$\epsilon_{jk} = d_{ijk} E_i \quad 2\text{-}3$$

Here the ϵ is the strain tensor and the E is the electric field, this equation is to describe the shape change when the piezoelectric material is placed in an electric field, and it is a thermodynamic consequence of the direct effect.

To simplify the tensor notation, the Voigt notation is also used to reduce the order of the ϵ_{ij} and d_{ijk}:

$$\begin{pmatrix} \epsilon_1 \\ \epsilon_2 \\ \epsilon_3 \\ \epsilon_4 \\ \epsilon_5 \\ \epsilon_6 \end{pmatrix} = \begin{pmatrix} d_{11} & d_{21} & d_{31} \\ d_{12} & d_{22} & d_{32} \\ d_{13} & d_{23} & d_{33} \\ d_{14} & d_{24} & d_{34} \\ d_{15} & d_{25} & d_{35} \\ d_{16} & d_{26} & d_{36} \end{pmatrix} \cdot \begin{pmatrix} E_1 \\ E_2 \\ E_3 \end{pmatrix}. \quad 2\text{-}4$$

However, the piezoelectric coefficient tensor d_{33} in the 2-4 still has 18 components. To further reduce the components, symmetry of the piezoelectric material is considered: for example, the hexagonal wurtzite AlN has space group P63mc, which is in the class of the 6mm, the d_{ij} matrix in the direct effect piezoelectricity could be simplified as:

$$d_{ij} = \begin{pmatrix} 0 & 0 & 0 & 0 & d_{15} & 0 \\ 0 & 0 & 0 & d_{15} & 0 & 0 \\ d_{31} & d_{31} & d_{33} & 0 & 0 & 0 \end{pmatrix}. \quad 2\text{-}5$$

In the matrix, the $d_{31} = d_{32}$ and $d_{24} = d_{15}$, therefore they exist two times. Here the indices 1….6 stands for the direction of the a-axis(indices 1), b-axis(indices 2), c-axis(indices 3), shear about a-axis(indices 4), shear about b-axis(indices 5) and shear about c-axis(indices 6). In the piezoelectric coefficient d_{ij}, i stands for the direction of the polarization, and j stands for the direction of the strain: e.g. the d_{33} indicating the induced polarization along the c-axis by the stress applied on the c-axis.

However, the direct and converse effects are indicating the case, where the external electric field or the stress is zero. Normally, the piezoelectricity is described in piezoelectric constitutive equations in a strain-charge form [15]:

$$\begin{aligned} D &= d_{ij}\sigma_j + \xi_{ij}^{\sigma}E_i \\ \epsilon_{jk} &= S_{ij}^{E} + d_{ij}E_i \end{aligned} \qquad 2\text{-}6$$

and stress-charge form:

$$\begin{aligned} D &= e_{ij}\epsilon_j + \xi_{ij}^{\epsilon}E_i \\ \epsilon_{jk} &= C_{ij}^{E} + e_{ij}E_i \end{aligned} \qquad 2\text{-}7$$

In the strain form, D is the dielectric displacement, ξ_{ij}^{σ} indicates the relative permittivity under constant stress, S_{ij}^{E} stands for the material compliance; while in the stress form, ξ_{ij}^{ϵ} indicates the relative permittivity under constant strain, C_{ij}^{E} stands for the material stiffness.

The stiffness C and the material compliance S are the elastic properties of the material, for the hexagonal material, the order is reduced because of the symmetry:

$$C_{ij} = \begin{pmatrix} C_{11} & C_{12} & C_{13} & 0 & 0 & 0 \\ C_{12} & C_{11} & C_{13} & 0 & 0 & 0 \\ C_{13} & C_{13} & C_{33} & 0 & 0 & 0 \\ 0 & 0 & 0 & C_{44} & 0 & 0 \\ 0 & 0 & 0 & 0 & C_{44} & 0 \\ 0 & 0 & 0 & 0 & 0 & \frac{1}{2}(C_{11}-C_{12}) \end{pmatrix}. \qquad 2\text{-}8$$

$$S_{ij} = \begin{pmatrix} S_{11} & S_{12} & S_{13} & 0 & 0 & 0 \\ S_{12} & S_{11} & S_{13} & 0 & 0 & 0 \\ S_{13} & S_{13} & S_{33} & 0 & 0 & 0 \\ 0 & 0 & 0 & S_{44} & 0 & 0 \\ 0 & 0 & 0 & 0 & S_{44} & 0 \\ 0 & 0 & 0 & 0 & 0 & 2(S_{11}-S_{12}) \end{pmatrix}. \qquad 2\text{-}9$$

In the measurement and analysis of the piezoelectric properties and describe the material elastic properties, the translation between C and S is crucial, and will be used in the characterization of the mechanical properties of AlScN. Therefore the relationship between the stiffness and compliance is shown below [16]:

$$S_{11} = \frac{C_{11}C_{33} - C_{13}^2}{(C_{11}-C_{12})[C_{33}(C_{11}+C_{12}) - 2C_{13}^2]} \qquad 2\text{-}10$$

$$S_{12} = -\frac{C_{12}C_{33} - C_{13}^2}{(C_{11}-C_{12})[C_{33}(C_{11}+C_{12}) - 2C_{13}^2]} \qquad 2\text{-}11$$

$$S_{13} = -\frac{C_{13}}{C_{33}(C_{11}+C_{12}) - 2C_{13}^2} \qquad 2\text{-}12$$

$$S_{33} = \frac{C_{11} + C_{12}}{C_{33}(C_{11} + C_{12}) - 2C_{13}^2} \quad 2\text{-}13$$

$$S_{44} = \frac{1}{C_{44}} \quad 2\text{-}14$$

Another coefficient which is related to the piezoelectric material and very important for the resonators based on piezoelectric material is the electromechanical coupling factor. It is defined as the ratio of the conversion between mechanical and electrical energy. The electromechanical coupling factor discussed in this work is divided into two categories according to the material or the fabricated devices. Considering the piezoelectric tensor components of the material, the material coupling factor is expressed as [17,18]:

$$k_t^2 = \frac{e_{33}^2}{\left(c_{33} + \frac{e_{33}^2}{\varepsilon_{33}}\right)\varepsilon_{33}} \quad 2\text{-}15$$

Where the ε_{33} is the dielectric constant along the c-axis, and the indices t of the k_t^2 means that it is along the thickness direction. Another coupling factor is regarding the measurements of the piezoelectric resonator at the frequency of resonance, which is called the effective coupling factor:

$$k_{eff}^2 = (f_p^2 - f_s^2)/f_p^2 \quad 2\text{-}16$$

The f_p and f_s are the frequencies at the admittance maximum and impedance maximum conditions, respectively. The effective coupling is dependent on both the material coupling factor as well as the resonator geometry.

2.2 Aluminum scandium nitride, a novel piezoelectric material

2.2.1 Aluminum nitride

Back to the early years in 1960, when the microelectromechanical system (MEMS) started to develop, piezoelectric material was not widely used and only limited to ZnO due to the deposition technology. During the time the transducers were based on Lead zirconate titanate (PZT), and it was even more difficult to process and integrate on the silicon. Furthermore, the PZT suffered from low quality factor for radio-frequency applications and caused contaminations in CMOS production. As the ALN was introduced to the commercial use of the resonator, it drew a huge interest in the AlN MEMS application, due to the ideal reproducibility of the deposition, great compatibility in the silicon technology and enhanced performance in the AlN MEMS devices [19].

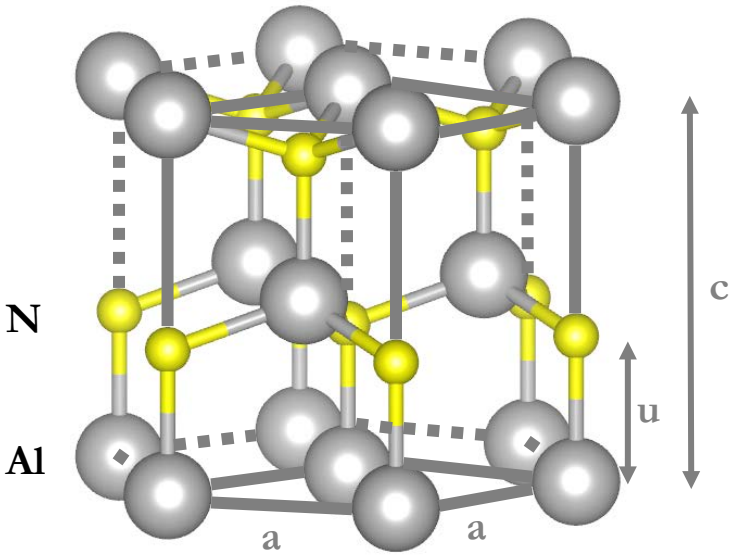

Figure 2-1 AlN with hexagonal wurtzite atomic structure, silver and yellow atoms stand for Al and N, drawn by usig VESTA

The atomic structure of AlN is shown in Figure 2-1, which indicates that piezoelectric wurtzite AlN is a close-packed hexagonal structure with space group P63mc (P: primitive, 63: screw axis with periodicity 6 and displacement 1/3 along *c*-axis, m: mirror plane p {100}, c: glide plane along c-axis, respectively). The lattice parameter *c* and *a* are 4.98 Å and 3.11 Å, respectively. $u = 0.38$ is the internal parameter, which defines the length of the bond length of anion-cation along the *c*-axis. One Al atom is attached to four N atoms in a tetrahedral like form. However, the Al-N bond B_2 along the *c*-axis (0001 direction) is slightly longer than the other three bonds B_1 (shown in Figure 2-2), which is 1.90 Å and 1.89 Å, respectively. Because of the asymmetry of the wurtzite structure, the AlN has a polar axis along the *c*-axis direction, which leads to an spontaneous polarization along the c-axis[20,21]. Furthermore, if the spontaneous polarization is already present in the crystal, the change in temperature will also change the polarization, this phenomenon is called pyroelectricity [22]. When the strain is applied along the *c*-axis direction, the displacement causes dipole moment change and leads to the polarization, which is called the piezoelectric effect. AlN is both exhibiting "positive" (aluminum) or "negative" (nitrogen) polarity, depends on the synthesize method and conditions, such as oxygen in the process gas [23,24], process pressure [11], especially seed layer or substrates [25]. Furthermore, there are some methods to increase the piezoelectricity by deposition the c-axis oriented AlN with tilting [26,27].

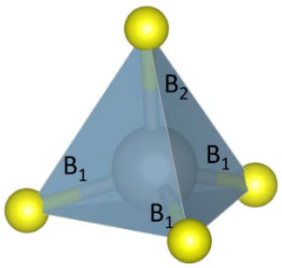

Figure 2-2 Tetrahedral geometry of the AlN, B_1 and B_2 stand for different Al-N bonds.

As a wide band gap III-V nitride semiconductors, AlN has 6.2 eV band gap while measured at the absorption edge [28], but the measured band gap is obtained at lower energy due to the defects gener-

ated during growth [29]. Furthermore, there were also some reports of the optical properties measured by Raman spectroscopy, the focus is normally on the E_2(High) and A_1(LO) modes [30–32], due to their relation to the stress and the crystalline quality. The thermal expansion coefficient of the AlN was determined by measurements and theoretical calculations, the value is between 4.35-5.27 × 10^{-6} K^{-1} and also temperature dependent [33–36]. The physical properties of AlN are summarized in Table 2-1.

Table 2-1 Physical properties of AlN

AlN properties	Values
Structure	Hexagonal wurtzite, space group P63mc
Lattice parameter *c*	4.98 Å [37]
Lattice parameter *a*	3.11 Å [37]
Band gap E_g	6.2 eV [38]
Linear thermal expansion coefficient α	5.27 ×10^{-6} K^{-1} [34]
Refractive index *n*	2.15 [39]
Piezoelectric coefficient d_{33}	5.5 pC/N [40]

2.2.2 Scandium nitride

Scandium nitride (ScN) is normally stable with rock-salt cubic structure with space group Fm3m (F: face-centered, m: mirror along {001}, 3: 3 fold symmetry along body diagonal, m: mirroring normal to face diagonal, respectively), as shown in Figure 2-3, the lattice constant a = 4.501 Å. The ScN is showing narrow and indirect band gap, which is measured between 2.1 eV and 3.2 eV [41–43]. Compared to AlN, ScN is not widely used in the industry. ScN shows potential in the electronic applications, and ScN has a very small lattice mismatch (< 0.3%) with GaN and thus serves a very good buffer layer of GaN to reduce the defects [44,45]. The deposition methods of ScN are mainly sputtering and molecular beam epitaxy (MBE) [43,44]. The measured Young's modulus and Poisson ratio for (111) ScN are 270 GPa and 0.188 [46], respectively.

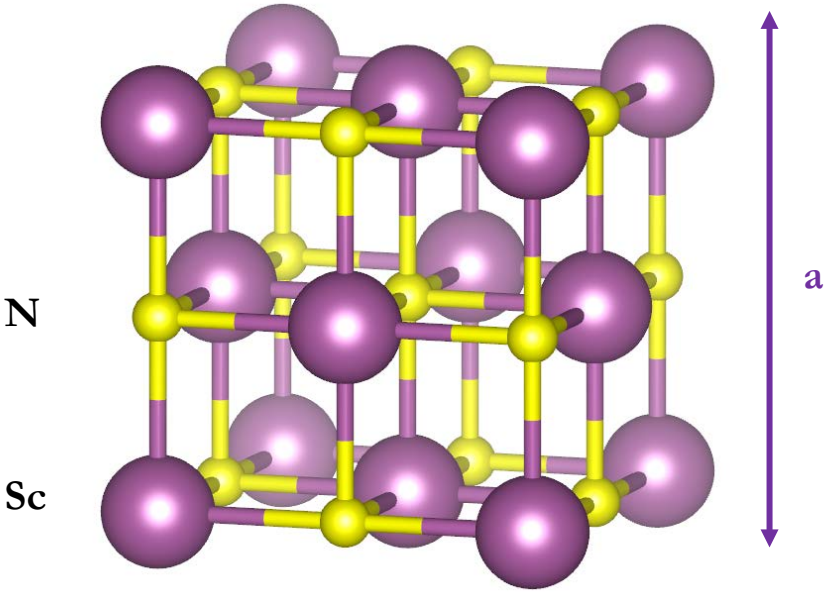

Figure 2-3 Cubic structure of ScN [47]

In addition, Farrer and Bellaiche also reported the existence of the layered hexagonal ScN [48,49], with space group 6/mmm and lattice parameter a = 3.66 Å, c = 4.417 Å. Due to the cubic structure, the rock-salt ScN normally doesn't show piezoelectric effect in the c-axis orientation, however, the strained hexagonal ScN is predicted to have piezoelectric coefficient e_{33} = 12 C/m² according to the first-principle calculations [49].

2.2.3 Aluminum scandium nitride

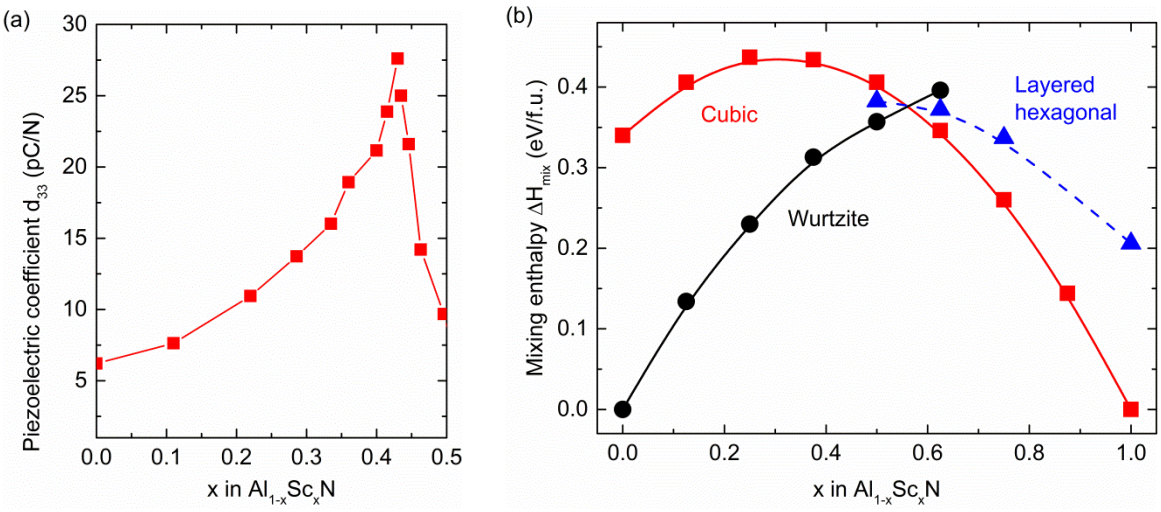

Figure 2-4 (a) Piezoelectric coefficient as a function of Sc concentration reported by Akiyama [3] **in 2009 (b) mixing enthalpy reported by Höglund et al. [50]**

In 2009, Akiyama *et al.* revealed the up to 400% piezoelectric coefficient d_{33} increase in the sputtered $Al_{0.57}Sc_{0.43}N$/Si (Figure 2-4 (a)). Although it was the first publication to introduce the AlScN, the achieved piezoelectric coefficient was the highest for several years. However, the first AlScN still suffered from distorted crystalline quality in the Sc concentration larger than x ≈ 0.43, the crystalline quality later was improved by decreasing sputtering temperature [51]. In order to figure out the structural stability of the AlScN regarding the Sc concentration, Höglund *et al.* [50] determinated the mixing enthalpy of different crystal structures using ab-initio calculation: wurtzite AlN, rock salt ScN and layered hexagonal ScN. Based on mixing enthalpy, the transition of AlScN from hexagonal wurtzite structure to cubic rock-salt structure at around x ≈ 0.56 (Figure 2-4 (b)). The electromechanical coupling coefficient of AlScN was reported by Wingqvist *et al.* [18], the electromechanical coupling coefficient k_t^2 in $Al_{0.7}Sc_{0.3}N$ has reached 15% compared to 7% in the AlN. These findings indicated the advantage of AlScN in the piezoelectric properties, and huge potential in the electro-acoustic applications in the future.

Some of the works on the theoretical calculations of the AlScN for lattice parameters, band gap, and mechanical properties are also worth mentioning. Zhang *et al.* [52] calculated the lattice parameters c and a using density functional theory (DFT), the transition point from hexagonal to rock-salt at x = 0.56 was determined, and the band gap ranges from 6.2 eV to 4 eV for AlN and $Al_{0.5}Sc_{0.5}N$, respectively (Figure 2-5). Caro *et al.* [53] calculated the piezoelectric coefficient and piezoelectric constant of AlScN, and later Zhang *et al.* [54] calculated the stiffness of the AlScN as a function of Sc concentration.

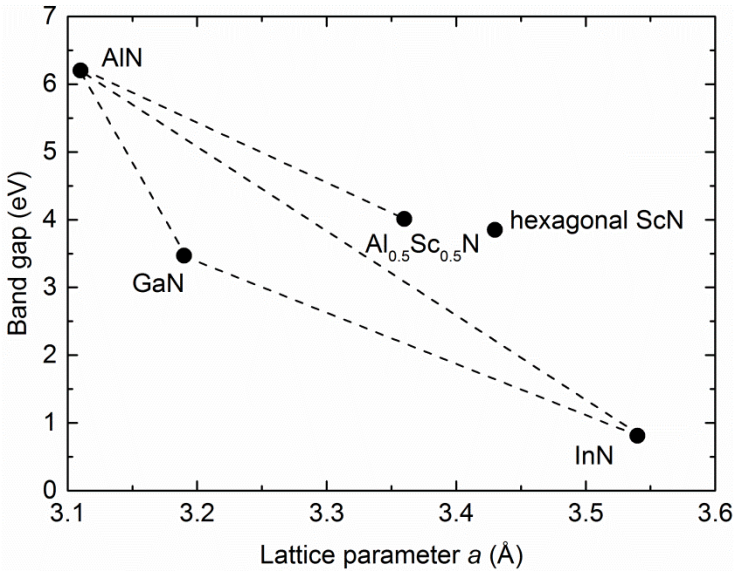

Figure 2-5 Band gap plot of AlScN as a function of Sc concentration, data from theoretical calculation [55], lines are the guide for the eye.

The deposition of the AlScN was mainly done by magnetron sputtering. Characterization of AlScN was mostly focused on the crystalline quality and piezoelectric properties. Zukauskaite *et al.* [56] determined the piezoelectric response of the co-sputtered AlScN/TiN/Al_2O_3 grown at 400°C and 800°C. Mayhofer *et al.* evaluated the piezoelectric coefficient d_{33} by Laser Doppler Vibrometry (LDV) of $Al_{0.73}Sc_{0.27}N$/Si sputtered by AlSc target with 30% Sc concentration [57,58]. Fichtner *et al.* [10] identified the abnormal microstructure during the sputtering deposition of the AlScN/Mo/Si structure. Barth *et al.* sputtered 10 um thick AlScN/Si by double ring magnetron sputtering system. Felmetsger *et al.* [59] sputtered AlScN film on 200 mm diameter Bragg mirror by S-gun magnetron facility, which showed the potential of the mass production for the device applications.

Nowadays, more and more electro-acoustic resonators of the AlScN are fabricated, including SAW and BAW devices: Gillinger *et al.* [60] showed unique phase velocity propagation direction of AlScN/Al_2O_3 based SAW resonators, Hashimoto *et al.* [61] fabricated the AlScN/single crystalline diamond based SAW resonators [62]. Pashchenko *et al.* fabricated hybrid BAW/SAW structure with unique polarity design based on AlScN [63]. Among the publications of the electro-acoustic resonators, part of the work is also collaborated with their industry partners, including EVATEC [64], Huawei [65], OEM group [66], Epcos [67] and so on, indicating not only scientific research but also huge potential in the industry and market.

At last, the deposition of the AlScN is not limited to the magnetron sputtering, Hardy *et al.* [68] demonstrated MBE grown AlScN with x = 0.14-0.24 on GaN and SiC substrates, opening a window for AlScN from electro-acoustic devices to high charge density electronic devices. Dittmar *et al.* [69] successfully grow the bulk ingot of AlScN by physical vapor transport sublimation, although the lower Sc concentration x = 0.0055, the bulk growth enables AlScN in the field of optoelectronics.

2.3 Sputter deposition

Sputtering is defined as the ejection of the species from a condensed matter target due to the bombardment of the particles, the first report of the of sputtering to deposit thin film was in 1852 [70].

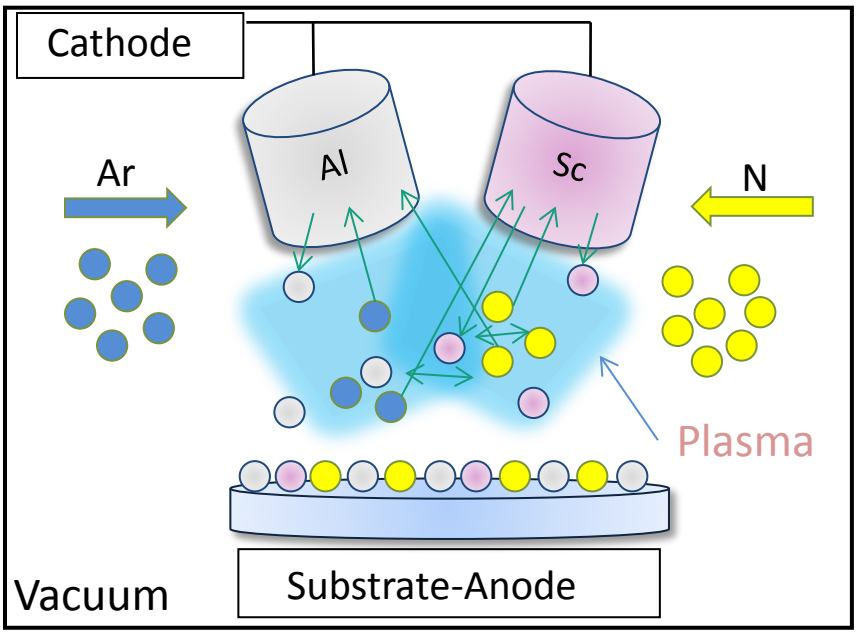

Figure 2-6 Schematic figure of reactive DC-magnetron co-sputtering.

In a sputtering process, the source of the coating material is called a target and mounted in the vacuum chamber. The target could be either pure element or ceramic. Furthermore, to control the mixture of the materials in the film deposition [71], sputtering system can be equipped with multiple different targets, which is called co-sputtering. The partial power on the target in the co-sputtering could be adjusted independently, thus the composition of the required material is tailored.

The schematic figure of the co-sputtering setup used in this work is shown as an example (Figure 2-6). Inside the chamber, the targets serve as cathodes and the substrate serves as anode, the substrate is mounted opposite the target in our case and chamber was evacuated by turbo molecular pump (TMP) to a range from 10^{-6} to 10^{-8} mbar. Later the reactive and inert gas is introduced to the chamber, which is N_2 and Ar for AlScN. A glow discharge plasma is used to ionize the gas atoms and the ions are accelerated toward the targets. Due to the bombardment of the targets, the species such as Al^- and Sc^- are leaving the targets. Under the electric field between the cathode and anode, the sputtering species, the gas molecules, and ions are accelerated towards the substrate. To control the electric field, the anode could be set as floating potential or with biased potential. It is also dependent on the chamber conditions including process pressure or density of the particles, whether the collisions of the particles are happening before landing. In discharge plasma the gas molecules are ionized and the electrical energy is transferred to the momentum of energetic gas particles. Through collisions, the chemical reactions are thus promoted and depositions are conducted. Also, the momentum energy of the impinging sputtering species is influenced by collisions. The collision probability in a gas-phase is often defined by mean free path λ, which stands for the distance traveled by the particles between collisions:

$$\lambda = 1/(N\sigma) \qquad 2\text{-}17$$

here the N is the gas-particle density and σ is the collision cross section, which could be written as:

$$\sigma_{tot} = \sigma_{el} + \sigma_{ex} + \sigma_{ion} + \sigma_a + \sigma_{oth} \quad 2\text{-}18$$

the indices el, ex, ion, a and oth stand for elastic or momentum exchange, excitation, ionization, attachment, and other processes, respectively.

However, initially the sputtering process is limited by low deposition rates, low ionization efficiencies and high substrate heating effects due to the secondary electron [72]. The magnetron sputtering technique was used to overcome these issues. A ring magnet is set around the outer edge of the target to form the magnetic fields and constrain secondary electrons, which increases significantly the probability of the ionization of atom and results in a dense plasma [73].

Magnetron could be powered by a variety of methods, such and radio frequency (RF), direct current (DC), pulsed-DC and high power impulse magnetron sputtering (HIPMS) [74]. Although DC sputtering is simple and cost efficient, arcs often occur during reactive sputter deposition and can be characterized as a low voltage and high current discharge. Furthermore, the insulating film forming on the target surface will drastically reduce the growth rate when using DC sputtering for the dielectric films (also called target poisoning). To prevent arcing and the target poisoning, the applied voltage is working in a DC-pulsed mode, which means a low reversed charge is applied to targets when the charge is accumulated on the targets.

2.4 Growth mechanism

A continuous polycrystalline film with specific crystallographic orientation consists of the grains with a distribution of certain grain size [75]. To understand the mechanism of nucleation and growth of the film, including microstructure and its evolution during the sputtering is necessary to control and tailor the properties as well as performances of the desired thin film. In the case of sputtering wurtzite structure AlN thin films, surface roughness [76–78], electrical properties [79,80], and mechanical properties [6] will be influenced by the microstructure.

When deposition is carried out, first atoms or species reach the surface of substrate and form clusters, which is called nucleation. Once they are formed, the nuclei will grow in both vertical direction and in the lateral direction parallel to the surface, which leads to crystal impingement and coalescence. The grain boundaries are created and some initial microstructure characteristics are already formed for this newly deposited film. The grain size of the nucleation is normally 10 nm or less, the further thickening of the film is necessary because of the application of the films. Two cases of the microstructure evolution are possible here: If the grain boundary is immobile during island impingement, the microstructure stays after it is influenced by the nucleation, growth, coalescence etc. However, when the epitaxial growth is conducted or columnar microstructure is observed, the in-plane grain size at the start of the deposition is often smaller than the grain size on the top surface, due to competitive growth [81].

2.4.1 Nucleation

The deposition of the thin film evolves mainly by one of the three growth modes: Volmer-Weber mode, Stranski-Krastanov mode and Frank-van der Merwe mode [73,82]. In the Volmer-Weber mode, small cluster nucleates directly on the surface of the substrate after landing, later they grow into islands and coalescence to each other to form a continuous film. Normally it occurs when the grown film atoms are bonding stronger between grains than the bonding to the substrate. Frank-van der Merwe mode is a 2D-layer by layer growth, when the binding between the film atoms is equivalent to or less than the binding of film atoms to the substrate. The Stranski-Krastanov mode refers to a combination of the 2D-layer by layer growth from Frank van der Merwe mode and 3D-island growth from Volmer-Weber mode. In a detail, the atom or clusters first form one or several monolayers, than the further growth turns into a 3D-island growth. It is not completely understood when the 2D growth is changed to 3D growth, when the lattice mismatch is existing between substrate and film. Here the Volmer-Weber growth is mainly discussed since we are conducting sputtering deposition at a lower temperature.[83]

During the deposition, the adatoms are arriving the surface with a flux *R*, which indicates the number of incoming atoms per unit time on the unit area of substrate. Nucleation occurs when the rate of the clusters or atoms continuously grow to form islands is faster than dissolving to cluster or atoms back. The rate of nucleation is described and analyzed by capillarity theory or atomistic nucleation process [82].

In the capillarity theory, it is assumed that the heterogeneous nucleation of thin films on the substrate surface, atom or clusters are impinging to the surface and aggregates into larger clusters or separating to smaller entities through dissociation processes. A cluster is assumed to have a mean radius r, the free energy change ΔG with respect to dissociation could be expressed as:

$$\Delta G = a_3 r^3 \Delta G_v + a_1 r^2 \gamma_{vf} + a_2 r^2 \gamma_{fs} - a_2 r^2 \gamma_{sv} \qquad 2\text{-}19$$

where the a_1r^2, a_2r^2 and a_3r^3 stand for the surface that between the cluster and vapor phase, contact area between cluster and substrate, and volume of the cluster, respectively. Interfacial tensions ν with indices *v*, *f* and *s* are representing vapor, film and substrate, respectively. Usually the nuclei is assumed as spherical solid phase, then the critical nucleus size as well as critical free-energy can be calculated (the maximum size of nucleus and corresponding free-energy). Furthermore, the capillarity theory also predicted the dependence of nucleation on substrate temperature and deposition rate quantitatively, such as: higher substrate temperature leads to larger critical nuclei size; lower temperature and higher deposition rate leads to polycrystalline deposition [82].

The atomistic nucleation process is first mentioned to treat small amount of the atoms in the earliest stage of the growth as macromolecules. It defines critical dissociation energy *E* and stable critical cluster containing *i* atoms. This theory is very important because the application in the epitaxial growth, that the relationship between crystallographic orientation and conditions of supersaturation and substrate temperature are linked. It suggests the existence of the critical temperature *T* where the nuclei size and orientation would have critical change, and the critical temperature forming epitaxy layer is dependent on the material of thin film.

Besides the capillarity theory and atomistic nucleation process, other nucleation models such as kinetic model, density functional theory (DFT) and diffuse interface theory (DIT) are also developed, however, due to the limitation of the paragraph, they will not be discussed in detail here.

2.4.2 Microstructures

As mentioned before, the microstructures are influencing the properties of the as-deposited thin films, therefore it is very important to tune the deposition parameter finely to achieve the required microstructures. One of the most well-known model is the structure-zone model developed by Thornton [84,85]. In the original structure-zone model the growth behavior was categorized mainly into four regimes. The microstructure evolution is constructed as a function of argon pressure and the ratio of substrate temperature versus melting temperature of the material. In Zone 1 the $T/T_m < 0.1$, low substrate temperature leads to low adatom surface mobility. The surface morphology is mainly affected by shadowing effect, which means the adatoms are just located on the landing place due to low surface mobility and the formed microstructure is mainly influenced by surface roughness and geometry of growth equipment. The deposited films thus have lower density despite the high density of the individual grains. When the argon pressure is increasing, the voids structure is suppressed by limited adatom surface mobility. At slightly higher T/T_m (0.1-0.3), fibrous grains with conventional grain boundaries are observed, caused by self-diffusion and grain coalescence. According to the literature [6], the thin film piezoelectric AlN belongs to Zone T growth. When the T/T_m is increased to 0.3-0.5, the even higher surface mobility allows grain boundary migration and recrystallization, thus the columnar grain microstructures during the entire growth are observed. The faceted surfaces and flat grain tops could be found, when the T/T_m is further increased to 0.75 or above.

A revision of the structure zone model was reported by Messier [86] to discuss the zone 1 and zone T. The zone T was found with no obvious boundary to zone 1 and the parameter argon pressure was replaced by substrate floating potential V_f. The microstructure is highly dependent on the mobility of the adatom on the surface, in Thornton's structure zone model the mobility is correlated to substrate temperature. However, the energetic bombardment is also an important process [87] and should be considered. Furthermore, the factor of chemically induced mobility, which controlled by adsorption-desorption characteristics, is also described in the revised model. At lower mobility the zone T is small. The range of temperature ratio of zone T increases when higher bombardment energy is introduced. In the revised structure zone model the evolutionary growth is also taken into account. Several subzones A to E are assigned by the physical size of the column and void sizes, from 1-3 nm to 300 nm, respectively. Larger column sizes are expected in a thicker film. The revised structure zone model thus helps to explain a more specific case in the structure zone model developed by Thornton [84].

More extended structure zone model of sputtered biaxially aligned thin film growth is discussed by Mahieu *et al.* [83]. In this model the development of the film microstructure towards out-of-plane orientation and off the substrate normal is discussed in detail. For out of plane orientation, the microstructures are classified into zone 1a, 1b, 1c, T and II according to the structure information and resulting crystallographic orientation. In zone 1a and 1b, the morphology is formed due to energetic bombardment at low temperature. In zone 1c the temperature is further increased and adatom could overcome the diffusion barrier to form crystalline islands. One should notice the interesting crystallization behavior in zone T and zone II. The high surface mobility would allow grain diffusion and grow by kinetic behavior in the zone T. First faceted nuclei with random crystallographic orientation form

on the substrate, the overgrowth on these nuclei is with the same thickness per unit time. While the further enlargement of the grains, impingement between the grains happens and grain boundaries are created. During the competition growth, the facets with fastest geometric growth direction will cover other grains and overgrow further. Therefore, in zone T straight columns with out-of-plane orientation will be observed (Figure 2-7). In the zone II the substrate temperature is even higher, which enables the recrystallization and reconstruction of the atoms. Therefore a straight column structure throughout the whole film could be expected, overgrowth in the zone T will not happen.

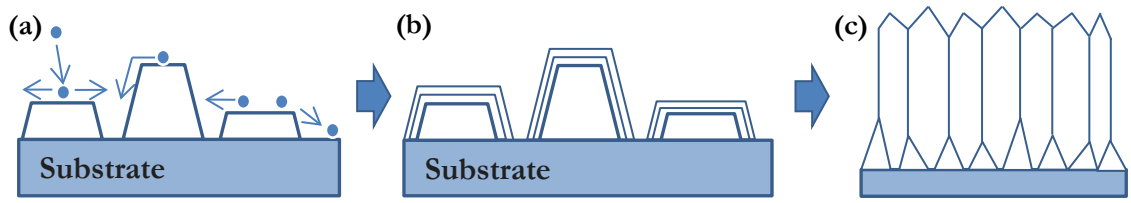

Figure 2-7 Schematic figure of the microstructure: (a) Adatom diffuses between grains and facets formed (b) Facet thickening in the out-of-plane orientation (c) Facets overgrow and straight columns created.

2.5 Sample preparation and sputtering procedure

Throughout the study of AlScN thin films, reactive DC-pulsed magnetron co-sputtering cluster system was used to conduct the deposition experiments. The sputtering cluster is shown in Figure 2-8, the load lock, plasma etching chamber and sputtering chamber with substrate heater are used to prepare the AlScN thin films on the substrate. The handling system could manage to transfer 200 mm wafers loaded in the cassette of 10 wafers.

Figure 2-8 Reactive DC-pulse magnetron sputtering cluster system at Fraunhofer IAF.

To complete a whole process of sputtering AlScN, the wafer is first loaded and transferred into soft-etching chamber. Induced coupled plasma (ICP) etching is applied to remove oxides on Si wafers and other residuals on the surface. Besides, it leads to the roughening of the surface and helps the

nucleation of the film. Afterwards, the cleaned wafer is transferred to the sputtering chamber and the temperature of substrate heater is raised to the desired temperature. In order to reach the thermal stabilization, the temperature is kept for 30 min. For the ignition of the plasma, Ar and N_2 gas are introduced to the chamber with large flow and the power is applied to the magnetrons. The linear shutter of the Al and Sc target in the step is kept closed, to ensure the successful ignition of the plasma and clean substrate surface before growth. In the next step, the linear shutter is opened and the gas flow is adjusted to the desired value for the sputtering.

To achieve the specific Sc concentration, the sputtering chamber is equipped with Al and Sc targets, the partial power of Al and Sc magnetron is adjusted independently. Both targets are 100 mm in diameter, the purity of Al and Sc targets are 99.9995% and 99.99%, respectively. The vacuum is reached by using TMP and controlled by the butterfly valve, the relationship of the pressure and valve opening is plotted below (Figure 2-9). The test was done with 2 sccm Ar and 18 sccm N_2 gas, recipes were used to sputtering $Al_{0.86}Sc_{0.14}N$. A strong drop of the pressure when the valve opening of between 20% to 40% is observed, and a plateau later exists in the region of 40% to 100%. This behavior of the processing pressure gives convenience to finely tune the sputtering process according to the different desired material properties.

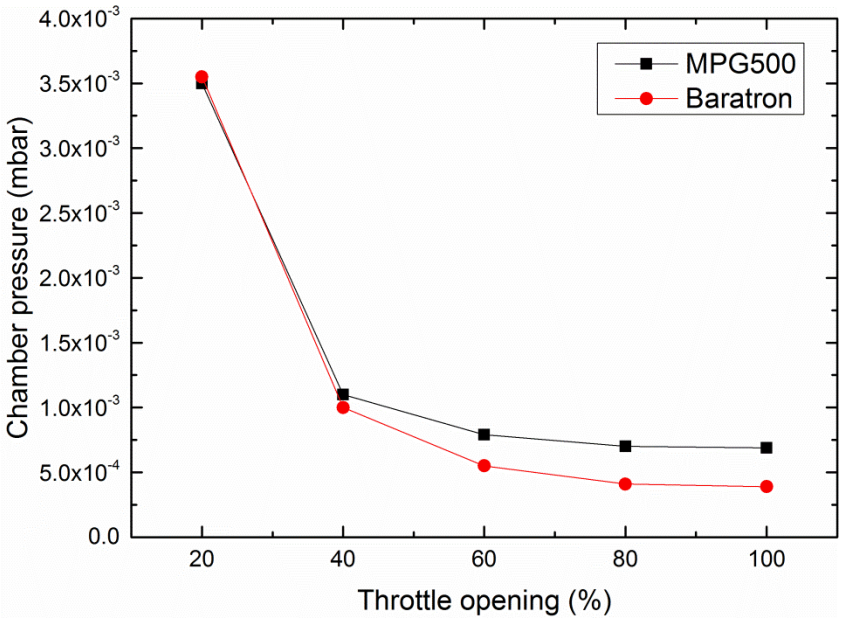

Figure 2-9 Pressure measured by vacuum gauge (MPG500) and baratron as a function of the throttle valve opening.

After the deposition of the AlScN thin film, the wafer is heated up to 300-500°C by the substrate heater as well as the bombardment of the sputtering species. To prevent cracks caused by the thermal shock, the wafer is cooled down in the sputter chamber for one hour and then unloaded.

The sputtering wafer is first measured by the ellipsometry to confirm the thickness of the AlScN thin films. The wafer curvature is measured by laser profiler before and after the sputtering to characterize the film stress. Afterwards, the characterizations are carried out to determine the crystallographic orientation and crystalline quality, microstructure, and other properties. The characterization methods such as X-ray diffraction, scanning electron microscopy (SEM), atomic force microscopy (AFM) are discussed in detail in the next chapter.

3 Characterization methods

In this chapter, part of the characterization methods to determine the properties of the $Al_{1-x}Sc_xN$ thin film will be discussed. The X-ray diffraction is used to confirm the crystallographic orientation of the $Al_{1-x}Sc_xN$. Furthermore, the crystalline quality is also checked. The surface morphology and the microstructure of the sputtered film are observed by scanning electron microscopy (SEM), Sc concentration of $Al_{1-x}Sc_xN$ is also determined by energy dispersive X-ray spectroscopy (EDX). Berlincourt method (also named Piezotest in some literature) offered a simple and fast determination of the clamped piezoelectric coefficient d_{33} of the $Al_{1-x}Sc_xN$, which is one of the most important parameters concerning the application of the electro-acoustic devices. Besides the characterization of the crystalline quality and electrical properties, optical measurement such as Raman spectroscopy and spectroscopic ellipsometry are also introduced here. The phonon vibration observed in Raman spectroscopy is an assist for us to analyze the internal stress of the localized areas. Spectroscopic ellipsometry are also introduced here. Spectroscopic ellipsometry is used to measure the reflection or transmission of the $Al_{1-x}Sc_xN$ film, the fitting of the ellipsometry spectra could help to describe the material parameter in terms of the dielectric function, and the band gap of the $Al_{1-x}Sc_xN$ could be determined.

3.1 X-ray diffraction (XRD)

The X-ray could be considered as electromagnetic radiation when it is impinging on the solid state materials, which is arranged periodically and the spacing is around the size of the wavelength of the X-ray. In this process, three types of interactions are undertaking concerning the energy range:

1. When the incoming radiation collides the atom with energy and momentum, electron of the atoms are released in the process of the photoionization, which belongs to inelastic scattering.
2. The incoming X-ray undergoes inelastic scattering process with the atoms and the wavelength is changed, which is termed Compton scattering.
3. X-ray is exciting elastic scattering, during this process the electron oscillates and produce dipole radiation with the same frequency of the incoming X-ray, this process is called Thompson scattering and it is used to determine the structural information in the X-ray diffraction [88].

When the X-ray reflection occurs, the relation of the incoming vector and scattered vector is expressed by the Bragg equation and the schematic figure is shown in Figure 3-1 (a):

$$n \cdot \lambda = 2 \cdot d_{hkl} \cdot sin\theta \qquad 3\text{-}1$$

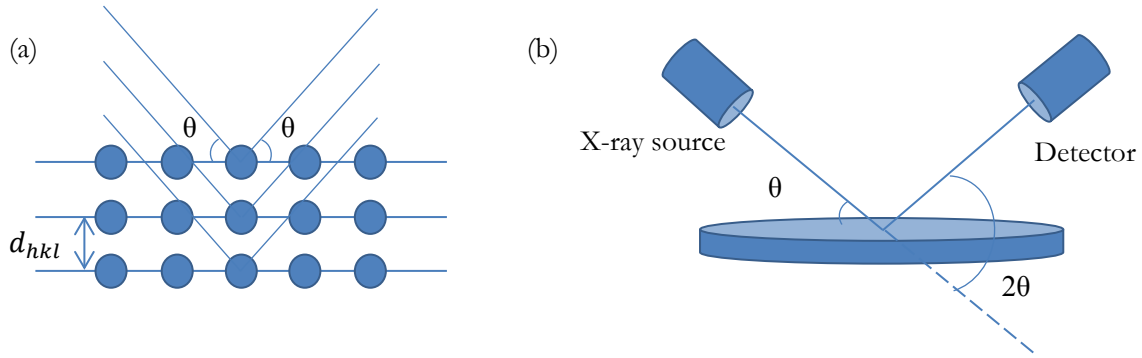

Figure 3-1 (a) Principle of the Bragg's equation, (b) Schematic figure of the Bragg-Brentano diffractometer.

where n is the order (n = 1, 2, 3…..) of the reflection in Bragg equation, λ is the wavelength of the X-ray, for the CuKα radiation which is used in this work the λ is 1.5406 Å, θ is the scattering angle between incident X-ray and detector and d is the interplanar spacing between crystallographic lattice plane with Miller indices h, k, l. The X-ray is impinging the crystallographic lattice plane with spacing d_{hkl} on an angle of θ. The spacing varies between different crystal systems, for hexagonal wurzite structure like AlN, its dependency on Miller indices h, k, l is shown in the following equation (3-2):

$$\frac{1}{{d_{hkl}}^2} = \frac{4}{3} \cdot \frac{h^2 + hk + k^2}{a^2} + \frac{l^2}{c^2} \qquad 3\text{-}2$$

The constructive inference of the reflective wave can only be achieved when the phase has a shift of the $2d_{hkl}\sin\theta$, therefore the n in the equation means the reflective order and is an integer.

Figure 3-1(b) is showing the widely used $2\theta/\theta$ Bragg-Brentano geometry. The sample was placed in the center of rotation axis and a flat surface is required. From the figure, both incoming and outgoing beam has an angle θ with respect to the sample surface. During the measurement, the diffraction pattern is collected by the detector. When the incident angle is changed by θ, the scattering angle is changed by 2θ simultaneously. Normally it is achieved by two symmetric sets of the instruments:

1. The X-ray source is fixed, the sample is turned by θ and the detector is turned by 2θ, which is the common setup used in this work,
2. The sample is fixed, both X-ray source and the detector are turning by θ, usually it is used in the powder diffraction.

In both setups the intensity $I_{(2\theta)}$ as a function of 2θ will be recorded. In the intensity $I_{(2\theta)}$ spectra, the intensity, shape and position of the reflections in order to determine the parameter such as lattice spacing, strain, grain size, and crystallographic orientation are important. The polycrystalline thin film with a certain dominating crystallographic lattice is called preferred orientation or texture. A film with texture or single crystalline will exhibit certain pattern in the intensity spectra. The crystallographic orientation is one of the most important parameter and it is revealed by indexing the reflections, to index the reflection pattern, identification of the phases is done by comparing measured data and records in the database, in this work we are using the database with the largest number of datasets, which is edited by the International Center for Diffraction Data (ICDD).

3.1.1 Rocking curve (ω-scan)

As mentioned that in a $2\theta/\theta$ scan, the position of the reflection is used to compare to the database and identify the phase information of grown material. The intensity and the shape of the reflection are analyzed to confirm the crystalline quality. For the diffraction pattern that contains only a few reflections, the rocking curve ω-scan could be performed. Similar to the geometry shown in Figure 3-1 (b), the sample is mounted to fit the configuration of the $2\theta/\theta$ with a certain θ orientation to study. However, in ω-scan geometry the incoming and outgoing X-ray beam are not coupled, but the outgoing angle is fixed. The incoming angle is called ω and fixed in a small range. Normally the symmetric $\theta/2\theta$ scan is first conducted for the fiber texture sample to exhibit preferred orientation. The thin film with fiber texture has normally the fiber axis coincident the substrate normal direction, but the crystallites are free to rotate around the fiber axis. Afterwards, the preferred orientation is shown as a reflection with angle θ in the intensity spectra, which is studied in the ω-scan and the full width at maximum (FWHM) of the reflection in the ω-scan intensity spectra is analyzed.

The FWHM of a rocking curve (0002) peak is considered as one of the most important factor, for piezoelectric AlScN thin films which reveals the layer thickness and crystalline imperfection like mosaicity. The mosaicity was first introduced by Darwin in 1923, it indicates the single crystalline materials with small variation of orientations. There are small grain boundaries between the grains and these dislocations allow the misorientation. In the fiber texture, the tilt of crystallites will cause the change of FWHM. When all of the crystallites are parallel to the substrate normal, the obtained FWHM is in a small value; otherwise a wider reflection with higher FWHM is obtained.

3.1.2 Grazing incidence X-ray diffraction (GIXRD)

The penetration depth of X-ray is normally hundreds of micrometer range, but the thickness of the thin film is regularly nanometer to micrometer range. Therefore, in the symmetric configuration like $2\theta/\theta$ scan, the structural information of the thin film is rather small compared to that of the substrate. To get sufficient X-ray intensity, an asymmetric configuration has been developed to use very small incident angle and thus the X-ray path in the thin film is increased drastically (Figure 3-2). This configuration is called grazing incidence X-ray diffraction (GIXRD). The measurement is undertaken when the incoming angle a is fixed in a rather small value. While the detector is moving along the 2θ circle, the outgoing angle regarding the sample surface is 2θ-a instead of θ in the symmetric configuration. The incoming, outgoing beam and the sample normal direction are in the same plane, therefore it is also called coplanar configuration, the same as $\theta/2\theta$ scan and ω-scan.

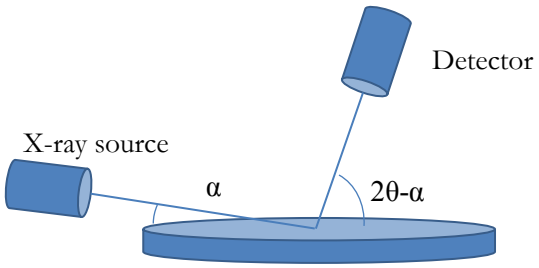

Figure 3-2 Schematic figure of GIXRD configuration.

3.1.3 Pole figure

Here we consider the $2\theta/\theta$ scan again, $I_{(2\theta)}$ spectra are contributed by Bragg reflection parallel to the sample surface. However, in the in-plane orientation they are not always isotropic. In the previous part the fiber texture is mentioned as all the crystallites aligning parallel to the substrate normal direction. The crystallites can also rotate around the fiber axis under fiber texture condition. If there is epitaxial relationship between grown layer and substrate, the rotation of the fiber is not possible. This in-plane orientation is not detectable neither by $2\theta/\theta$ scan or ω-scan. To conduct the scan from various orientation, azimuth angle φ and tilt angle ω are introduced. The azimuth angle φ is the angle of rotation around the sample normal, while the tilt angle stands for the angle between sample normal and scattering vector. In a pole figure measurement, first the $\theta/2\theta$ scan are measured in a specific azimuth angle φ and tilt angle ω, latter a step such as 5° are applied on the φ or ω, repeat the measurement. The schematic figure of the measurement is shown here (see Figure 3-3) with 4 variables ω, 2θ, φ and ψ. To visualize the function Ih(φ, ω), normally a stereographic projection named pole figure is used(Figure 3-4).

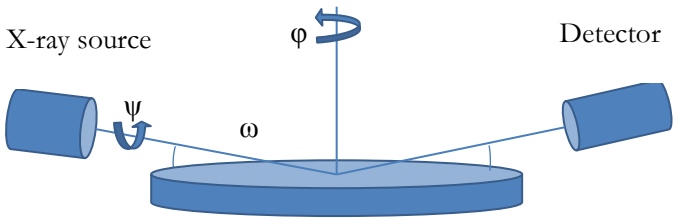

Figure 3-3 Schematic figure of the pole figure.

In the stereographic projection, the measurements can be plotted with (φ, ψ), where the azimuth φ is from 0° to 360° and it increases in the anti-clockwise direction, ψ is marked from 0° in the center and 90° in the outer circle. The pole figure measurement has to select first a reflection, e.g. AlN $10\bar{1}1$ is used in this work. Due to the fiber texture nature, the crystallites are rotating along the fiber axis but aligned to the normal substrate direction, the reflection of random in-plane alignment forms a circle marked as red in Figure 3-4 (a). If the epitaxial relationship to the substrate is established, like AlN/Al_2O_3, the pattern of the 6 fold symmetry of the crystal (marked as red dots in Figure 3-4 (b)) is shown in the projection, indicating the in-plane alignment of the single crystalline AlN [94].

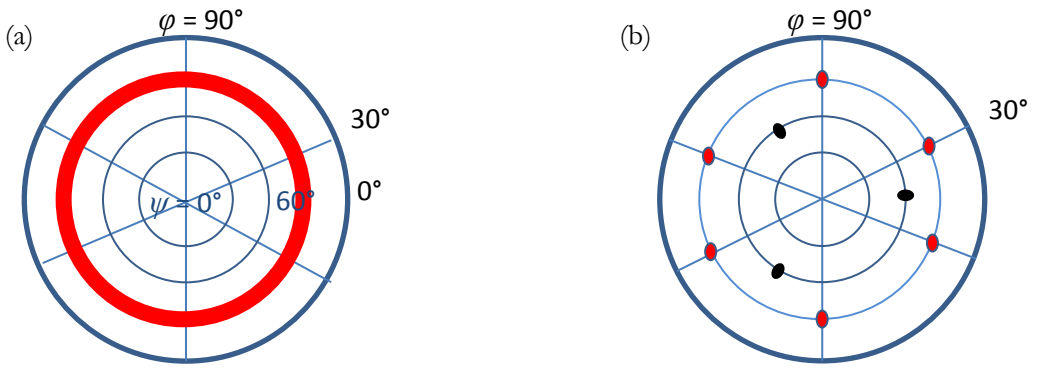

Figure 3-4 AlN $10\bar{1}1$ pole figure pattern for the AlN thin film with (a) fiber texture, (b) epitaxial relationship to the Al_2O_3, red and black spot are representing reflection from AlScN and Al_2O_3, respectively. In the case of (b), $[10\bar{1}0]_{AlScN}//[11\bar{2}0]_{sapphire}$ and $(0001)_{AlScN}//(0001)_{sapphire}$ is shown [89].

3.2 Scanning electron microscopy (SEM)

The scanning electron microscopy is the most widely used electron beam characterization method, due to the variety of detection modes, the high spatial resolution of the images, flexible size of the sample, and also the lower requirement in the sample preparation. SEM is used massively to analyze material microstructure and surface morphology. It is the swiftest method to determine the crystallization behavior and realize the material quality, thus it becomes the standard measurement after the as-deposited material is synthesized.

3.2.1 Electron-beam interaction

The beam of electrons is generated from the emitter and accelerated by the electrical objects. When the electron beam hits the specimen, the interaction is categorized into elastic scattering and inelastic scattering. The inelastic scattering leads to the transfer of energy and numerous processes, such as secondary electron excitation, inner shell ionization, Bremmstrahlung and excitation of phonons [90]. Those processes can be simulated and visualized by Monte Carlo simulation as shown in Figure 3-5, which is also called electron-beam interaction volume.

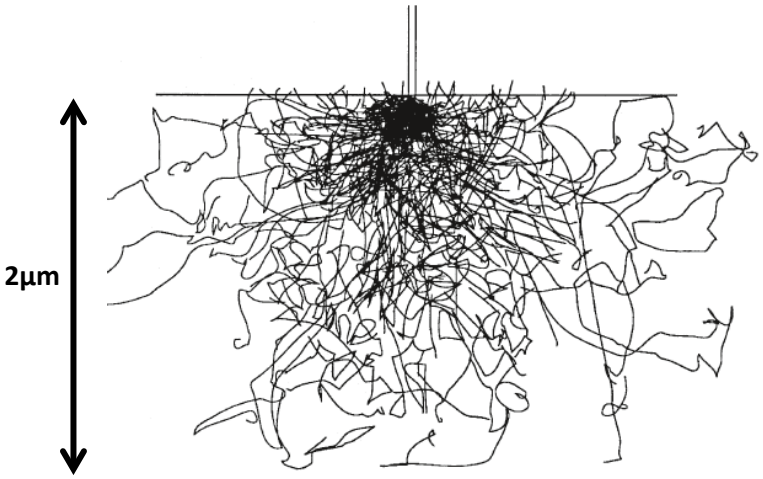

Figure 3-5 Visualized electron beam interaction volume, modified according to [90]

There are lots of aspects which could influence the interaction volume. First, the size of the volume is strongly dependent on the energy of the electron beam. As the beam energy increases, the electron trajectories near the surface become straighter and penetrate deeper due to the elastic scattering; also the energy loss rate is smaller and the electron beam enters with higher energy. Second, the higher atomic number leads to more elastic scattering and larger scattering angle. Third, the inclination of the sample surface also brings asymmetric and smaller interaction volume.

3.2.2 Energy dispersive X-ray spectroscopy (EDX)

As in 1968 the solid state energy-dispersion spectrometer was first mentioned by Fitzgerald et al. [91], the concept to use characteristic X-ray to determine the chemical composition of the sample is generated. Later the resolution of the detector is much developed and EDX module integrated in SEM as

well as TEM (Transmission electron microscopy) is used to identify the chemical composition of the specimen, qualitatively and even quantitatively.

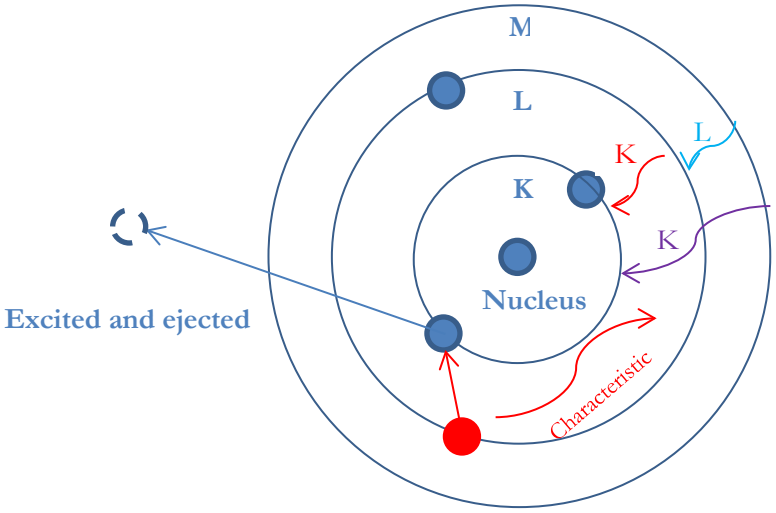

Figure 3-6 Schematic figure of characteristic X-ray emission

When the high-energy electron beam strikes an atom and reaches the critical excitation energy E_c, the electron in the inner shell (K) will be excited and ejected, which leaves a vacancy in the inner orbital. The electron from outer shell will fill in the vacancy to reach the minimum energy, which is shown in the Figure 3-6. When the transitions of electron from outer shell to the inner shell are happening, they generate characteristic X-ray radiation and for each atom every shell is unique. To specify the X-ray lines, e.g., Kα is corresponding to the electron transition from L shell to K shell, Kβ is corresponding to the electron transition from M shell directly to K shell, Lα is the transition from M to L shell, etc.[90]

These X-ray photons will be captured by the crystal inside the detector and create electron-hole pair. The electrical signal is formed by applying bias voltage and is sent to the amplifier and processed in the computer. To reach the low noise-to-signal ratio, the detector is kept at -25°C by thermocouple during the operation.

The identification of the X-ray line in the EDX is quite straightforward. First, the acceleration voltage of the electron beam (EHT), aperture, current, and accumulation time should be set to the value that the X-ray peak intensity is high enough to recognize. In this work it is measured normally under 15 kV, 120 um, high current mode, and 3 min, respectively. However, due to small grain size 20-30 nm for AlScN, under this configuration, it is very hard to recognize the grain boundaries of the grains, therefore the mapping of the surface is not possible. The Sc peaks are observed at 0.4, 4.1 and 4.5 keV, while the Sc Kα peak (4.1 keV) is chosen for qualitative and quantitative determination due to the overlapping of other Sc peaks with N. Possibly O peak will be observed at 0.5 keV and Ar peak will be at 3 keV position. The existence of the Si peak is indicating the interaction volume is into the Si substrate, as shown in the Monte Carlo simulation by the Bruker Quantax software the penetration depth is around 2 um at EHT = 15kV.

To determine the Sc concentration in the AlScN thin film quantitatively with EDX is a tricky but important task, due to the benefit from the short measurement duration and non-destructive feature of the EDX. EDX is more suitable compared to the complex sample preparation in SIMS (Secondary

Ion Mass Spectroscopy). However, if higher accuracy is needed, the RBS (Rutherfold Backscatter Spectroscopy) should be performed.

The first approximation of the relationship between peak intensity I_i and the concentration C_i (wt%) of the element i are discussed by Castaing in his PhD thesis in 1951:

$$\frac{C_i}{C_i^{std}} = \frac{I_i}{I_i^{std}} = k_i \qquad 3\text{-}3$$

where the k stands for relative intensity ratio. To apply the equation for quantitative calculation, first the concentration of reference or standard specimen needs to be confirmed. Then the X-ray intensity of the element i has to be measured by the same X-ray detector under same conditions, including incident energy of electron beam, aperture, current, take-off angle etc. Once the k is value is obtained, a correction coefficient according to the atomic number Z, absorption factor A and fluorescence effects has to be considered, which has been often referred to the well-known ZAF method [92].

$$[Z \cdot A \cdot F]\frac{C_i}{C_i^{std}} = \frac{I_i}{I_i^{std}} = k_i \qquad 3\text{-}4$$

The actual calibration of the AlScN sample regarding the quantitative Sc concentration determination is done by the reference sample measured already by SIMS. Therefore the peak intensity I_{Sc} are showing the amount of Sc, to exclude the influence of measurement on the absolute intensity of the Al or Sc peak, a ratio of $I_{Sc}/(I_{Al} + I_{Sc})$ is used to determine the Sc concentration. This ratio EDX spectra are compared to the Sc concentration in the SIMS, thus the equation of the Sc concentration regarding the Sc peak intensity is established, this work will be discussed in detail in Chapter 5.2.1.

3.3 Atomic force microscopy (AFM)

In 1986 the atomic force microscopy was first invented by Binnig et al. [93] to have high sensitivity to measure the surface morphology for conductor and insulator. Beside the lateral information, the AFM is also capable of the height information of the surface to provide height distribution as well as roughness. Therefore not only the SEM is involved in this work for the surface morphology and microstructure, but also the AFM is frequently used to determine the more detail mapping with roughness and 3D size of the microstructure. Furthermore, the homogeneity of the piezoelectric phase can be measured by the piezoresponse force microscopy (PFM) module.

Typically the scanning modes are categorized by the contact behavior into 3 cases: Contact mode, Non-contact mode and A.C. mode (Tapping mode). In the contact mode, the tip is kept contacting the surface and the cantilever is bending during the measurement. The bend is caused mainly by the Van der Waals repulsive force. Images are obtained by analyzing the deflection of the cantilever. However, because of the contact of surface it may induce some damage of the soft material and fast consumption of the tip. In the non-contact mode the probe is oscillating with specific resonance frequency above the surface, the frequency deviation is detected due to the Van der Waals attractive force and the image is formed. However, it needs vacuum condition for better imaging, it is influenced by the contamination on the sample and the lateral resolution is low. The intermediate mode (or A.C. mode)

is to combine the feature of contact and non-contact mode. First, the tip is excited at the resonance frequency with large amplitude, the excitation is finished by the piezo inside the AFM. Besides, the tip is also touching the surface, which means the tip is affected by both Van der Waals repulsive and attractive force. Furthermore, the tip could penetrate into the contamination layer and touch the real sample surface [94]. The feedback is normally based on both amplitude signal and phase, while the amplitude is reduced by contact of the surface and phase shift also happens [94].

Surface roughness and morphology was measured at Fraunhofer IAF by JPK Nanowizard III AFM in tapping mode with PPP-NCHR tips. The schematic figure of atomic force microscopy is shown below:

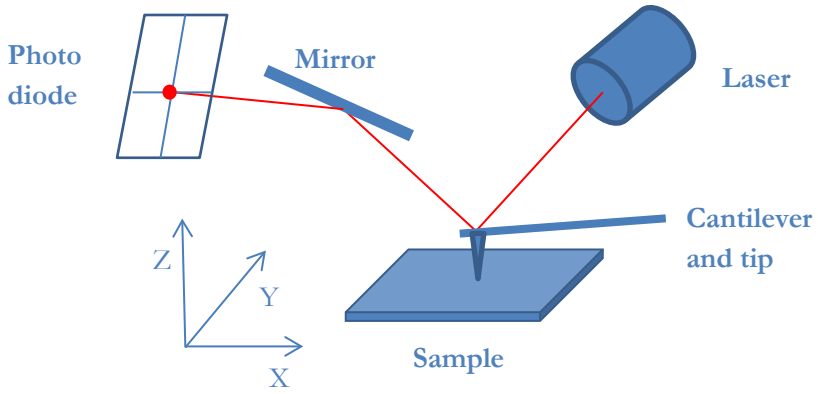

Figure 3-7 Schematic figure of atomic force microscopy

The tip is shaped like polygon based pyramid with a typical radius of 2 nm [95]. The cantilever with force constant could be considered as a spring plate, where the bend or the deflection is formed due to the Van der Waals force when it contacts the sample surface. The backside of the cantilever is coated with Al, therefore the laser beam is reflected and the deflection is captured by the photodiode.

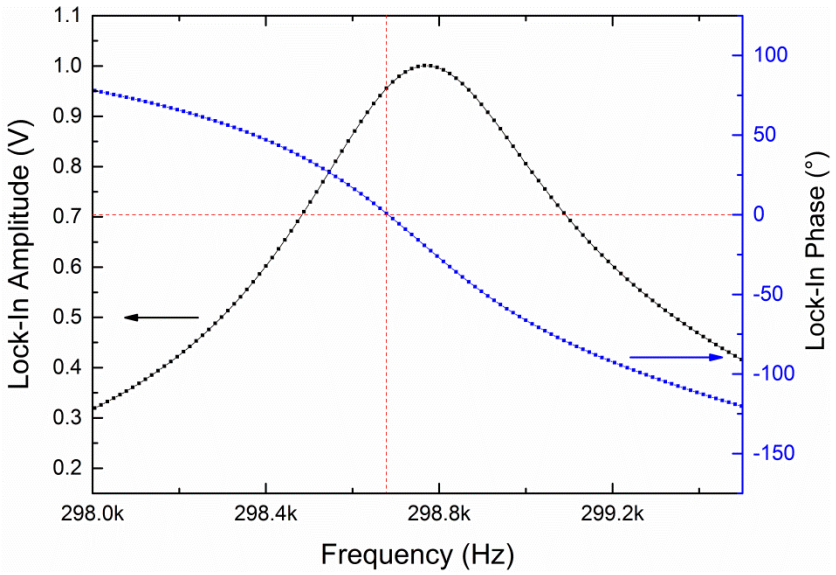

Figure 3-8 Lock-in amplitude and lock-in phase as a function of oscillating frequency, marked as black dots and blue dots, respectively. The red dash lines are indicating the set point as Lock-In Amplitude and tip resonance frequency.

Before the measurement, the resonance frequency as well as lock-in amplitude has to be selected, which is to keep amplitude at the maximum value. After mount of the sample and optical alignment of

the laser on the cantilever, A.C. mode has to be selected to perform the frequency tuning. The first step is to choose the resonance frequency, which is normally dependent on the tip, e.g., PPP-NCHR has 330 KHz as nominal frequency and the actual frequency ranges from 200 to 400 KHz (Figure 3-8), one significant peak with high amplitude will be recognized as resonance frequency. If multiple peaks are observed, the peak with strongest amplitude should be selected. To choose the frequency with highest intensity will allow high resolution of the topographic image. As shown in Figure 3-8, the actual frequency is located off the maximum and slightly shifted to the lower frequency, this is due to the shift to higher frequency during the measurement. When the frequency is chosen, the system will automatically adjust the phase to the zero, which means the applied phase is matching the actual operating frequency. Second is to choose the set-point (Figure 3-8), the set-point means the interaction force between tip and sample surface, because the feedback in the A.C. mode is based on decreased amplitude. Therefore, the lower the set-point, the higher interaction force applies on the sample surface. With a low set-point it is possible to consume the tip very fast and with high set-point the system could not approach the sample surface. For the used system the typical number is 0.6-0.7 V.

Furthermore, the roughness is also very important surface properties for applications, e.g., for surface acoustic wave devices to further deposit finger structure, smooth surface is required. In AFM the Root-mean-squared roughness R_{rms} is commonly used, the expression is shown below:

$$R_{rms} = \sqrt{\frac{1}{n}\sum_{i=1}^{n} \gamma_i^2} \qquad 3\text{-}5$$

To give a general idea of the roughness, for AlN thin film R_{rms} is around 1 nm and for good quality AlScN R_{rms} is smaller than 2 nm.

3.3.1 Piezoresponce force microscopy (PFM)

The piezoresponce force microscopy was first introduced by Guenthner *et al.* [96] as poling and imaging the localized piezoelectricity of the polymer film at the same time. Also the mechanism and applications are mentioned in some review papers [97–99]. In this work, the piezoelectric property is the most important and the main advantage of AlScN thin film. Therefore, the PFM is the method to bridge the surface topography and piezoelectric domain information. Through mapping the piezoelectric domain, e.g., piezo-amplitude, piezo-phase and height, overview of the sample surface and quantitative study can be made.

PFM is based on contact mode with conductive tip. Modulated A.C. voltage and D.C. bias is applied to the tip, while the piezoelectric amplitude and phase are recorded by two lock-in amplifiers simultaneously. The resonance frequency (or coupled resonance frequency) is chosen when the tip is approached to the sample, also named "resonance PFM". In this mode the resonance frequency is normally up to 1 MHz, much higher than the resonance frequency. Furthermore, the topographic image of AFM is recorded simultaneously [100,101].

Before PFM measurements, calibration is necessary to determine the range and zero reference of the piezo-phase, which is done by measuring PPLN (periodically poled lithium niobate) with 0° and 180° polarization.

3.4 Berlincourt method

As mentioned in the previous chapter, one of the most important advantages of AlScN is the increased piezoelectric response. The piezoelectric response is defined by piezoelectric charge coefficient d_{ij}, higher d_{ij} means more active piezoelectric response. To measure the piezoelectric response there are several methods available with varieties of accuracy and simplicity, such as, displacement measured by PFM [40], double-side beam interferometry (DBI) [67] and characterization of cantilevers [102]. The most widely use method is the Berlincourt method [51,103,104], with which it is convenient to excite the resonance and obtain the piezoelectric coefficient in the thickness direction.

The Berlincourt method is often conducted by Piezometer, the operating principle could be expressed as [105]:

$$\mathrm{d}_{33,f} = [\delta S_3/\delta E_3]_T \qquad 3\text{-}6$$

where the S and E stands for the strain and electric field strength, respectively. The indices 3 and T are indicating it is measured along z-direction under constant stress, respectively. The measurement setup consists of two parts: the force head and controller. In the force head the static preload and load with oscillating are applied on the sample. The controller is regulating frequency of the oscillation, measuring the charge and calculating the d_{33} value. Effects such as frequency, static preload, and sample replacement could lead to the deviation of measurement. Therefore AlScN/Si samples are cut into 1×1 cm^2 pieces and the preload is kept at 10 N for each measurement.

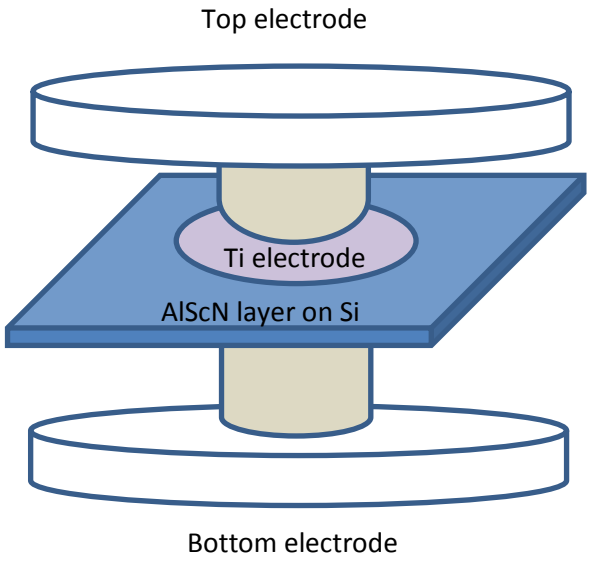

Figure 3-9 Schematic figure of the Piezotest setup

In the measurement of the Berlincourt method, first the AlScN/Si layer structure is achieved. Afterwards, the Ti electrodes with diameter around 3 mm are sputtered on the AlScN and the AlScN/Si wafers are diced into small pieces. The Piezotest is turned to the d_{33} mode, AlScN pieces are clamped between the top and bottom electrode. Because the Si wafer used in this work is highly conducting, there is no need of bottom metal electrode for the measurement. The preload is adjusted by turning

the screw spring of the top electrode, to keep the 10 N constant for each sample and ensure the repeatability of the measured d_{33}.

3.5 Raman spectroscopy

The Raman spectroscopy is a powerful characterization method to evaluate the parameter of the thin film, one of the most important uses is to determine the local stress of the AlN [106]. Besides, in the Raman spectroscopy the bonding information can be investigated by the phonon vibration modes. For wurtzite structure, the active optical phonon modes visible in AlN and AlScN in this work are listed in Figure 3-10. Among all of the optical phonon modes, A_1 and E_1 are along the polar axis, they are both IR and Raman active, they are divided into transverse optical (TO) and longitudinal (LO) phonon modes. In the E_2 symmetry the subscripts "low" and "high" indicates two different atomic displacement in the basal plane, therefore they are non-polar modes [107].

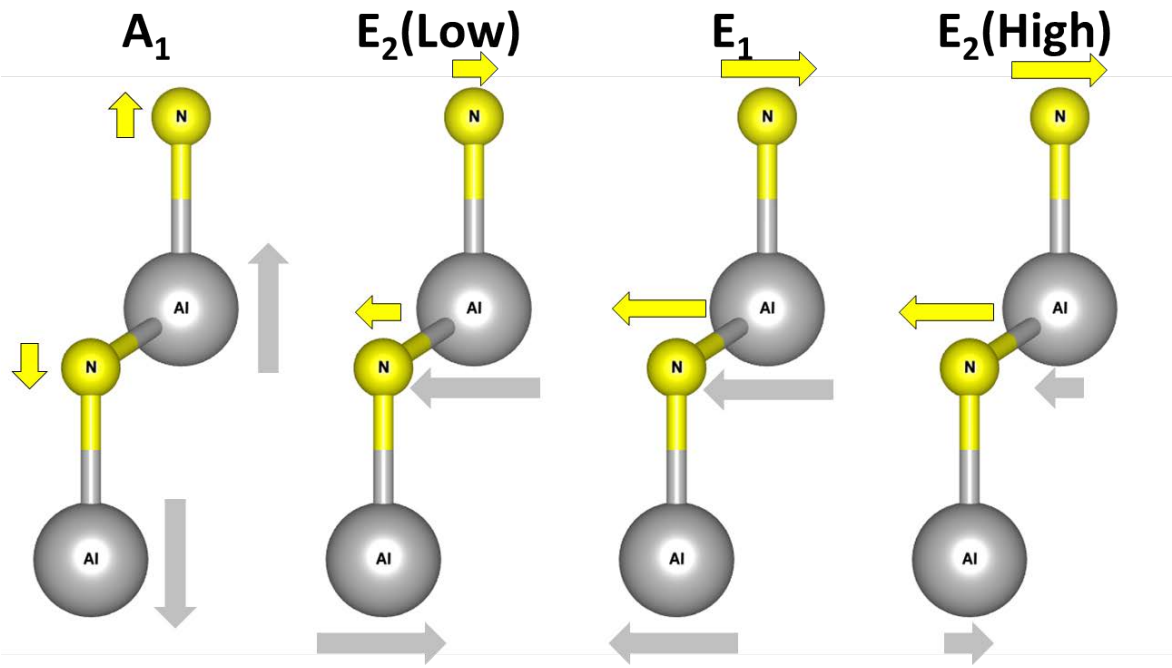

Figure 3-10 Optical phonon modes in wurtzite [32]

Furthermore, the configuration of the geometry in the Raman experiment (set by the filter) also influences the optical mode which is visible in the spectra, called Porto's notation. The Porto's notation consists of four letters a(b, c)d, where a means propagation of the incoming light direction, d means propagation of the scattered light direction; b and c stand for the polarization direction of incoming and scattered light. For the wurtzite crystal nitrides, the optical modes are visible under different configurations [108].

For example, the E_2 peak for wurtzite AlN is visible in the $z(x, y)\bar{z}$ configuration, which indicates the incoming laser beam and outgoing is propagating parallel to the c-axis orientation of wurtzite structure, polarization of the incoming and scattered beam are perpendicular to each other. Due to the weakening of the E_2 peak in the AlScN reported in the literature [109] and study of the higher Sc con-

centration, the Raman measurements are not confined in a specific configuration with filters. This work is discussed in Chapter 6.1.3.

Table 3-1 Raman configuration and correlated modes in wurtzite nitrides

Configuration	Mode
$x(y, y)\bar{x}$	$A_1(TO)$, E_2
$x(z, z)\bar{x}$	$A_1(TO)$
$x(z, y)\bar{x}$	$E_1(TO)$
$z(x, x)\bar{z}$	$A_1(LO)$, E_2
$z(x, y)\bar{z}$	E_2

The Raman spectra of AlScN samples were collected by Renishaw Invia Raman spectroscopy equipped with 532 nm Laser, with a 100× objective lens and 3000 l/mm grating. Before measurement the system was calibrated with Si reference sample.

3.6 Spectroscopic ellipsometry (SE)

Ellipsometry is an optical measurement technique to characterize the optical reflection or transmission from the sample. As shown in Figure 3-11, light with s-plane polarized and p-plane polarized is irradiating the sample with Brewster angle (normally 70-80°, will be explained later) , two values amplitude ratio ψ and phase difference Δ of the reflected s- and p- plane polarized light waves are analyzed. When the sample structure is not too complicated, the ψ and Δ are determined by reflective index n and extinction coefficient k, respectively. After reflection, the polarized light normally becomes elliptically polarized, therefore the characterization method is called ellipsometry [110].

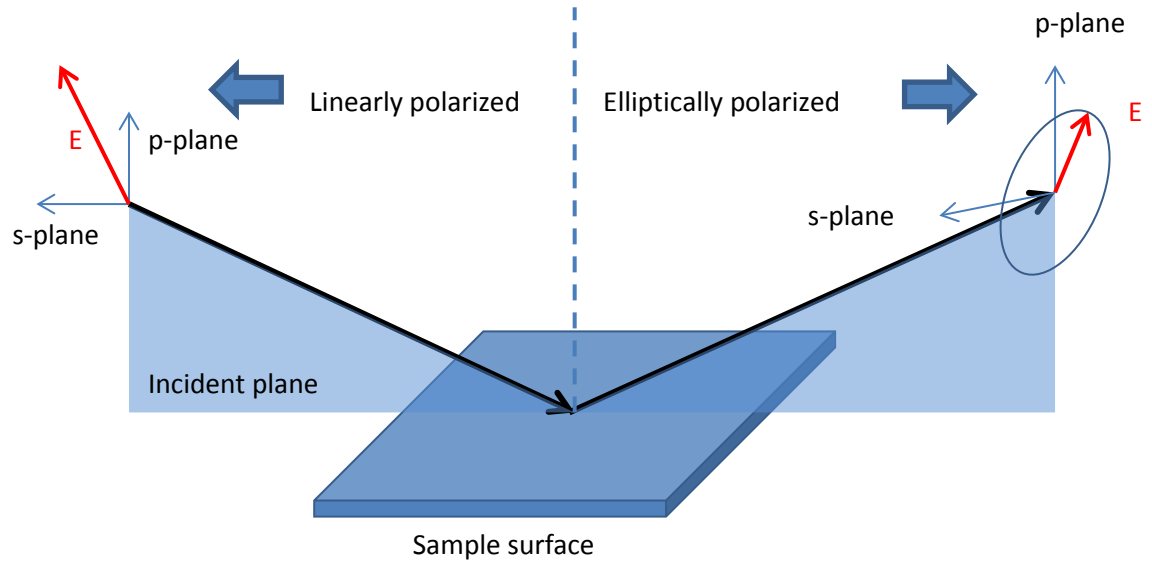

Figure 3-11 Schematic figure of light polarization with a sample.

3.6.1 Refractive index

When the light advances into an optically different media, the refractive index *n* is defined as:

$$n = c/s \tag{3-7}$$

where the *c* and *s* are the constant value of light speed in vacuum and light speed of light in a medium, respectively. When the medium is transparent, *n* could determine the propagation of the electromagnetic waves completely; while the medium is strongly light absorption, we introduce imaginary part extinction coefficient *k* and define the complex refractive index *N* as:

$$N = n - ik \tag{3-8}$$

When $k = 0$, it means the light travels without loss, while the $k > 0$ means the light is absorbed.

As the light propagation in a medium is described by the complex refractive index *N*, actually it is determined by dielectric polarization generated in that medium. The media with large dielectric polarization is called dielectric, there are mainly 4 kinds of dielectric polarization:

- External electric polarization
- Atomic polarization
- Orientation polarization
- Dipole moment

The magnitude of the polarization is defined as dielectric constant ε (also called permittivity). Since the light wave is electromagnetic wave, it has A.C. electric field and with sinusoidal shape. Thus the polarity of the surface charges varies with the time, the electric dipole does so as well. The time-varying external field accelerates the electric dipoles and radiates electromagnetic waves, which is known as electric dipole radiation, the frequency of the radiated electromagnetic field is equal to the external electric field. In the definition of the refractive index, the conclusion is that higher refractive index leads to lower light speed in a specific medium. If considering the electric dipole radiation, thus the decreased propagation speed is caused by the dipole in dielectrics which is with high ε value. Here the complex refractive index *N* is also defined by:

$$N^2 = \varepsilon \tag{3-9}$$

ε is complex number which defined by:

$$\varepsilon = \varepsilon_1 - i\varepsilon_2 \tag{3-10}$$

Similar to the complex refractive index, the ε_2 is also imaginary part.

3.6.2 Brewster angle

When the ellipsometry measures the ratio of amplitude reflection coefficients from s- and p- planes, the difference between is maximized at one certain incident angle. At the meantime, the sensitivity is also at maximum at the angle, which called Brewster angle and normally the ellipsometry is performed at the Brewster angle θ_B [111]. According to the Brewster's law, the expression of θ_B is:

$$tan\theta_B = n_t/n_i \qquad 3\text{-}11$$

Here the n is refractive index and the subscripts t, i represent transmission and incidence, respectively. If we consider the polarized light in p-plane, when the incident angle is $\theta_i < \theta_B$ and transmitted with θ_t, the atoms near the interface will have electric dipole radiation, reflected light is extracted only by the light wave with the same reflection and incident angle $\theta_i = \theta_r$. When $\theta_i \neq \theta_B$, there is a $\Delta\theta$ between direction of the reflected light and oscillatory direction of electric dipoles, and $\Delta\theta$ becomes zero if $\theta_i = \theta_B$. From s-plane, the oscillatory direction of the reflected light is always parallel to the vibration direction of the reflected light. Therefore when we combined the s- and p- plane polarized light, only when satisfying $\theta_i = \theta_B$, there is significant difference of the electric dipole radiation between s- and p-plane, for the semiconductors characterization the Brewster's angle is 70-80°, depends on the wavelength.[111,112]

3.6.3 Measurement and analysis of SE data

As we mentioned, the measurement of the spectroscopic ellipsometry is expressed as amplitude ratio ψ and phase difference Δ, the measured complex ratio ρ has the relation:

$$\tan(\psi) \cdot e^{i\Delta} = \rho = r_p/r_s \qquad 3\text{-}12$$

Here the r is complex Fresnel reflection coefficient and subscript p, s stands for p-, s-plane polarized light, respectively. In a variable angle spectroscopic ellipsometry (V.A.S.E), the measurement is done with variable wavelength as well as incident angle. If we consider the optical constants of the measured materials needed for further analysis, combined with the equations listed above, the relation to the ellipsometry measurement could be expressed as:

$$N = \varepsilon^2 = \sin(\theta_i)^2 \cdot \left[1 + \tan(\theta_i^2) \cdot \left(\frac{1-\rho}{1+\rho}\right)^2\right] \qquad 3\text{-}13$$

Because the ellipsometry doesn't measure the material properties like thickness or optical constants directly, therefore the analysis of the measured values must be performed, it consists mainly of three parts: 1) dielectric modeling, 2) construction of the optical model, 3) fitting of the measured values ψ and ⊿. If we have wurtzite AlScN thin films which need determination of the thickness, we could first assume the model with optical structure AlN(layer 1)/Si(substrate), the optical constants of AlN and Si are already known. Second, the expected ψ and ⊿ are predicted by the constructed model using Fresnel equations, also the wavelength and the incident angle have to be chosen. At last, the measured ψ and ⊿ is used to compare to the values predicted, which was based on Fresnel equations, to determine

the optical constant as well as the thickness of the materials. In the analysis part, the most difficult procedure is to decide which model is suitable and which parameter is used to do the fitting.

The Cauchy-Urbach dispersion model [113] is the widely used function to determine the refractive index *n*:

$$n(\lambda) = A + \frac{B}{\lambda^2} + \frac{C}{\lambda^4}\cdots \quad 3\text{-}14$$

$$k(\lambda) = \alpha exp\beta(12400(\frac{1}{\lambda} - \frac{1}{\gamma})) \quad 3\text{-}15$$

where the *A*, *B* and *C* are Cauchy parameters, λ is wavelength. In the part of extinction coefficient *k*, α, β and γ are the model numbers and has to be adjusted [114].

Tauc-Lorentz model is also attempted to describe the optical constants for the dielectrics, it is combined with Lorentz model and the Tauc band edge [115]:

$$\varepsilon_2(E) = \left[\frac{AE_0C(E-E_g)^2}{(E^2-E_0^2)+C^2E^2}\frac{1}{E}\right], E > E_g \quad 3\text{-}16$$

$$\varepsilon_2(E) = 0, E < E_g \quad 3\text{-}17$$

Where the *A* is the amplitude, E_0 is the peak transition energy, *C* is the broadening constant and E_g is the band gap. This Tauc-Lorentz model is only valid for interband transitions and the dielectric response from infrared transitions, Urbach tail effects and core transitions are not included. Obviously, the Tauc-Lorentz model is empirical expression.

To fit the dielectric model to get proper optical constant, difference between the measured and calculated ψ and ⊿ are determined by Mean Squared Error (MSE). The lowest MSE achieved implies a better model to fit the results, the MSE expression is shown below[110]:

$$MSE = \sqrt{\frac{1}{2N-M}\sum_{i=1}^{N}\left[\left(\frac{\psi_i^{Mod}-\psi_i^{Exp}}{\sigma_{\psi,i}^{Exp}}\right)+\left(\frac{\Delta_i^{Mod}-\Delta_i^{Exp}}{\sigma_{\psi,i}^{Exp}}\right)\right]} \quad 3\text{-}18$$

3.7 Summary

In this chapter, overview of the characterizations used in this work was provided for a better overview of the developments and characterizations in the following chapters. The parameter settings in the PFM and EDX offer valuable information for the reader to compare results in this work with literature. The mechanism of the characterizations such as GIXRD and pole figure is discussed for better understanding of the experimental part.

After discussion of the characterization methods, the experimental work to develop $Al_{1-x}Sc_xN$ thin films starts from next chapter. The AlN was first optimized concerning microstructure and crystalline quality, in which SEM and XRD were mainly used. Based on AlN reference samples, AlScN thin films with homogenous piezoelectric domains and high piezoelectric coefficient are developed, the films are mainly measured by PFM and Berlincourt method. Raman spectroscopy and spectroscopic ellipsometry were used for determination of optical parameters in Chapter 6.

4 AlN thin film deposition

As already mentioned in the Chapter 1, that the AlScN thin films have several advantages in the electro-acoustic applications, but the sputtering deposition of the AlScN is still very challenging. Due to the same wurtzite structure of AlN and $Al_{1-x}Sc_xN$ ($x < 0.5$) and the well-established sputtering process of AlN thin films in the literature, the process window of sputtering AlN synthesized in the same co-sputtering chamber helps to understand the sputtering mechanism and optimize the AlScN thin films. Therefore the AlN thin films for electro-acoustic application are studied in this chapter. The optimization of the AlN sputtering process in this chapter is focused on microstructure, crystalline quality, which ensures the homogenous smooth surface for the acoustic wave propagation and performance. As mentioned in the literature [116], these properties of the AlN thin film can be achieved by finely tuning the sputtering parameters such as process pressure, TSD, and N_2 gas concentration. The following chapter explains how the desired properties are achieved by adjusting these sputtering parameters. Furthermore, the established models are explaining the evolution of microstructure with process pressure or TSD change, which will consider the kinetic energy caused by different sputtering parameter as well as the co-sputtering configuration used in this work. The models will help the understanding of the behavior in the similar sputtering setup and the further AlScN thin film optimization based on this established recipe of AlN.

4.1 Influence of the process pressure

The process pressure is one of the most important parameters in the magnetron sputtering, it is reported that the pressure could influence the intrinsic stress [106], crystalline quality [117,118], crystallographic orientation [119–121], microstructure [122], polarity [11]. In this part, the microstructure evolution caused by process pressure is analyzed. A model concerning microstructure and the process pressure is created at the end of this part to explain this behavior.

Table 4-1 Overview of the deposition parameters of the pressure variation series

Parameter	Value
P_{Al}	1000 W
Processing pressure	9.5×10^{-4}–8×10^{-3} mbar
Target-to-substrate distance	61 mm
N_2 / (Ar + N_2)	80%
Heater temperature	500 °C

As shown in Table 4-1, 500-900 nm thick AlN thin films were prepared on Ø = 100 mm Si(001) substrates with conductivity of 1-5 Ohm·cm using reactive pulsed DC magnetron sputtering in Ar/N_2 gas mixture with same processing time. Before the deposition, the process chamber base pressure was $< 5 \times 10^{-8}$ mbar. The Si(001) substrates were cleaned using in-situ inductively coupled plasma (ICP)

etching in Ar atmosphere to improve the AlN nucleation behavior [123]. All depositions were made at heater temperature of 500 °C. In this series, the process pressure was varied via different throttle valve opening (correlation of throttle valve and vacuum level already explained in Chapter 2.5), and also the total gas flow was further decreased to achieve process pressure 9.5×10^{-4}–8×10^{-3} mbar. The individual gas flows were controlled by mass flow controllers to provide the constant N_2 gas concentration, expressed as N_2 / (Ar + N_2). The sputtering power (P_{Al}) was kept constant at 1000 W. Pre-sputtering of the targets was performed prior to film deposition with a closed shutter for 1 minute in Ar/N_2 mixture.

4.1.1 Growth rate

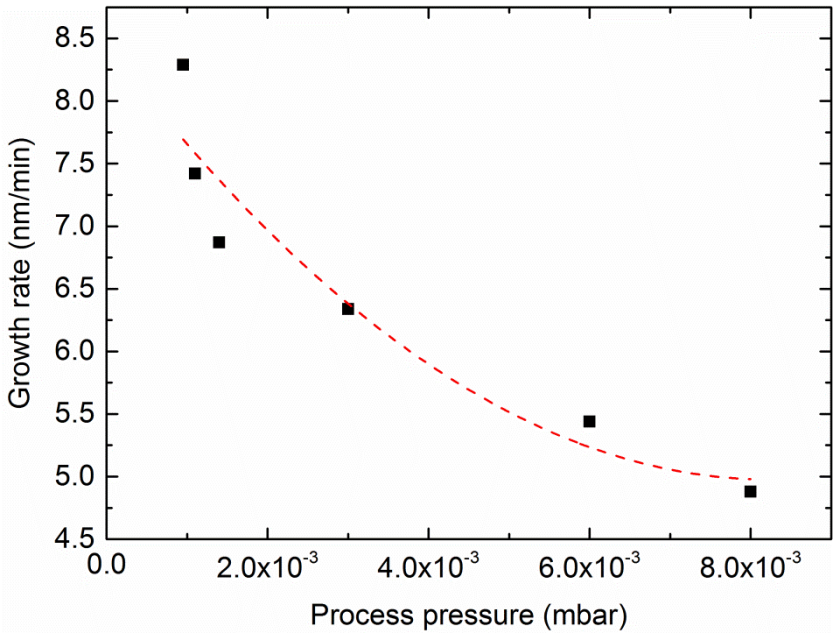

Figure 4-1 AlN film growth rate as a function of process pressure, the red line is a guide for the eye.

The dependence of the growth rate as a function of process pressure is shown in Figure 4-1, where the total film thickness ranged from 500-900 nm with same deposition time. In the region of 9.5×10^{-4}-1.4×10^{-3} mbar, the film growth rate is dropping drastically with increasing processing pressure, which is from 8.29 to 6.87 nm/min. After further increase the processing pressure larger than 1.4×10^{-3} mbar, the growth rate is still decreasing but the slope is much flatter. From the growth rate plot it can be observed that the growth rates are varying a lot around 1×10^{-3} mbar. There were also several literature reporting the similar trend as the processing pressure [117,124], the trend of growth rate decreasing strongly was reported in [125]. During the AlN sputtering a very high electric potential is applied to the Al-magnetron, the sputtered species are supposed to reach the substrate with high kinetic energy and less collision in the chamber, if there are less gas molecules to participate in the ionization and reaction. When the process pressure comes to 1.4×10^{-3} mbar, the mean free path is assumed to be comparable to the TSD, therefore the process pressure lower or higher than this value will cause huge difference concerning the kinetic energy and thus influences the growth rate. However, this behavior differs with respect to the DC or RF sputtering, e.g., in the RF sputtering the growth rate is not sensitive to the process pressure [106]; another case is the competition between growth rate from kinetic energy or numbers of molecules [120], when the number of molecules are dominating the growth rate, increasing of the process pressure leads to the increasing of the growth rate.

4.1.2 Microstructure

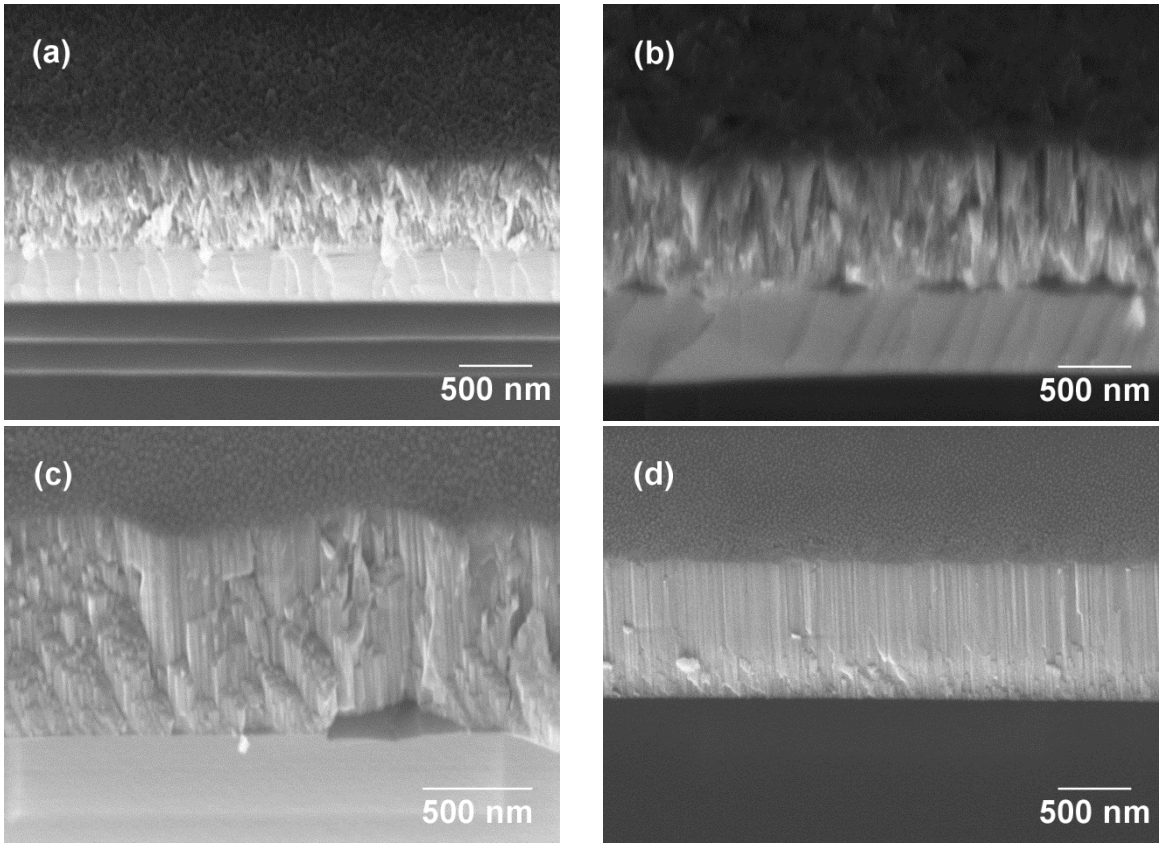

Figure 4-2 SEM cross-sectional images of the AlN thin film at the wafer center under different processing pressure (a) 8×10^{-3} mbar, (b) 1.4×10^{-3} mbar, (c) 1.1×10^{-3} mbar, (d) 9.5×10^{-4} mbar

The SEM figures of the AlN thin films sputtered under different process pressure are shown (Figure 4-2). The microstructure could be divided into three categories according to the process pressure:

1) The grains had V-shape growth when the pressure is larger than 1.4×10^{-3} mbar ((Figure 4-2 (a) and (b)). Not only the columnar growth at the cross section was missing, but also the surface is inhomogeneous. The V-shape microstructures are caused both by the rotation of the substrate and the co-sputtering configuration of the target. Therefore, a different microstructure concerning the position on the wafer is assumed.

2) The process pressure decreases to 1.4×10^{-3} mbar in Figure 4-2 (b), where the film is still in columnar microstructure. However, from the cross section picture lower density grains are observed. Also on surface the pebble like structure is similar to the previous sample but with slightly larger grains. The AFM roughness R_{rms} = 3.631 is also larger than the previous condition, indicating a rougher surface.

3) The processing pressure reached the lowest value at 9.5×10^{-4} mbar which is shown in Figure 4-2 (d), the film has columnar structure at the cross-section as well as the high density grains. The columns are well aligned and straight towards the normal direction of the substrate. On the sample surface the pebble-like structure is observed, which is very common for sputtered high quality AlN thin film [6,125–127]. AFM shows the surface had lowest roughness R_{rms} = 1 nm (not shown here);

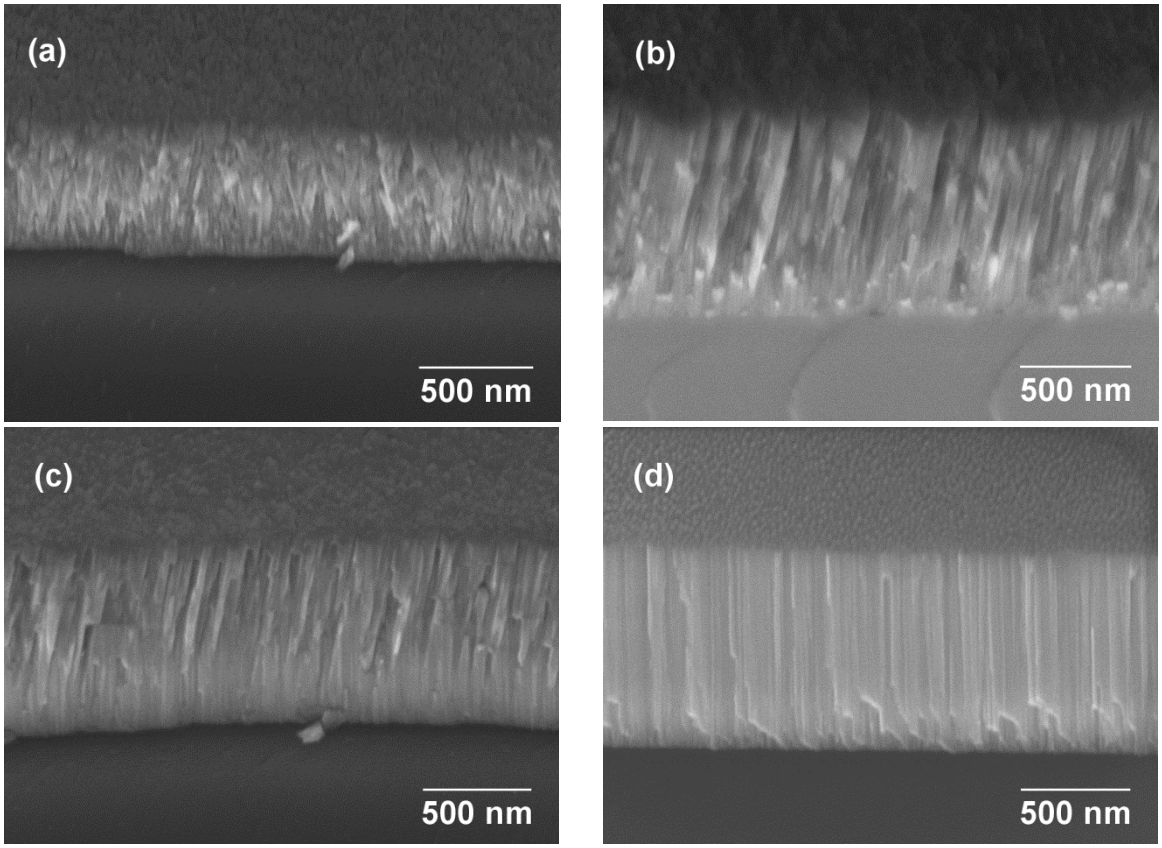

Figure 4-3 SEM cross-sectional images of the AlN thin film at the wafer edge under different processing pressure (a) 8 × 10^{-3} mbar, (b) 1.4 × 10^{-3} mbar, (c) 1.1 × 10^{-3} mbar, (d) 9.5 × 10^{-4} mbar

The SEM cross-sectional images were taken at the wafer edge for the same samples in the process pressure series (Figure 4-3). One can see the 1) and 3) categories are remaining the same as the wafer center. On the other hand, the evolution of the grains is different when the pressure is between 1) and 3), under the process pressure 1.4 × 10^{-3} mbar the grains at the edge of the wafer are tilted with a large angle, but when the pressure is decreased to 1.1 × 10^{-3} mbar, the grains first experience columnar growth along the c-axis orientation, and then show an inclination after around 100-300 nm.

In the lowest process pressure, the sputtering species incident the substrate surface with very few collisions to the each other. The kinetic energy of the species is high, that the adatoms have enough energy to find the preferred orientation and minimized surface energy in the basal plane, which is also the fastest growth direction. This behavior is quite similar to the zone *T* or even zone *II* in the Messier structure zone model [86] (explained in Chapter 2.4). Under such conditions the grains are arranged in a high density and growing along the substrate normal direction. If the pressure is increased, more ions are generated in the plasma, the possibility of the collision before the species reach the surface is increased, which causes a shorter mean free path. The collisions lead to a lower kinetic energy of the species. Part of the grains may have enough energy to form preferred orientation, therefore the straight grains are observed within the first grown 100 nm layers. As the thickness is increasing, the needed kinetic energy to support the growth along the preferred orientation is also increasing, which could not be afforded by the incoming species. Due to the 15° tilted target in the co-sputtering chamber, tilted grains at the position of the wafer edge are formed, which is why the grains are first straight then tilted. Similar behavior is found in the literature as "Biaxial texture sputtering deposition" [83,128]. As the pressure is further decreasing, because of the increasing probability of the collisions,

more and more grains formed due to the shadowing effect, which leads to lower density grains and V-shape/totally tilted microstructure according to the wafer position.

4.1.3 Crystallographic orientation and crystalline quality

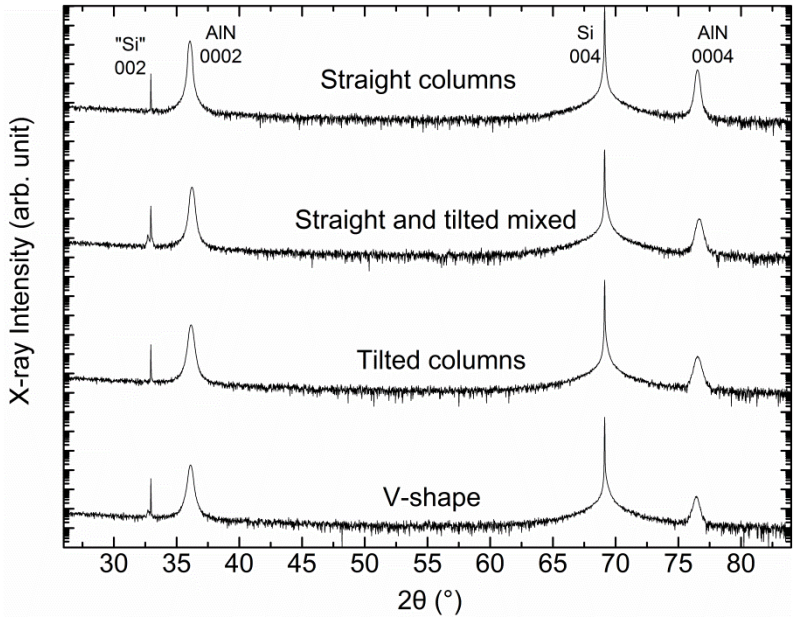

Figure 4-4 XRD 2θ/θ scans for the AlN sample with different microstructure (straight columns, straight and tilted mixed, tilted columns, V-shape) in the process pressure series,

In order to investigate the crystallographic orientation, XRD $2\theta/\theta$ measurements were conducted for samples sputtered under process pressure 9.5×10^{-4}–8×10^{-3} mbar (Figure 4-4). The listed $2\theta/\theta$ scans for the AlN thin films with straight columns, straight and tilted mixed, tilted columns, V-shape are indicating the samples with process pressure 9.5×10^{-4}(center), 1.1×10^{-3}(edge), 1.4×10^{-3}(edge), 8×10^{-3}(edge) mbar, respectively. All of the $2\theta/\theta$ scans showed only AlN $000l$ ($l = 2, 4, 6$) reflections in the measurement range. Since the $000l$ ($l = 2, 4$) are the only visible reflection for AlN and no addition AlN reflections are visible, indicating that lattice planes are arranged parallel to the sample surface and thus the sputtered AlN thin films all have pure c-axis orientation.

The crystalline quality was further investigated and quantified by the FWHM of AlN 0002 reflection rocking curves (Figure 4-5). Start with the sample deposited under the highest pressure $6\text{-}8 \times 10^{-3}$ mbar, the FHWM is as large as 4°. High FWHM values are indicating more and more tilted lattice planes compared to smaller value, especially the case at the wafer edge. Although the difference between the wafer center and wafer edge is eliminated, it only confirms that the shadowing effect is dominating in this pressure range in both positions. If the processing pressure is decreased to 1.1×10^{-3}–6×10^{-3} mbar, although the FHWM in the wafer center and edge are both decreasing, however, the steepness from the two positions is quite different. The difference reaches the maximum when the processing pressure is at 1.3×10^{-3} mbar showing 1.68° and 3.11° for center and edge, respectively. Finally when the process pressure is further decreased to 9.5×10^{-4} mbar, the FWHM of the wafer center and edge have the same value at 1.5°, indicating that the crystalline quality of the wafer center and edge are quite homogenous. This result concurs also the microstructure by cross-sectional image in the SEM, that from the wafer center and edge are dense, straight columnar grains.

The AlN thin films sputtered under different process pressure were in a huge thickness range, which is factor to influence the rocking curve FWHM. As reported by Martin *et al.* [129], the rocking curve of the sputtered AlN thin films with thickness 500 nm and 1000 nm are 1.26° and 1.14°, respectively. Therefore it is convincing that the increased FWHM 4° at 8×10^{-3} mbar is indicating a distorted crystalline quality instead of the effect by the smaller film thickness.

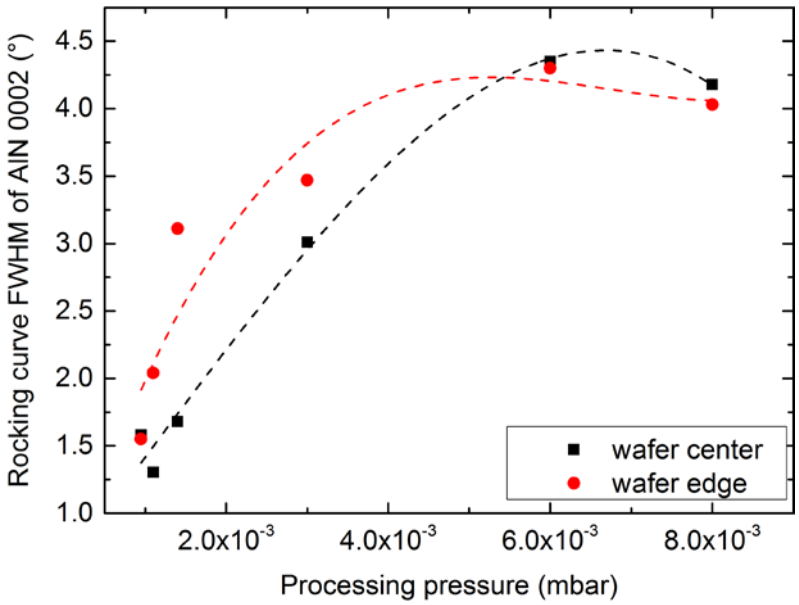

Figure 4-5 Rocking curve FWHM of AlN 0002 reflection as a function of processing pressure, the lines are the guides for the eye.

4.1.4 Discussion and summary

In this part it was shown that, for the AlN/Si the microstructure and crystalline quality distribution across the wafer can be controlled by process pressure, and the microstructure further influences growth rate. In the SEM cross-section, four kinds of the microstructures are observed, if arranged from the highest processing pressure, it should be 1) V-shape grains, 2) Tilted columnar grains, 3) First straight and then tilted columnar grains, and 4) Straight grains, now the evolution of these microstructures are discussed:

The schematic figure of the sputtering configuration as well as the different kinds of grain structures are shown in Figure 4-6.

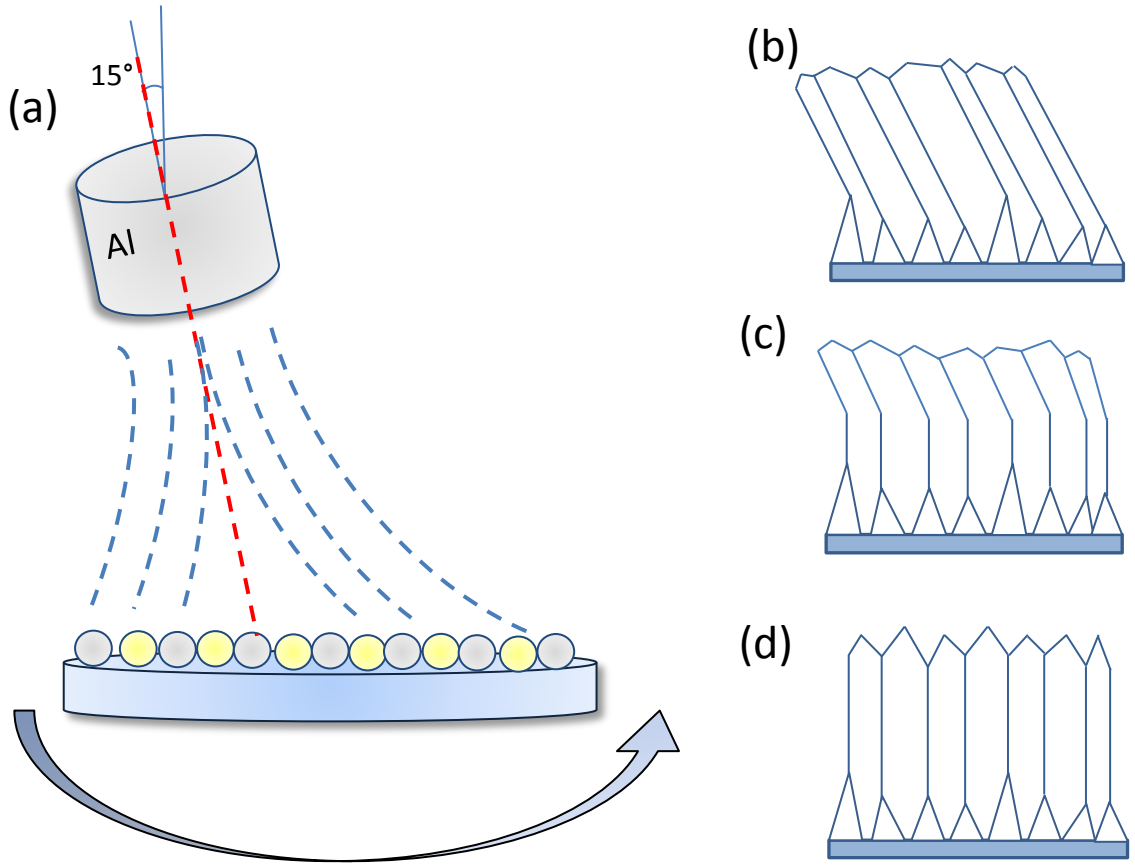

Figure 4-6 Schematic figure of the (a) target configuration and traces of the species in co-sputtering chamber (b) tilted grains (c) vertical grains combined with tilted grains (d) fully vertical grains

1) **The V-shape grains**: They appear at the wafer edge and the wafer center under highest processing pressure, due to the high probability of the particle collision only the shadowing effect are taking place. According to the target configuration in Figure 4-6 (a), in the wafer center the incoming particles are bombarding the substrate surface with 15° tilt angle, and low kinetic energy in not sufficient to support the species finding the preferred position. That is the reason why in the wafer center, the V-shape grains are observed when the pressure is increased to 8×10^{-3} mbar.

2) **Tilted grains**: As shown in Figure 4-6 (b), it is observed that tilt grains are formed directly on the nucleation layer. Considering the wafer edge in Figure 4-6 (a), due to the target configuration the incoming species are still with tilt angle. However, because of both smaller path of the particle and lower processing pressure, the kinetic energy is slightly higher and able to form the preferred growth orientation, but the shadowing effect still exists. Thus tilted columnar structure is formed, and it happens mainly at the wafer edge due to the co-sputtering geometry.

3) **Straight and tilted mixed**: As shown in Figure 4-6 (c), the processing pressure is even lower than the previous case. The higher kinetic energy is expected due to less collision before the deposition. In this case it is interesting to see co-existence of two kinds of grains, and probably it indicates a boundary of the energy. At the beginning of the growth, the columnar growth in substrate normal direction is obtained, because of lower processing pressure and the higher kinetic energy. The energy requirement to form larger grains with preferred orientation is increasing, at a certain point, the energy of the sputtering species, is not sufficient. There the shadowing effect takes place and the grain structure is back to the case of 2).

4) **Straight columns**: The grain is towards out-of-plane direction, as shown in the Figure 4-6 (d). The kinetic energy of the incoming species and adatoms is increasing, the preferred growth direction is achieved. The lowest processing pressure 9.5×10^{-4} mbar assures only c-axis oriented AlN thin film with the best crystalline quality, the measured $d_{33,\,clamp} = 7.5 \pm 0.2$ pC/N. The columnar microstructure and pebble like surface morphology is homogenous from the wafer center to the edge, which ensures the low roughness $R_{rms} = 1$ nm.

From the analysis there are two points: 1). The co-sputtering configuration in this work leads to a different kinetic energy of the sputtering species when they land on the wafer, which brings different microstructure across the wafer. However, if we imagine a single target setup, that the edge of the wafer is still possible to have the tilted grains. 2). Having the tilted grains is mainly due to the configuration of the sputtering setup, but to solve it, increasing the kinetic energy is the effective method.

The evolution of the crystalline quality, actually happens in the pressure region 9.5×10^{-4} mbar to 1.4×10^{-3} mbar, which is the region that the tilted grains and the V-shape microstructure co-exists. However, when the film is grown in a high quality, AlN thin film can be strongly tensile stressed up to 800 MPa, when the microstructure is evolving to V-shape or tilted grains, the stress will evolve to lower value. It is reported that the stress of the AlN is tuned by adjusting the processing pressure of the AlN/Si thin films in the RF sputtering [6], however, due to the sensitivity of the AlN to the process pressure discussed in chapter 4.1, it is not recommended in our case, and other growth parameter should be used for further improvement.

4.2 Influence of the target-to-substrate distance (TSD)

In the previous section the process pressure was discussed. Results show that low process pressure is preferred in terms of homogenous microstructure and better crystalline quality. From process pressure series, the co-sputtering configuration is influencing the microstructure due to unequal kinetic energy at different positions on the wafer. Therefore, finely tuning the TSD will also have effect to improve the microstructure. Furthermore, TSD was reported to have effects on the preferred orientation of sputtered AlN [119,130]. As a result, the influence of the TSD on the microstructure and crystalline quality of AlN was studied, as discussed below

Table 4-2 Overview of the deposition parameters of the samples in TSD variation series

Parameter	Value
P_{Al}	1000 W
Process pressure	9.5×10^{-4} mbar
Target-to-substrate distance	40-70 mm
N_2 / (Ar + N_2)	80%
Heater temperature	500 °C

The sputtering parameters of the AlN samples in TSD series are listed in Table 4-2. AlN thin films were prepared on 100 mm Si(001) substrates, the TSD was varied for different samples in the range of 40-70 mm. The process pressure was kept constant for each sample at 9.5×10^{-4} mbar based on results of process pressure optimization in chapter 4.1.

4.2.1 Growth rate and stress

As discussed in the pressure series, the large variation of growth rate as well as intrinsic stress as a function of sputtering parameter could indicate possible transition of the microstructure. The thickness of the AlN/Si thin films was measured by the ellipsometry and fitted with Cauchy-function with Urbach tail. The wafer curvatures of the wafer are then measured before and after the AlN growth, the stress is calculated according to the Stoney-formula.

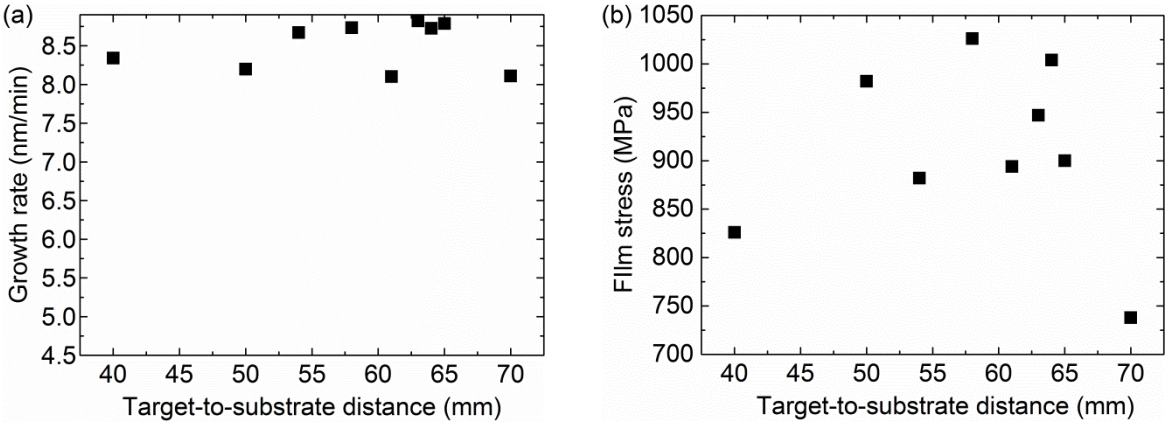

Figure 4-7 (a) Growth rate and (b) intrinsic stress of sputtered thin film AlN as a function of the target-to-substrate distance

In Figure 4-7, the film thickness and intrinsic stress are shown for TSD series. In Figure 4-7 (a), the growth rate is varying between 8-9 nm/min, compared to 5-8 nm/min in pressure series, it indicates the growth rate is less sensitive to the TSD than to the process pressure. From Figure 4-7 (b), the intrinsic stress is also in a range between 750-1000 MPa. The stress difference when the TSD in the range of 55-65 mm is in a range of 150 MPa, both the samples with TSD 40 mm and 70 mm show generally lower stress than other samples. When the samples are sputtered with TSD 50-65 mm, the trend of the growth rate and the stress are quite similar: The samples with higher growth rate normally are more tensile stressed. However the stress differences between the samples are less than 200 MPa, indicating no clear trend.

4.2.2 Crystallographic orientation and crystalline quality

In Chapter 4.1 the XRD $2\theta/\theta$ scans were used to determine the preferred orientation of the AlN thin films. However, all the thin films showed only AlN 0002 reflection and are indicating pure c-axis orientation. All of the $2\theta/\theta$ scans of the samples in the TSD series showed AlN 0002 reflection and were not influenced by TSD values. Therefore the $2\theta/\theta$ scans is not plotted here. The rocking curve FWHM of AlN 0002 is indicating the crystalline quality and also correlated to the possible distorted microstructure, therefore it is plotted in Figure 4-8 (a). The FWHM of the wafer center for TSD = 40 mm is 1.35° and is slightly increased to 1.6° for TSD = 65 mm, and then suddenly increased to 2° for TSD = 70 mm. On the wafer edge, the FWHM shows a similar trend as in the wafer center. Interestingly, it can be observed that the FWHM of these two wafer positions evolves with different increasing trends and overlaps when TSD = 65 mm, which is marked by dashed lines in the Figure 4-8 (a). For better observation, Figure 4-8 (b) is plotted to show the (ω-FWHM$_{center}$ - ω-FWHM$_{edge}$). When the TSD is in the range of 55-70 mm, the (ω-FWHM$_{center}$ - ω-FWHM$_{edge}$) decreases with TSD and reached

to zero when TSD = 65 mm, indicating the similar crystalline quality at different positions on the wafer. From the comparison of the FWHM value, the samples with best homogeneity of the crystalline quality are TSD = 65 mm. The next step is to confirm if microstructure is also homogenous as described in the next section.

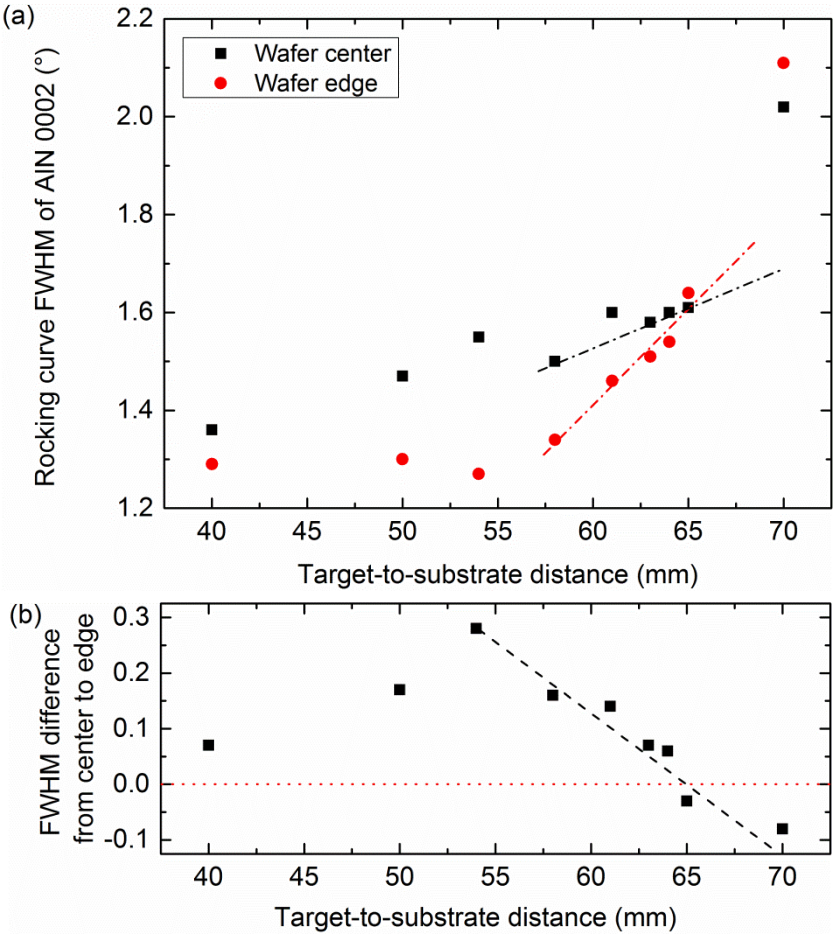

Figure 4-8 (a) Rocking curve FWHM of AlN 0002 reflection (b) difference of the FWHM in the wafer center and at the wafer edge as function of TSD, the lines are the guides for the eye

4.2.3 Microstructure

In the process pressure series, the difference of the ω-FWHM value of AlN 0002 peak normally indicating microstructure change at different position on wafer. Although the thickness in the process pressure is playing a role on FWHM values, the difference of FWHM values is up to 2° and huge difference of microstructure is observed. In the TSD series, the FWHM value evolves with a different trend as the TSD increases. The SEM cross-section images are shown in Figure 4-9 to confirm whether the microstructure is homogenous at a certain TSD value.

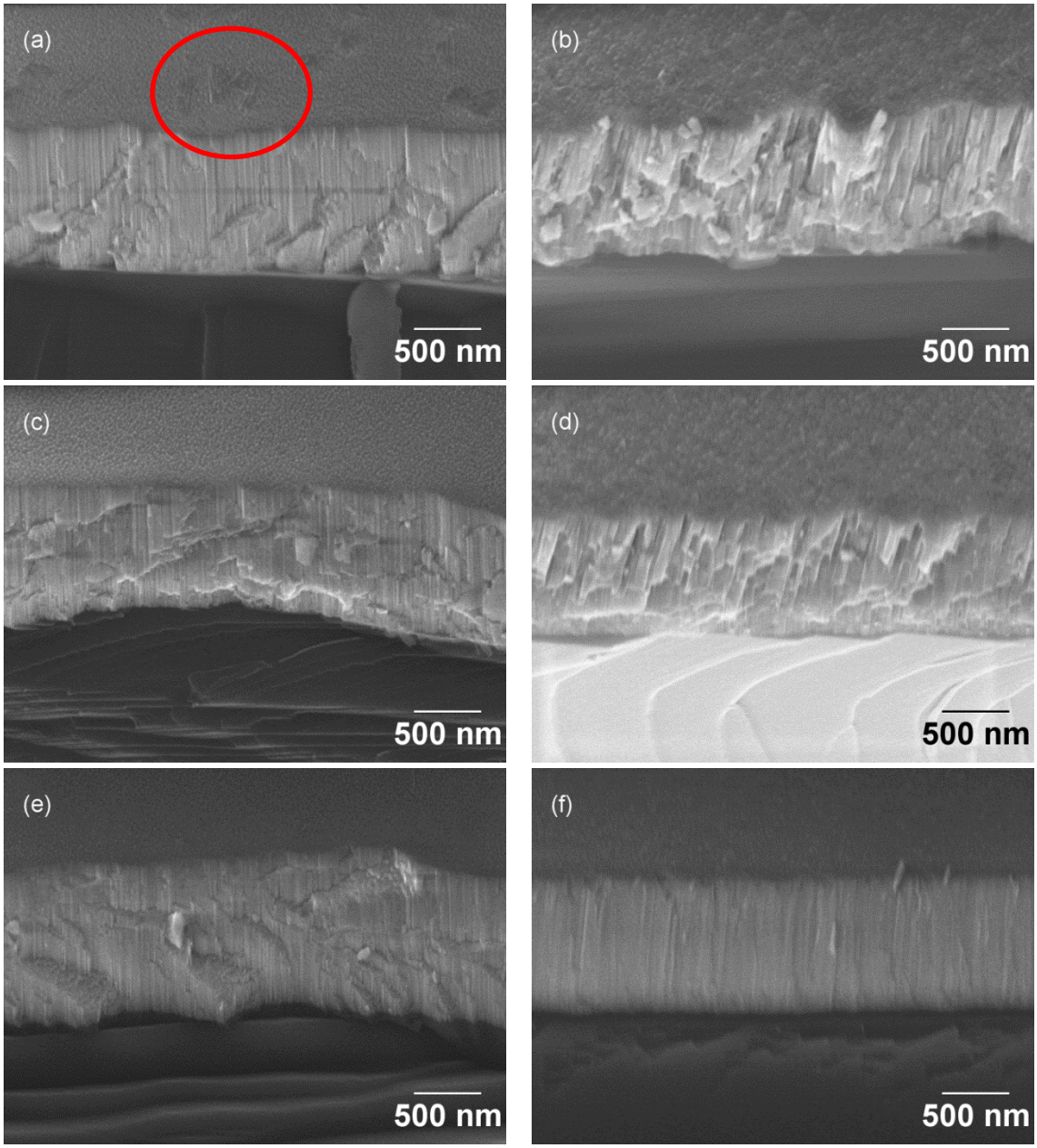

Figure 4-9 SEM cross-sectional image of the samples deposited at (a) TSD = 54 mm, wafer center, (b) TSD = 54 mm, wafer edge, (c) TSD = 58 mm, wafer center, (d) TSD = 58 mm, wafer edge, (e) TSD = 65 mm, wafer center (f) TSD = 65 mm, wafer edge

From the cross-section of the wafer center, the columnar microstructure perpendicular to the substrate could be observed from all the samples. Interestingly, there are the triangular shape crystallites on the surface of the sample TSD = 54 mm (Figure 4-9 (a)). The cross-section of the wafer edge shows different trend compared to wafer center, which is expected from FWHM values. While the TSD is 54 mm, tilt grains with low grain density are dominating in the cross-section, and it shows the mixture of the vertical grains and tiled grains can be seen in the case of TSD = 58 mm. When the TSD is increased further to 65 mm, the cross-section finally shows dense columnar grains along the thickness direction. The microstructure evolution concurs the results of the FWHM values difference as a function of the TSD, the homogeneity of crystalline quality as well as microstructure is obtained only when TSD = 65 mm.

4.2.4 Discussion and summary

In this section the evolution of crystalline quality and microstructure as a function of the TSD was shown, the crystalline quality of the AlN was the most uniform across the wafer when the TSD = 65 mm. The microstructure of the wafer center was not evolving in a visible trend as a function of the TSD, however the microstructure of wafer edge was depending on the TSD strongly. The tilting of the grains is observed with decreased TSD, the main reason is the co-sputtering configuration, as mentioned in the previous section.

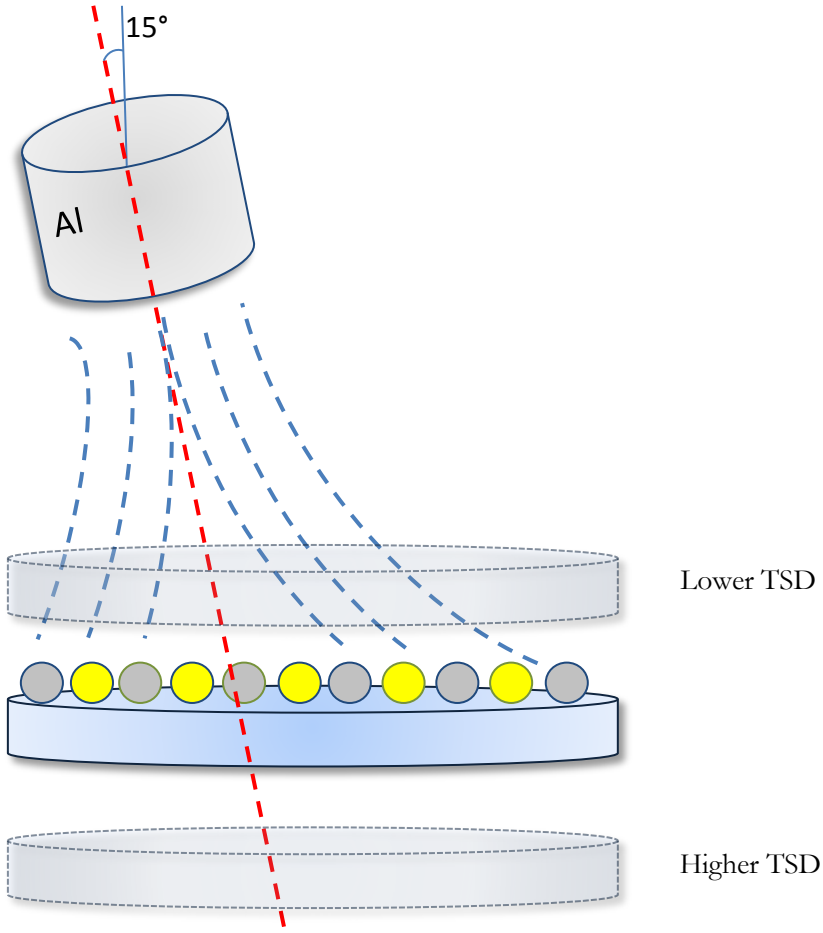

Figure 4-10 Schematic figure of the sputtering set up when the TSD is changing.

As shown in Figure 4-10, the configuration during process under different TSD is considered. When the process pressure is relatively low, the sputtering species experience less collisions and high kinetic energy when they land on the substrate surface. However, different path length of the sputtering species could lead to different kinetic energy of the particles. Therefore the microstructure at the wafer edge is observed at TSD < 65 mm. When the TSD is increased to 65 mm, the kinetic energy of the particles at the wafer edge are high enough and the difference of the kinetic energy of different localized area at wafer edge can be ignored, that is the reason the dense columnar grains in out-of-plane direction are observed. When the TSD is further increasing, the condition of particle collision and kinetic energy of the incoming sputtering species is similar to increase the process pressure. The increasing probability of the collision leads to low kinetic energy and thus the crystalline quality is degraded.

Furthermore, the FWHM values vs. TSD plot showed the same crystalline quality at the wafer center and wafer edge at 65 mm TSD. If the FWHM values and microstructure are considered as the results mainly caused by the configuration and the kinetic energy of sputtering species, then under these sputtering conditions the virtual "focus" point of this co-sputtering chamber is defined as 65 mm. Certainly, if the sputtering condition changed, e.g., the substrate size is changed from 100 mm to 200 mm, the target size, or the tilting angle of the target is changed, the "focus" point has to be found again.

4.3 Influence of the N_2 concentration (N_2 / (Ar + N_2))

By tuning the processing pressure and the TSD, the microstructure and also the crystalline quality of the AlN/Si were optimized. Columnar microstructure and pebble like surface morphology are observed both in the wafer center and wafer edge. However, during the change of the TSD, there are also abnormal microstructure (triangular shape in Figure 4-9 (a)) observed on the sample surface, it is existing together with columnar structure. Therefore we are now focusing more on the surface morphology to find the correlation of the sputter parameter and the abnormal grain formation.

In this sample series, the N_2 ratio (expressed as N_2 / (Ar + N_2)) will be regulated for different samples to study the crystalline quality and microstructure. The sputtering parameters are shown in Table 4-3, 1100 nm AlN thin films were sputtered on the 100 mm Si(001) wafer. Base pressure and process pressure are kept the same as in the Chapter 4.2. TSD and heater temperature are 65 mm and 500°C, respectively.

Table 4-3 Overview of the deposition parameter of the N_2 concentration variation

Parameter	Value
P_{Al}	1000 W
Process pressure	9.5×10^{-4} mbar
Target-to-substrate distance	65 mm
N_2 / (Ar + N_2)	64-100%
Heater temperature	500 °C
Film thickness	1100 nm

4.3.1 Growth rate and stress

The growth rate as a function of N_2 / (Ar + N_2) is shown in Figure 4-11 (a). As expected, the film growth rate is decreasing with the increasing N_2 / (Ar + N_2), which is also reported in the literature [118,131]. The main reason for this effect is, the mass of a single charged ion (Ar^+) is higher than the ionized molecule (N_2^+). When they are bombarding the targets, higher mass leads to higher kinetic energy, thus the sputtering yield is higher with the single charged ion (Ar^+). The target poisoning is often reported in the literature [132,133], which is normally found in the DC reactive magnetron sputtering with N_2 and Ar gas mixture. Because of the DC-pulse function, there is no obvious poisoning effect observed when the high N_2 / (Ar + N_2) is used in the sputtering process. In Figure 4-11 (b) the intrinsic stress is shown, it evolves in a non-linear trend with respect to the N_2 / (Ar + N_2). The stress is decreasing from 550 MPa for 64% N_2 to 440 MPa for 90% N_2 and again increasing to 520 MPa in the 100% N_2. The trend of the decreasing stress with more N_2 is also mentioned in the literature [134],

that the N_2 will bring more ion bombardment and due to the impinging effect, the film is more compressive stressed. However, when the N_2 / (Ar + N_2) is reaching 100%, the stress has different behavior as lower N_2 concentration, further studies are necessary to reveal the sudden change of the stress.

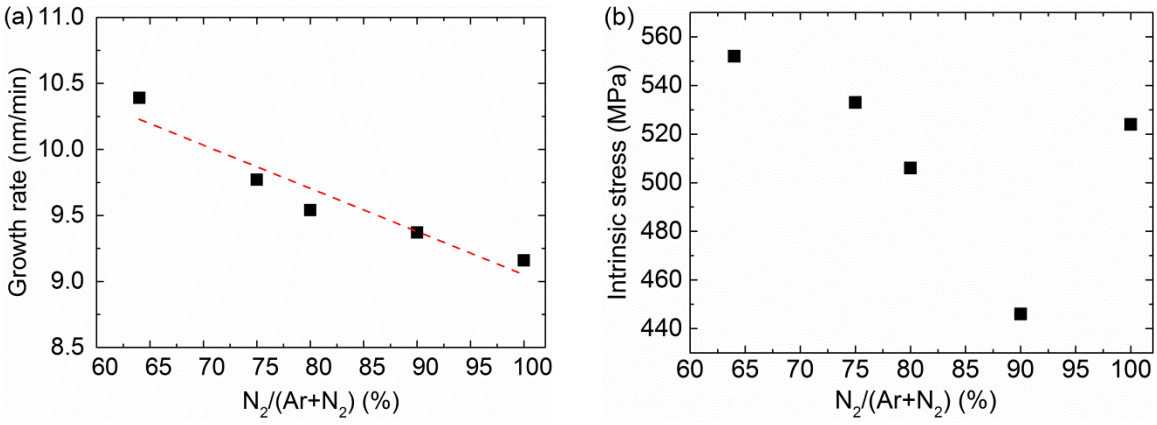

Figure 4-11 (a) Growth rate and (b) Film stress of sputtered thin film AlN as a function of the N_2 / (Ar+N_2)

4.3.2 Microstructure and surface morphology

To determine the surface microstructure, SEM surface images were recorded for different cases of N_2 / (Ar + N_2) (Figure 4-12 (a) and (b)). When we compare the surface morphology of the N_2 / (Ar + N_2) = 64% and 100%, the small amounts of the abnormal grains are observed and marked on the SEM picture. The lateral size of grain is in the range of hundred nanometers. The sample with N_2 / (Ar + N_2) = 100% has pebble like morphology on the surface, no abnormal grain is observed. Typically, the well c-axis oriented AlN shows pebble-like surface morphology [6,8,106,135,136]. In order to investigate the correlation of the N_2 / (Ar + N_2) on the quantity of the abnormal grain, the density of abnormal grain is plotted as a function of N_2 / (Ar + N_2) (Figure 4-12 (c)). Generally the density of the abnormal grain does not excess 0.1 /um², meaning in 100 μm² AlN surface there are no more than 10 abnormal grains. Furthermore, the density is reducing with increasing N_2 / (Ar + N_2) and it reaches 0 at N_2 / (Ar + N_2) = 100%, while in the wafer center it is more dependent on the N_2 / (Ar + N_2).

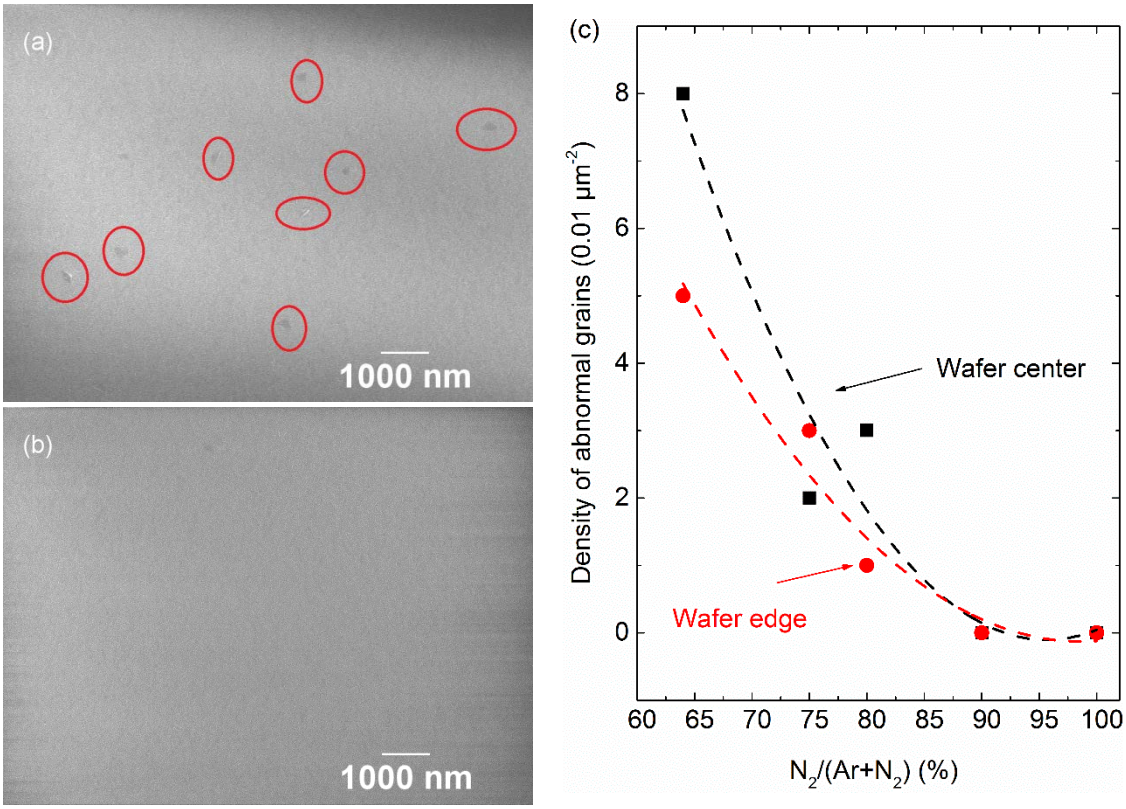

Figure 4-12 (a) SEM surface morphology of the AlN with N_2 / (Ar + N_2) = 64%, wafer center, the abnormal grains are marked with circles; (b) SEM surface morphology of the AlN with N_2 / (Ar + N_2) = 100%, wafer center; (c) density of the abnormal grain at the wafer center and at the wafer edge as a function of N_2 / (Ar + N_2), the lines are a guide for the eye.

4.3.3 Crystallographic orientation and crystalline quality

Due to the abnormal graind found in the AlN with low N_2 / (Ar + N_2) ratio, XRD 2θ/θ scans of AlN with N_2 / (Ar + N_2) = 64% and 100% are compared in Figure 4-13. The observed reflections are "Si" 002, AlN 0002, Si 004 and AlN 0004 for both samples, the peak position and the peak intensities are similar in both samples. It could be concluded that the low density abnormal grains observed in AlN thin film.

The trend of the rocking curve FWHM of AlN 0002 reflection as a function of N_2 / (Ar + N_2) is shown in Figure 4-14. The FWHM is increasing with the increasing N_2 / (Ar + N_2) for both wafer center and wafer edge with almost the same trend. It shows at the wafer center and edge 1.58°, 1.64° for N_2 / (Ar + N_2) = 64% and 1.66°, 1.71° for N_2 / (Ar + N_2) = 100%, respectively. The differences of the value of the rocking curve ω-FWHM between center and edge are almost constant during the increasing of the N_2 / (Ar + N_2). If we compare it to the rocking curve FWMH change in the process pressure or TSD series, such a low density of the abnormal microstructure is difficult to detect from XRD 2θ/θ scans and FWHM values.

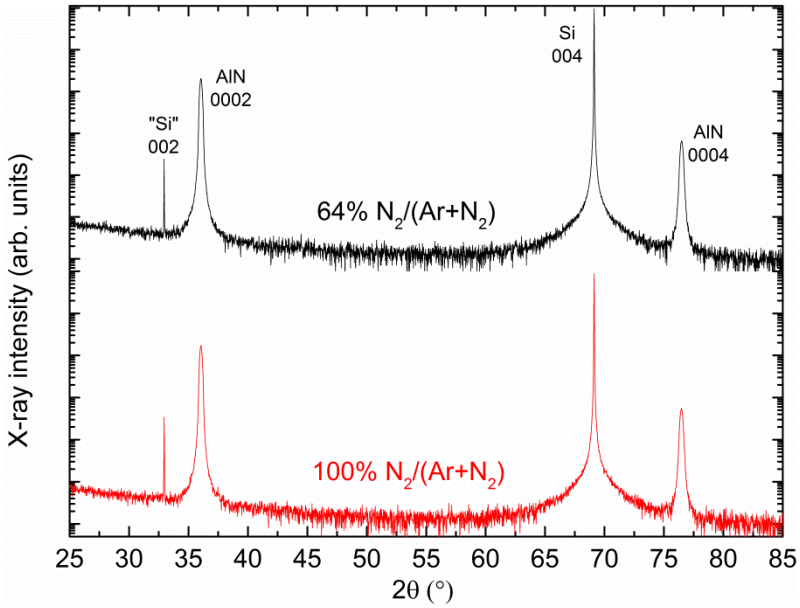

Figure 4-13 XRD 2θ/θ scans for the AlN grown with 64% and 100% $N_2/(Ar+N_2)$, measurements were done at the wafer center.

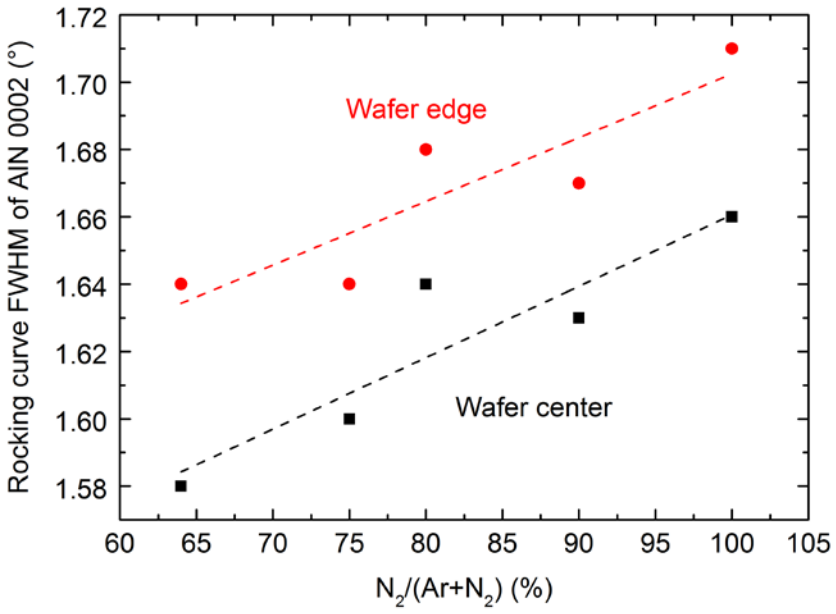

Figure 4-14 Rocking curve FWHM of AlN 0002 reflection as a function of N_2 concentration, the lines are the guides for the eye

4.3.4 Discussion and summary

According to the SEM images, the abnormal grains exist when the N_2 / (Ar + N_2) is in a lower value, and will disappear with increasing N_2 / (Ar + N_2). Furthermore, the nitrogen gas during the sputtering leads to lower growth rate due to the low yield of the N^{2+} than Ar^+ ions. This phenomenon is reported

in the literature [8,106], Reusch *et al.* [106] found abnormal grains in higher processing pressure, and it is less sensitive to the N_2 concentration, which is different as observed in this work.

However, more detailed characterization about the abnormal microstructure should be carried out, physical properties such as crystalline orientation, electrical properties, and other influences of the abnormal microstructures should be determined. Due to the low density abnormal microstructure in the AlN/Si film, this issue is not simply distinguished by the XRD but only SEM figures.

4.4 Summary

In this chapter, the sputtering deposition parameters: process pressure, TSD, and gas ratio are optimized to achieve wurtzite *c*-axis oriented AlN thin films on Si(001) substrates. The optimization is done in the co-sputtering configuration with single Al-target, therefore the process window of AlN is a perfect reference of the AlScN sputtering deposition with the same setup.

In the processing pressure variation, the influence of the process pressure on microstructure of the AlN/Si is observed, the low density inhomogeneous V-shape growth and tiled columnar growth are caused by the high process pressure. In the higher process pressure, the microstructure was different of different position on the wafer, which leads to the degrading of the crystalline quality at the edge of the wafer. Due to decreasing the kinetic energy of the sputtering species and the shadowing effect dominating in the sputtering process. In this case the c-axis orientation still exists in the sputtered AlN film, but the crystalline quality is decreased. The kinetic energy is higher in the lower process pressure due to less collisions, leading a dense columnar microstructure in cross-section and pebble like surface morphology. The crystalline quality was much better and more homogenous across the wafer. The piezoelectric coefficient d_{33} was also improved.

Second, TSD was varied between 40 and 70 mm. In the co-sputtering setup the Al-target and Sc-target are 15° tiled (Figure 4-10). Therefore the change of the TSD is actually influencing not only the vertical distance between the substrate and the target but also the "focus" point on the substrate surface. In the variation, the AlN/Si sputtered under 65 mm has the smallest difference of the AlN 0002 rocking curve ω-FWHM regarding wafer center and wafer edge, which could be also confirmed that the dense columnar microstructure of the AlN sputtered under 65 mm. The last but not least, the density of abnormal grains with triangular shape was decreased at TSD = 65 mm.

Later on, the N_2 concentration is investigated to solve the abnormal grains. With the achievable range of the gas ratio, the abnormal grains were still in a low density up to 0.1 /um². The SEM figure so far was the only way of characterization. By increasing N_2 concentration the density of abnormal grains decreased to zero. However, the investigation of the abnormal grains, crystallographic orientation, influences of the piezoelectric coefficient cannot be conducted due to the low density of the abnormal grains.

Finally, the process window of high quality wurtzite c-axis oriented thin film AlN was defined. Based on the process parameters of the AlN, the AlScN thin film will be deposited and described in the following chapter.

5 AlScN thin film deposition

This chapter is focused on the deposition process development part of AlScN. As a novel material first introduced by Akiyama *et al.* [3]. in 2009, the challenge has been the obtaining of the high piezoelectric properties [4] as well as the sufficient crystalline quality concerning the metastability in high Sc concentration. In this chapter, two solutions and two improvements are introduced. The two solutions are: 1) the investigation and elimination of the abnormal grains, 2) solution of the possible degraded crystalline quality in the high Sc concentration. The two improvements are: 1) high piezoelectric coefficient which is comparable to the state-of-the-art, 2) sputter deposition of c-axis oriented epitaxial $Al_{1-x}Sc_xN/Al_2O_3$ thin films.

When the AlScN thin films are sputtered with similar sputtering parameter as AlN/Si thin films, abnormal grains are found with even higher density. Therefore GIXRD technique is used to confirm the misorientation and its correlation to the piezoelectric response is established. Through the combination of tuning N_2 concentration and TSD, the misoriented grains are eliminated in the $Al_{1-x}Sc_xN$ thin films. This work has been published in paper [126].

After the influence of the misoriented grains was reduced to the minimum, the partial power of the Al- and Sc-magnetrons was then adjusted to achieve higher Sc concentration, to achieve higher performance of the acoustic devices. In order to determine Sc concentration, quantitative EDX measurement procedure was established. Based on the literature, when the Sc concentration x is higher than 0.4, phase instability is increasing especially deposited at higher heater temperatures [50,56]. By optimizing the heater temperature, $Al_{1-x}Sc_xN/Si$ with high Sc concentration up to x = 0.46 is sputtered and with high crystalline quality. The piezoelectric coefficient is measured and corrected by the mechanical properties of the $Al_{1-x}Sc_xN$ and substrate, the value is comparable or even higher than the state-of-the-art. The last part describes the magnetron sputter epitaxy of $Al_{1-x}Sc_xN/Al_2O_3$ with epitaxial relationship, in which the crack issue caused by the intrinsic stress is solved.

5.1 Abnormal grains in AlScN

The abnormal grains were observed in the AlN using different N_2 / (Ar + N_2) ratio. However, in the AlN it was no more than 10 grains per 100 μm^2, which means in a relatively low density. Furthermore, there are still some questions to be answered. How is the abnormal microstructure in AlScN? What properties of AlScN will be changed by abnormal microstructures? How to improve microstructure by optimizing the sputtering process? In this part the influence of abnormal microstructure in the AlScN will be analyzed in detail, from crystallographic orientation to piezoelectric properties, and finally the N_2 concentration and TSD will be optimized to reduce the density of these abnormal microstructures.

Table 5-1 Overview of the deposition parameters of AlScN in the abnormal microstructure study

Parameter	Value
$P_{Al} + P_{Sc}$	1000 W
Process pressure	9.5×10^{-4} mbar
Target-to-substrate distance	55-75 mm
$N_2 / (Ar + N_2)$	50-100%
Heater temperature	500 °C
Thin film thickness	900-1200 nm

As shown in Table 5-1, 900-1200 nm thick AlN and $Al_{0.87}Sc_{0.13}N$ thin films were prepared on Ø = 100 mm Si(001) substrates in Ar/N_2 gas mixture from Al and Sc targets (Ø = 100 mm). Before the deposition, the process chamber base pressure was $< 5 \times 10^{-8}$ mbar. The Si (001) substrates were cleaned using ICP etching in Ar atmosphere to improve the AlScN nucleation behavior [123]. All depositions were made at heater temperature of 500 °C, the total $Ar + N_2$ flow was kept constant at 20 sccm, and the individual gas flows were controlled by mass flow controllers to provide the specific N_2 gas concentration, expressed as $N_2 / (Ar + N_2)$. The total sputtering power ($P_{Al} + P_{Sc}$) was kept constant at 1000 W, i.e. $P_{Al} = 1000$ W for AlN, and $P_{Al} = 800$ W, $P_{Sc} = 200$ W for $Al_{0.87}Sc_{0.13}N$. Pre-sputtering of the targets was performed prior to film deposition with a closed shutter for 1 minute in Ar/N_2 mixture.

In order to evaluate the influence of sputtering parameters on surface morphology and microstructure of $Al_{1-x}Sc_xN$ thin films, two sample series were prepared as follows: (1) sample target-to-substrate distance (TSD) was fixed at 65 mm, and the N_2 concentration was varied from 50 to 100%; (2) N_2 concentration was fixed at 100%, while TSD was set to 55, 60, 65, 70, and 75 mm. As a reference, AlN thin films with TSD 65 mm and 100% N_2 concentration were also prepared based on optimized AlN growth process described in previous chapter

5.1.1 Compositional analysis

To investigate the possible influence of N_2 concentration in the gas mixture on thin film composition, $Al_{1-x}Sc_xN$ films were sputtered at TSD = 65 mm, $N_2 / (Ar + N_2)$ = 50-100% and Sc concentration was determined by EDX (Figure 5-1). As the EDX analysis revealed $x = 0.13 \pm 0.02$ for all N_2 concentrations (uncertainty is discussed in [5,52]), indicating that within the measuring accuracy of EDX the variation of N_2 concentration had very little influence on the Sc concentration. The same Sc concentration was also confirmed by secondary ion mass spectroscopy measurements.

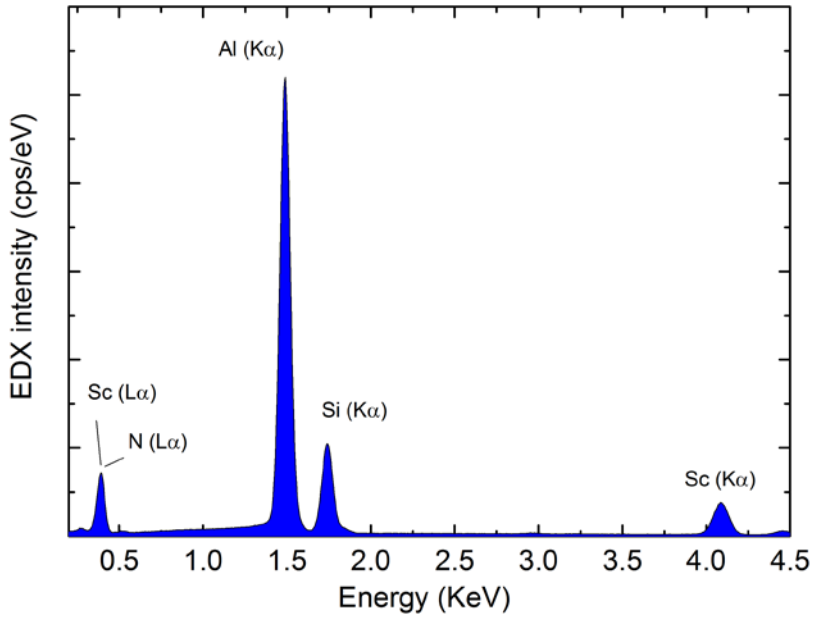

Figure 5-1 EDX spectra of the $Al_{0.87}Sc_{0.13}N$ with N_2 / (Ar + N_2) = 100 %, TSD = 65 mm

5.1.2 Crystallographic orientation and crystalline quality

Figure 5-2 shows the $2\theta/\theta$ scans for AlN and $Al_{0.87}Sc_{0.13}N$, both sputtered at TSD = 65 mm and N_2 / (Ar + N_2) = 100%. Only the Si 002 Renninger reflection, AlN or $Al_{0.87}Sc_{0.13}N$ 000*l* (*l* =2, 4) reflections are present, suggesting AlN and $Al_{0.87}Sc_{0.13}N$ films to be preferentially c-axis oriented. Additional $2\theta/\theta$ scans for the $Al_{0.87}Sc_{0.13}N$ with (1) N_2 / (Ar + N_2) = 50, 60, 70, 80, 90, and 100%, TSD = 65 mm and (2) N_2 / (Ar + N_2) = 100%, TSD = 55, 60, 65, 70, and 75 mm (not shown) also indicate c-axis oriented thin films, meaning that changing these growth parameters had no influence on the preferential film orientation.

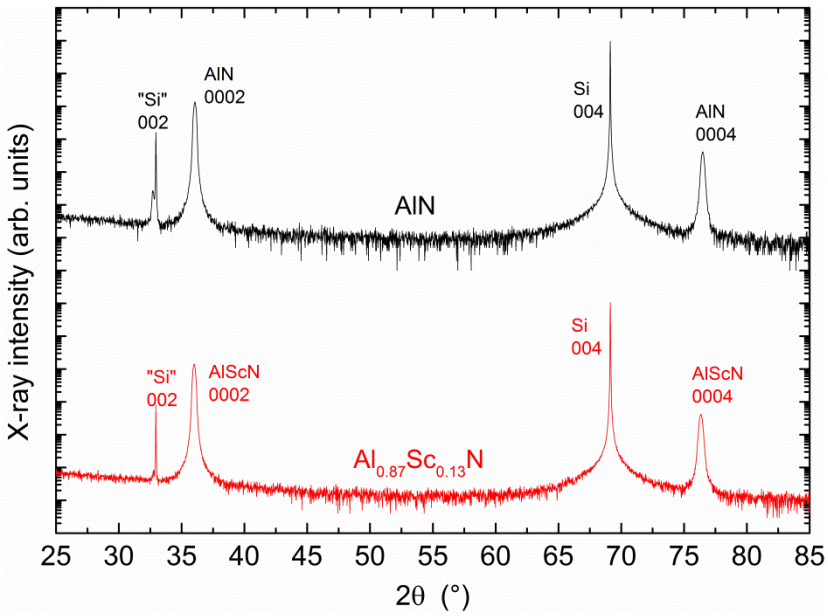

Figure 5-2 X-ray diffraction patterns for the (a) AlN and (b) $Al_{0.87}Sc_{0.13}N$ grown at target-to-substrate distance of 65 mm and 100 % N_2 concentration. [126]

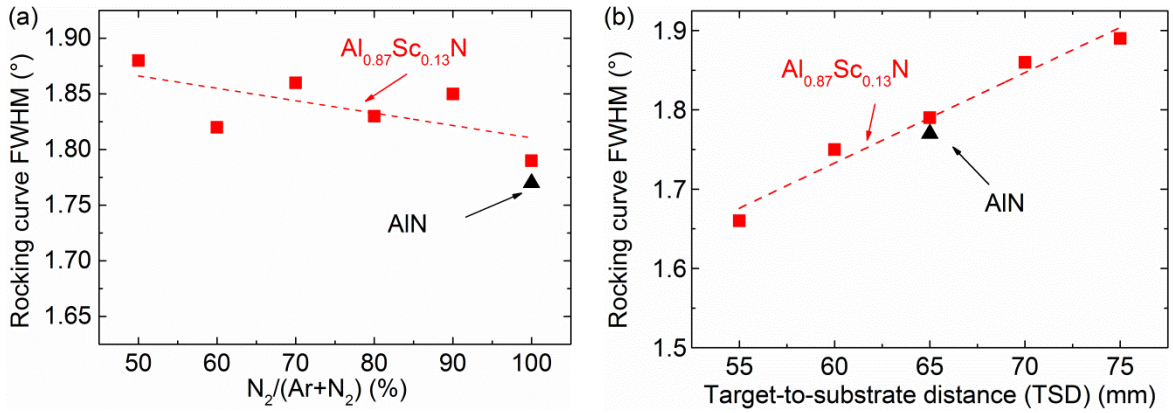

Figure 5-3 FWHM of AlScN (red squares) and AlN (black triangle) 0002 rocking-curve as a function of (a) N_2 / (Ar + N_2) from 50 to 100%, target-to-substrate distance is fixed at 65 mm (b) target-to-substrate distances from 55 mm to 75 mm, N_2 / (Ar + N_2) = 100%. The lines are a guide for the eye. [126]

The FWHM of the $Al_{1-x}Sc_xN$ 0002 rocking curve for all samples was < 2° (Figure 5-3), indicating a high degree of c-axis orientation [56]. However, in the Figure 5-3 (a) the rocking curve FWHM decreases slightly from 1.88° for 50% N_2 to 1.79° for 100% N_2 suggesting an improvement in crystalline quality when using more N_2 in the process gas mixture. In Figure 5-3 (b) the FWHM of 0002 rocking curve is plotted for samples with different TSD grown at 100% N_2. With increasing TSD, FHWM increased from 1.66° to 1.89°. Although the samples at TSD = 55 mm and 60 mm showed lower FWHM, both of them exhibit increased thickness inhomogeneity of ~6% (not shown), therefore TSD = 65 mm for further investigations is chosen. The rocking curve FWHM of AlN sputtered under 100% N_2 concentration and 65 mm TSD is also shown in Figure 5-3 as a reference (1.77°). Comparing the rocking curve FWHM of AlN and $Al_{0.87}Sc_{0.13}N$ films grown under comparable growth conditions, there is no obvious degradation of crystalline quality.

Based on the results of Mishin *et al.* [7], high degree of c-axis orientation contributes to strong piezoelectric response. According to [137] FWHM of 0002 rocking curve and the presence of non-0002 reflections are important factors when optimizing the piezoelectric quality of AlN thin films. In this case, based on $2\theta/\theta$ scans and measurements of rocking curve FWHM one can see: (1) all films investigated in this work showed only $000l$ (l = 2, 4) reflections in $2\theta/\theta$ scans; (2) the change in FWHM for different N_2 concentrations is less than 0.1°. Based on $2\theta/\theta$ scans, N_2 gas concentration has little influence on the $Al_{0.87}Sc_{0.13}N$ thin film crystalline quality. In order to investigate the influence of growth parameters and the possible defects not detected by XRD $2\theta/\theta$ scans, the analysis of surface morphology of $Al_{1-x}Sc_xN$ thin films was also performed and the results are summarized in the next section.

5.1.3 Surface morphology and microstructure

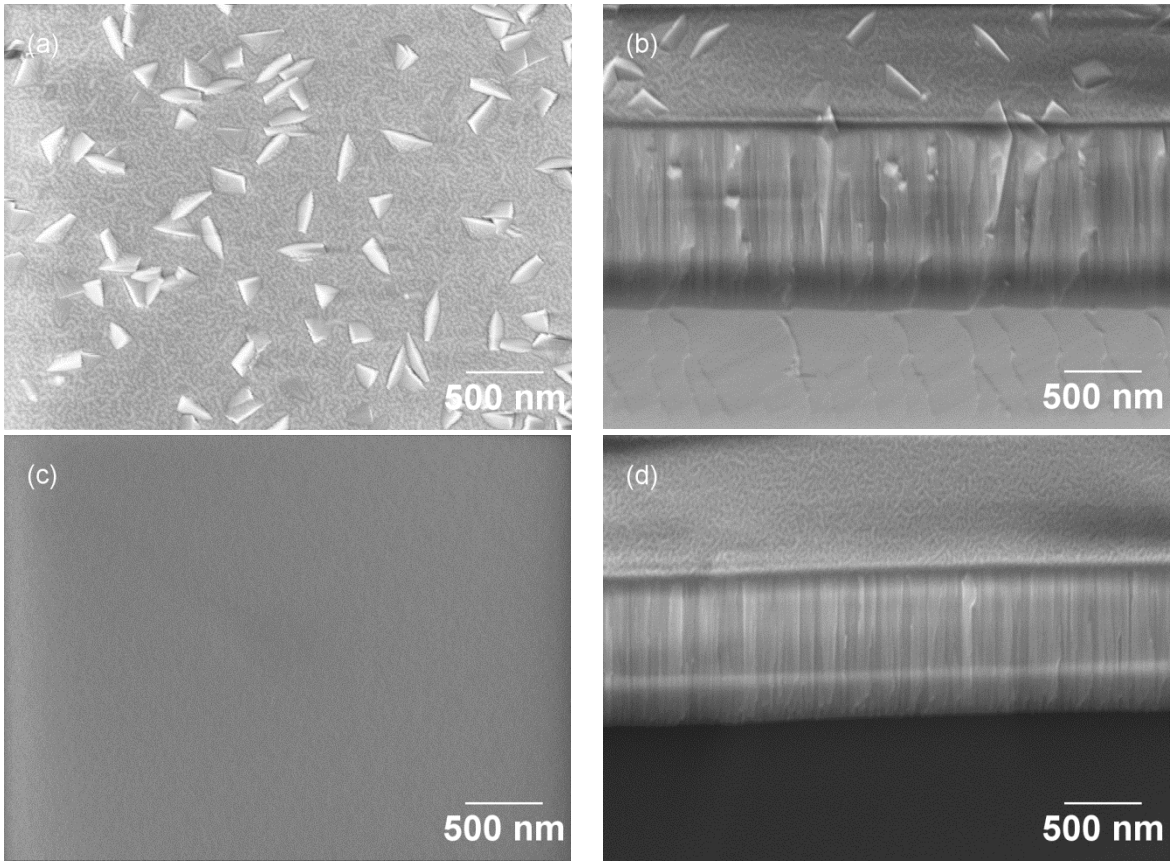

Figure 5-4 Scanning electron microscopy images of $Al_{0.87}Sc_{0.13}N$ thin films: (a)-(b) are the planar and cross-sectional images of films grown under 50% N_2 concentration and (c)-(d) are the films grown under 100% N_2 concentration, respectively. [126]

In order to examine the microstructure of the $Al_{1-x}Sc_xN$, SEM was used for planar and cross-sectional imaging of the samples. Figure 5-4 (a)-(b) shows the films grown with 50% N_2 concentration. Large triangular shape grains are randomly distributed on the surface and based on cross-sectional analysis (Figure 5-4 (b)) they start forming in the early stages of the growth. Literature suggests that these abnormal grains might not be c-axis oriented [8,9,138] and described these structures as misoriented grains. Further investigations of their structure as well as influences on piezoelectric properties are discussed below. In the case of 100% N_2 concentration, the films have dense, homogenous, pebble-like surface morphology (Figure 5-4 (c)) and well developed columnar structure visible in cross-section (Figure 5-4 (d)) of the thin films. The surface roughness root-mean square (R_{rms}) value from AFM measurements (not shown) is below 2 nm, indicating a very smooth surface.

Same as the observation from AlN films in previous chapter, based on the SEM results of the $Al_{0.87}Sc_{0.13}N$ sputtered under 50% and 100% N_2 concentration, the surface morphology is strongly dependent on N_2 concentration. To quantify this phenomenon, the density of misoriented grains in 10K magnification SEM micrographs was determined using ImageJ image processing program [139]. With increasing N_2 concentration the density of abnormal grains is decreasing (Figure 5-5), and this behavior can be divided into three regimes: (1) up to 60% N_2, where the density of misoriented grains is drastically decreased with increase in N_2 concentration; (2) 60% – 90% N_2, where relatively low density of misoriented grains is present, and with increasing N_2 concentration there is no obvious change

in surface morphology; and (3) 100% N_2, where the film surface is very uniform and smooth, and the density of misoriented grains is lower than 1 per 100 µm².

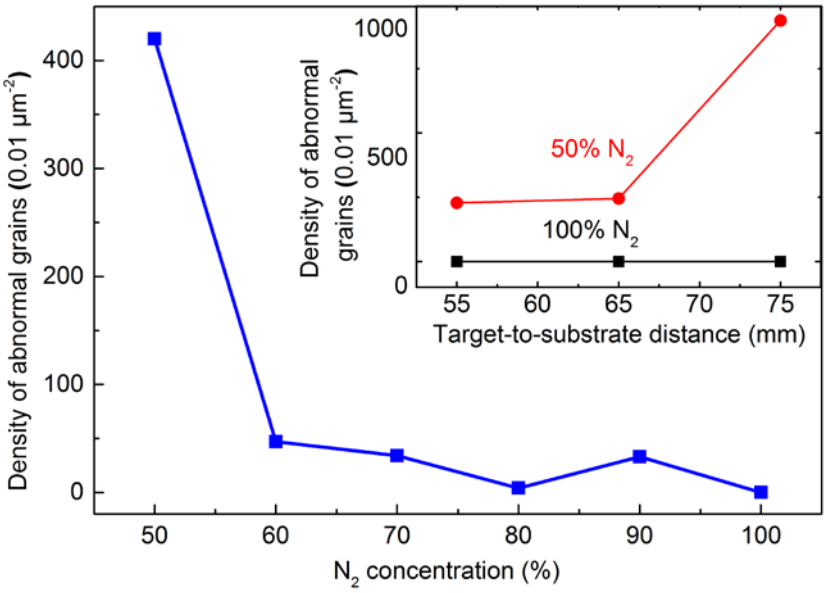

Figure 5-5 Number of abnormal grains in an area of 100 µm² as a function of N_2 concentration (large plot) and target-to-substrate distance (inset). In the N_2 series the TSD is kept at 65 mm. In the TSD series, 100% and 50% N_2 concentration are compared. The lines are a guide for the eye. [126]

In the samples grown at different TSD (Figure 5-5, inset), one can observe even a higher density of abnormal grains when the TSD is increased to 75 mm at 50% N_2 concentration. However, when the N_2 concentration is fixed to 100%, from 55 mm to 75 mm, surface of the films is free of abnormal grains, indicating that the N_2 concentration is the dominating factor during growth for controlling the density of abnormal grains.

5.1.4 Piezoelectric properties

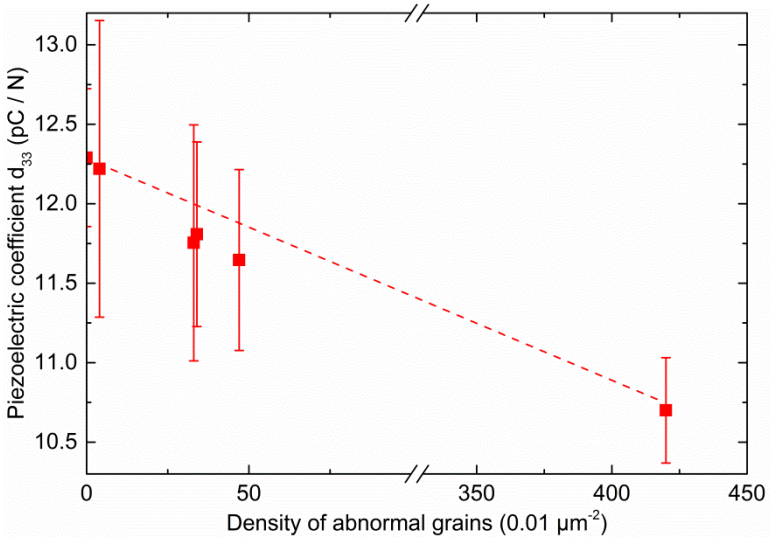

Figure 5-6 Average piezoelectric coefficient d_{33} as a function of number of abnormal grains in an area of 100 µm² (the line is a guide for the eye). [126]

Figure 5-6 shows the measured piezoelectric coefficient $d_{33,\,clamp}$ as a function of density of abnormal grains, all films were N-face polarity. $Al_{0.87}Sc_{0.13}N$ with highest density of abnormal grains showed lowest average piezoelectric coefficient $d_{33,\,clamp}$ = 10.7 pC/N. With decreasing density of abnormal grains the average piezoelectric response of the $Al_{0.87}Sc_{0.13}N$ films is increased. $Al_{0.87}Sc_{0.13}N$ deposited at 100% N_2 concentration was free of abnormal grains and had the highest average piezoelectric coefficient $d_{33,\,clamp}$ = 12.3 pC/N. AlN samples showed average piezoelectric coefficient $d_{33,\,clamp}$ = 7.3 pC/N, so the $Al_{0.87}Sc_{0.13}N$ without misoriented grains has almost 170% higher d_{33}, as compared to AlN and comparable to values found in literature [3,51,140]. Since the density of the abnormal grains had influence on the average piezoelectric coefficient $d_{33,\,clamp}$, the $Al_{1-x}Sc_xN$ samples were investigated by PFM in order to observe the piezoelectric properties on a nanoscale.

In Figure 5-7 (a)-(c), $Al_{0.87}Sc_{0.13}N$ sputtered at 50% N_2 concentration at TSD = 65 mm is shown. Figure 5-7 shows the surface topography. Here, one can see the large misoriented grains protruding from the surface, with their height in the range of 30 nm, sometimes even to 100 nm. In the piezoelectric amplitude mapping (Figure 5-7 (b)) the same grains show very low or no piezoelectric activity. Based on varying piezoelectric phase signal in the Figure 5-7 (c), the abnormal grains appear to have several different polarization directions.

PFM images of $Al_{0.87}Sc_{0.13}N$ sputtered with 100% N_2 concentration at TSD = 65 mm are shown in Figure 5-7 (d)-(f). The surface topography in Figure 5-7 (d) shows dense, homogenous surface with small pebble-like grains and all the grains have similar piezoelectric amplitude as shown in Figure 5-7 (e). In Figure 5-7 (f) polarization phase map is showing single phase, where irregularities at the grain boundaries are a known artefact when performing PFM measurements at contact frequency [88,128]. The sample free of abnormal grains has continuous and homogenous N-face polarity, supporting the high piezoelectric response $d_{33,\,clamp}$ measured by the Berlincourt method.

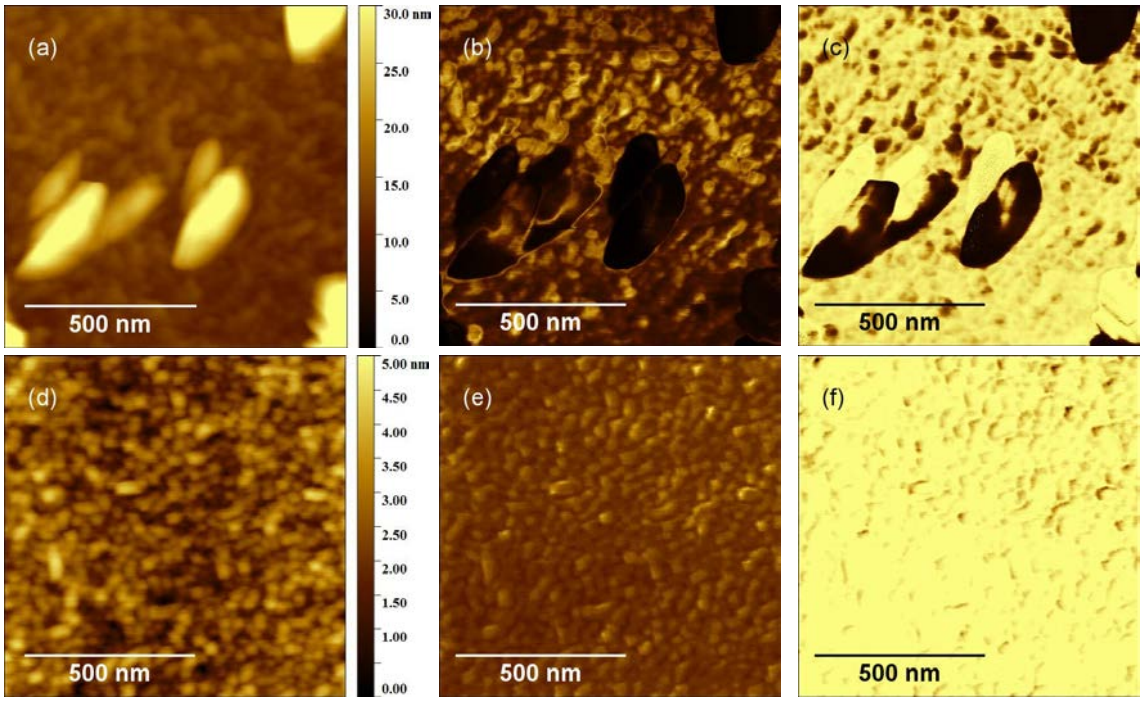

Figure 5-7 Piezoresponse force microscopy images of $Al_{0.87}Sc_{0.13}N$ grown with 50% and 100% N_2. (a) and (d) surface topography; (b) and (e) piezo-amplitude; (c) and (f) vertical piezo-phase. (a)-(c) for $Al_{1-x}Sc_xN$ prepared with 50 % N_2 concentration, at target-substrate distance of 65 mm; (d)-(f) for $Al_{0.87}Sc_{0.13}N$ prepared with 100% N_2 concentration, 65 mm TSD. In (c) and (f), bright and dark areas correspond to N-face and Al-face polarity, respectively. [126]

5.1.5 Grazing Incidence X-ray Diffraction (GIXRD)

Previous studies already discussed a lot about the characterization of high quality AlN and $Al_{1-x}Sc_xN$: typically, such films would have pebble-like surface morphology [6,8,106,135,136] and homogeneous columnar structure [36,128] can be observed in cross section. Additionally, $000l$ (l = 2, 4, 6) reflections in XRD $2\theta/\theta$ scan [3] and low rocking curve FWHM values indicate high degree of c-axis orientation. Higher piezoelectric response and homogenous polarity [141] enable improved piezoelectric performance.

However, to properly investigate the misoriented grains present in the underperforming AlScN thin films XRD $2\theta/\theta$ and SEM analysis is not enough. For example, Olivares *et al.* [8] used combination of XRD, infrared reflectance spectra, and AFM to determine the AlN film quality. Concerning the X-ray attenuation coefficient μ, the penetration depths of X-ray is in the 10 – 100 μm range [88]. Thus only negligible structural information is gained when investigating thin films with thicknesses of ~1 μm as it is in our case. The thickness-induced limitation can be overcome by using low angle XRD techniques, such as gracing incidence X-ray diffraction (GIXRD). With incidence angle ω = 0.3°, the X-ray path length through the thin film is increased and more detailed structural information about randomly oriented grains can be extracted.

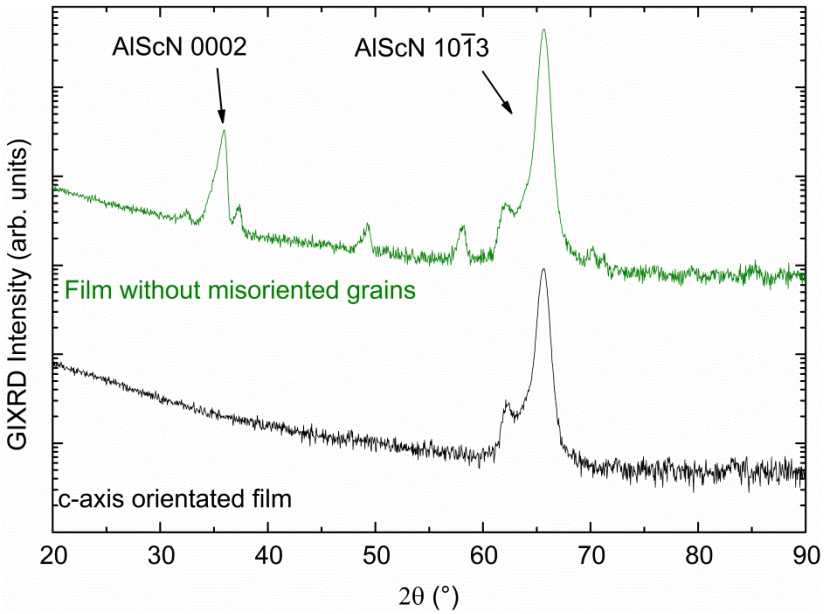

Figure 5-8 Grazing incidence X-ray diffraction (GIXRD) profile of $Al_{0.87}Sc_{0.13}N$ sputtered with 50 % N_2 and 100 % N_2 concentration. [126]

Figure 5-8 shows the comparison GIXRD spectra for $Al_{1-x}Sc_xN$ sputtered using 50% and 100% N_2 concentrations. At lower N_2 concentration the measurement shows multiple peaks corresponding to different AlScN orientations, indicating a presence of misoriented grains in the material. When the N_2 concentration is increased to 100% only the $Al_{1-x}Sc_xN$ 10$\bar{1}$3 reflection is observed, confirming a thin film with a single orientation.

5.1.6 Discussion and Summary

To understand the influence of misoriented grains on the piezoelectric response, we start with the crystallographic orientation: The samples with large abnormal grains observed in SEM show a mixture of orientations in GIXRD measurements, even though all of them still correspond to wurtzite type AlScN. Additionally, PFM shows that these grains don't behave the same way as their surroundings. Since only the c-axis oriented grains contribute to piezoelectric response, the average piezoelectric response increases for films where no misoriented grains are present.

It is apparent from cross-sectional SEM images that the misoriented grains form early during growth. Higher N_2 concentration leads to lower sputtering yield, and thus the sputtered species from Al and Sc targets have lower density as compared to lower N_2 concentration case. Consequently, there is lower possibility that AlScN clusters are formed already in the plasma before they reach the substrate and initiate the formation of the misoriented grains [106]. When tuning the TSD, the possibility of collision of the individual plasma species is increasing with higher TSD and the probability of forming misoriented grains is increased. In our case when the TSD is larger than 65 mm, the density of the misoriented grains is drastically increasing for 50% N_2 concentration.

The crystallographic orientation of the misoriented grains can be revealed by SAED (selected area diffraction) [9]. In the case of that study, a tilt of 60° to 90° for AlScN (0002) orientation in abnormal grains than the adjacent c-axis AlScN grains was observed, and explained by rocksalt structure in the embryonic nuclei reverting to the wurtzite phase and leading to a loss of c-axis orientation. Besides, the Sc segregation was also happening at the grain boundaries of these misoriented grains.

5.2 Sc concentration variation

In the previous section the misoriented grains were identified by GIXRD in AlScN thin film. The critical sputtering parameter for solving the misoriented grains was found to be the N_2 concentration N_2 / (Ar + N_2), which has a linear relationship with respect to the number of the misoriented grains in unit area of the surface. Afterwards $Al_{0.87}Sc_{0.13}N$ with dense and pebble like structure was obtained, columnar grains at the cross-section, c-axis orientation, high piezoelectric coefficient d_{33} and homogenous piezo-domains was achieved. However, as reported by Akiyama *et al.* [3] that the higher piezoelectric coefficient was achieved by higher Sc concentration, up to 43%.

In this part, the AlScN/Si with different Sc concentration is studied. First, the characterization procedure of EDX to measure the Sc concentration of the AlScN was established. As mentioned previously, the wurtzite phase and rocksalt phase could co-exist when the Sc concentration is higher than x = 0.4, due to metastability of AlScN. Therefore, the phase stability of the AlScN in high Sc concentration was studied and the heater temperature was thus optimized. Afterwards, the piezoelectric coefficient d_{33} was measured and corrected based on the relative hardness difference between AlScN layer and Si substrate. Finally the piezoelectric coefficient results were compared to the state-of-the-art for a better overview of this work.

Table 5-2 Overview of the deposition parameter of AlScN/Si with Sc concentration variation

Parameter	Value
$P_{Al} + P_{Sc}$	1000 W
Process pressure	9.5×10^{-4} mbar
Target-to-substrate distance	65 mm
$N_2 / (Ar + N_2)$	100%
Heater temperature	300-500 °C
Thin film thickness	900-1200 nm

Based on the previous studies of the microstructure, crystallographic orientation, crystalline quality etc., the processing pressure was set at 9.5×10^{-4} mbar for all of the sample to have the dense columnar growth and pebble like surface microstructure. N_2 concentration was kept at 100% and the flow was 20 sccm to be sure the minimum influence by the misoriented grains. TSD was kept at 65 mm to achieve promising microstructure. The total power of the Al and Sc magnetron were kept as 1000 W, the partial power to achieve specific Sc concentration was plotted, as shown in Figure 5-9. The partial power was adjusted according to the EDX determined Sc concentration x = 0, 0.06, 0.13, 0.23, 0.32, 0.41 and 0.46. Determination of the Sc concentration is going to be discussed in detail in the following section. The small concentration steps ensured that the trend of the properties evolution of the Sc concentration could be observed. The correlation of the P_{Sc} to the Sc concentration is not linear. Between 0% (AlN) to 14% the trend is rather linear, also the variation P_{Sc} is set for every 100 W. When the P_{Sc} is further increasing, the Sc concentration is increasing strongly, e.g., Sc concentration x = 0.41 for P_{Sc} = 450 W and Sc x = 0.46 for P_{Sc} = 475 W.

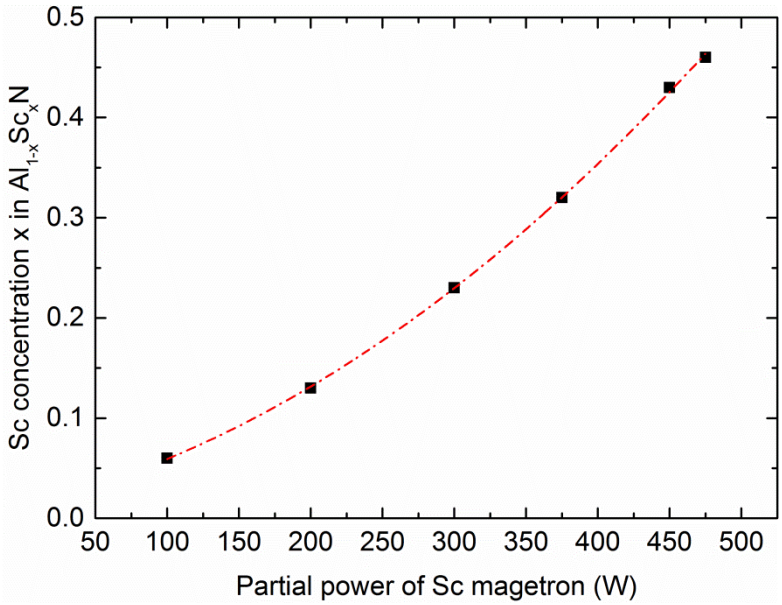

Figure 5-9 Plot of Sc concentration as a function of magnetron power of Sc target, the line is a guide for the eye.

5.2.1 Determination of Sc concentration

The co-sputtering configuration, it is very convenient to adjust the partial power and then tune the Sc concentration of the AlScN thin film. The concentration of the Sc in AlScN thin films had been pre-measured by SIMS and was used as reference sample, and the SIMS was calibrated accordingly. The samples with certain P_{Al} and P_{Sc} were first measured by SIMS, the Sc concentration in SIMS was determined. And then the sample was measured and used to calibrate the EDX, due to the measurement convenience and process time, later all the samples were measured by EDX.

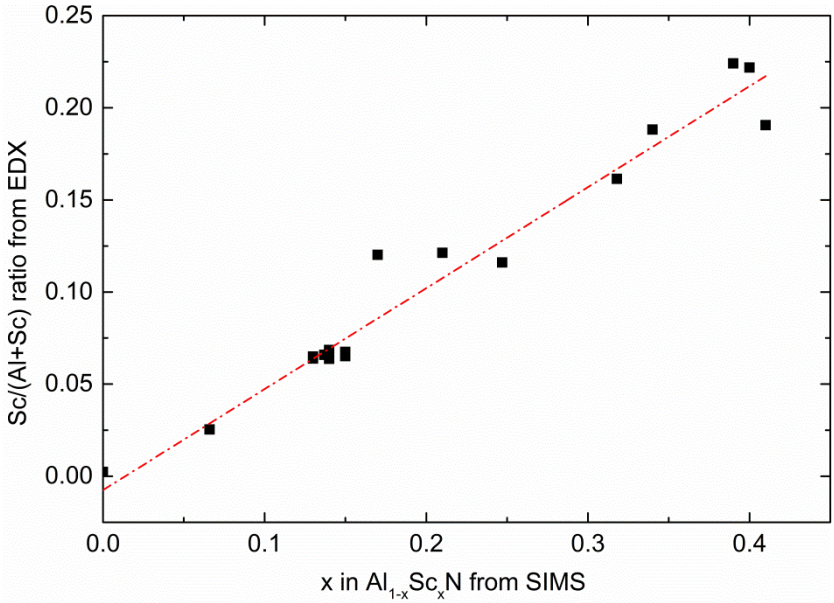

Figure 5-10 Intensity ratio Sc/(Al+Sc) measured in EDX as a function of SIMS measured Sc concentration, acceleration voltage EHT = 15 kV, the red dash line stands for the linear fitting of the EDX intensity ratio.

The composition of AlScN is assumed that (Al + Sc) : N = 1 : 1, so that the ratio of Sc / (Al + Sc) measured from EDX is used as x in $Al_{1-x}Sc_xN$, as shown in Figure 5-10. As mentioned in the previous paragraph, the reference and standard specimens have to be measured under same conditions due to the deviation induced by characterization parameter. Therefore, according to different EHT, the correlation of the EDX peak intensity ratio and composition measured by SIMS has to be adjusted, separately. The Table 5-3 shows the characteristic X-ray intensity under EHT = 15 kV for corresponding Sc concentration. The intensity ratio of Sc / (Sc + Al) measured from EDX spectra is quite linear compared to the Sc concentration by SIMS, the variation is x = ± 0.02 for Sc concentration in AlScN determined by EDX.

Table 5-3 Correlation of EDX intensity and Sc concentration

SIMS Sc %		0.06	0.13	0.23	0.32	0.41	0.46
EHT=15kV	Intensity Al	195687	104710	104414	89701	76392	132625
	Intensity Sc	4420	7240	13844	17623	22057	43671
Fitting	$C_{Sc} = (\frac{I_{Sc}}{I_{Sc}+I_{Al}} + 0.00754)/0.0000566$						

5.2.2 Temperature influences on the phase stability

The AlScN is metastable material [142] which has increasing mixing enthalpy with increasing Sc concentration, and the preferred phase is thus influenced by the processing temperature [3]. Therefore the $Al_{0.59}Sc_{0.41}N$ was sputtered on Si (001) with the different processing temperature.

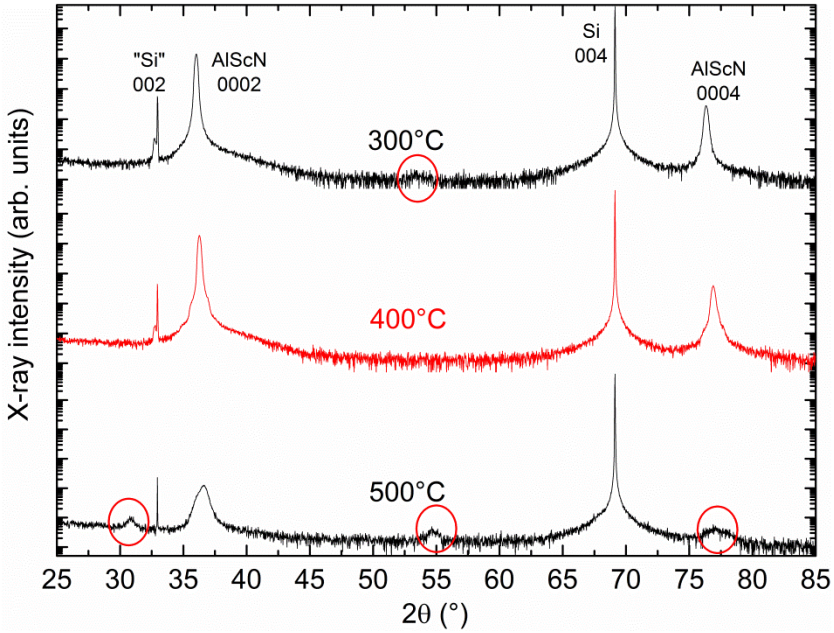

Figure 5-11 (a) X-ray 2θ/θ scans for the $Al_{0.59}Sc_{0.41}N$ grown at heater temperature from 300°C to 500°C

As shown in Figure 5-11, $2\theta/\theta$ scans of $Al_{0.59}Sc_{0.41}N$ show influence of the heater temperature. When the $Al_{0.59}Sc_{0.41}N$ was grown at 300 °C and 400 °C, AlScN 000l (l =2, 4) reflections is observed, indicating the preferred c-axis orientation. Here the $Al_{0.59}Sc_{0.41}N$ grown under 300 °C has a reflection around 2θ = 55° with a small intensity, which indicates non-wurtzite inclusion could form at such high heater temperatures. Furthermore, when the heater temperature is elevated to 500°C, the AlScN 0002 and 0004 reflection has weak intensity and broadening, especially the AlScN 0004 is almost invisible in the 500°C. Furthermore, the extra orientation at the peak positions 31°, 55° are already visible. However the 0002 reflection is still dominating in all of the samples. [3] The rocking curve FWHM also indicates the influence from the temperature (not shown here). The lowest value 1.26° is obtained at 400 °C, it becomes slightly higher at 1.51° when deposited at 300 °C. The distortion of the crystalline quality is observed when the temperature is at 500 °C, that the FWHM is reaching 4.5°.

5.2.3 Crystalline quality

The XRD $2\theta/\theta$ scans of AlScN up to x = 0.46 are shown in Figure 5-12. In all samles the AlScN 000l (l = 2, 4) reflections are observed, the peak position of AlScN 0002 and 0004 are around the 2θ = 36° and 76°, indicating the c-axis orientation of all the Sc concentration which is grown on the Si (001) wafer. It is reported in the literature that, in the higher Sc concentration x > 0.4, the probability to have extra orientation is high, including wurtzite AlScN (100), (101), (110) [57,103,143], strong peak shift in the first reported AlScN [3,51]. Here we could observe the peak position is with great intensity and the peak positions are around 36° when x ≤ 0.41, the 0002 reflection in $Al_{0.54}Sc_{0.46}N$ exists at 2θ = 36.5°. The peak shift towards both higher 2θ value [138,144] and lower 2θ value [56,80] is mentioned

in the literature. The relationship between peak position θ and c-lattice parameter is defined by the Bragg equation. According to the theoretical prediction[52], non-linear c-lattice parameter first increases up to 5.049 Å and then decreases to 4.981 Å. The non-linear peak position is fitting the trend of c-lattice parameter considering Bragg equation. Furthermore, other factors like lattice strain, volume and thermal strain, are also effecting the actual peak position, it cannot be considered as only clue to determine c-lattice parameter.

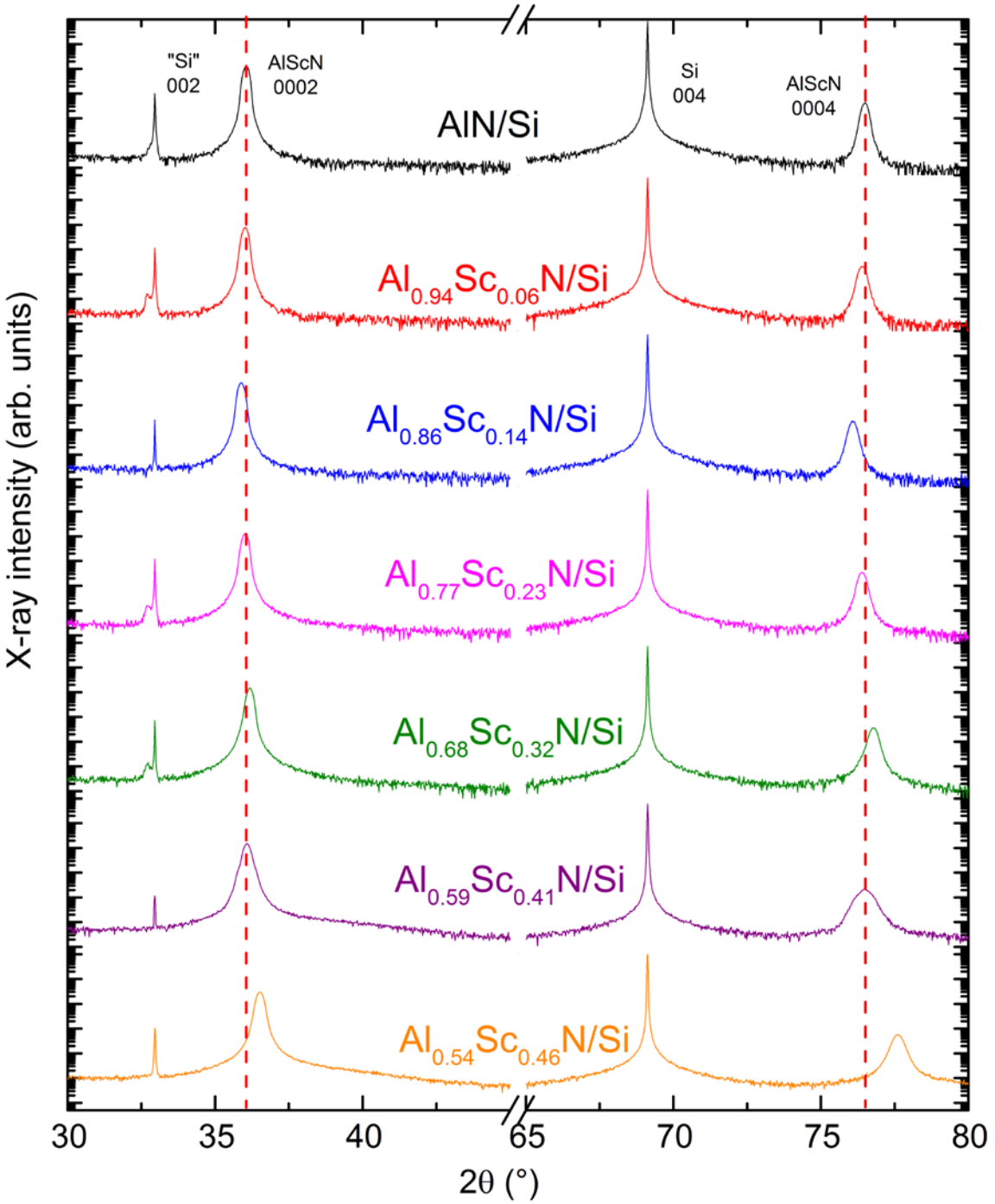

Figure 5-12 XRD 2θ/θ scans for the $Al_{1-x}Sc_xN$/Si up to x = 0.46, measurements was on wafer center from AlScN 0002 reflections to AlScN 0004 reflections

Figure 5-12 shows the rocking curve FWHM of the AlScN 0002 as a function of x in $Al_{1-x}Sc_xN$ thin film sputtered on Si(001) substrate. First, all the samples showed the FWHM < 2°, indicating good

material quality. The trend shows a decreasing FHWM as increasing Sc content, e.g., 1.9° in the AlN compared to 1.35° in $Al_{0.54}Sc_{0.46}N$, which indicating the increasing crystalline quality of the AlScN thin film as respect to the increasing Sc concentration. However, the mixing enthalpy of AlScN in the literature is increasing in the higher Sc concentration and leads metastability of the hexagonal structure [142], thus the higher Sc concentration should cause degrading of the crystalline quality. In the similar study regarding the Sc concentration in sputtered AlScN/Si recently, no significant correlation between 0002 reflection rocking curve FWHM and Sc concentration was observed [138,145].

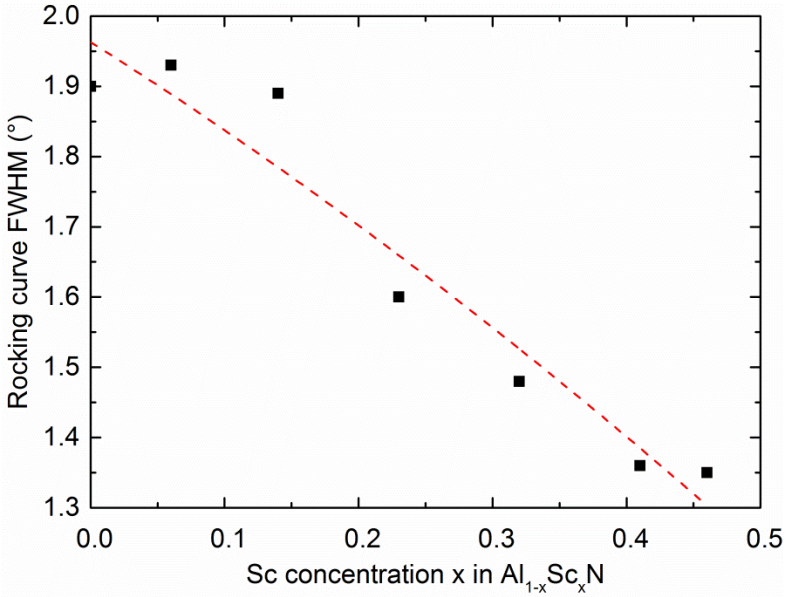

Figure 5-13 FWHM of AlScN 0002 reflection as a function of x in $Al_{1-x}Sc_xN$ thin film sputtered on Si(001) substrate, the line is a guide for the eye

5.2.4 Piezoelectric coefficient

To investigate the piezoelectric coefficient d_{33} as a function of the Sc concentration, piezoelectric coefficient $d_{33,\,clamp}$ was measured using Berlincourt method (Piezotest), the plot is shown in the Figure 5-14.

From the measured $d_{33,\,clamp}$ as a function of Sc concentration, the value for AlN and $Al_{0.54}Sc_{0.46}N$ is 7.3 ± 0.3 pC/N and 27.2 ± 0.9 pC/N, respectively. It brings a huge boost of the piezoelectric coefficient d_{33} in $Al_{0.54}Sc_{0.46}N$ compared to AlN by around 400%, similar to the 27.6 pC/N reported by Akiyama *et al.* [3] However the trend of the increasing d_{33} is not fitting to the measured value and theoretical prediction in the literature [3,53,104]. Although the Berlincourt method could characterize the piezoelectric coefficient, however, it measures effective coefficient of the sample and is influenced by the substrate stiffness. The real d_{33} is given when the stress is applied on the whole structure [146]:

$$d_{33} = d_{33,clamp} + 2d_{31}(S_{13} + \sigma/Y)/(S_{11} + S_{12}) \qquad 5\text{-}1$$

where the σ and Y are the Poisson ratio and Young's modulus of the substrate. In the actual calculation of measured d_{33}, d_{31} and S_{13} are using the simulated value reported in literature [53].

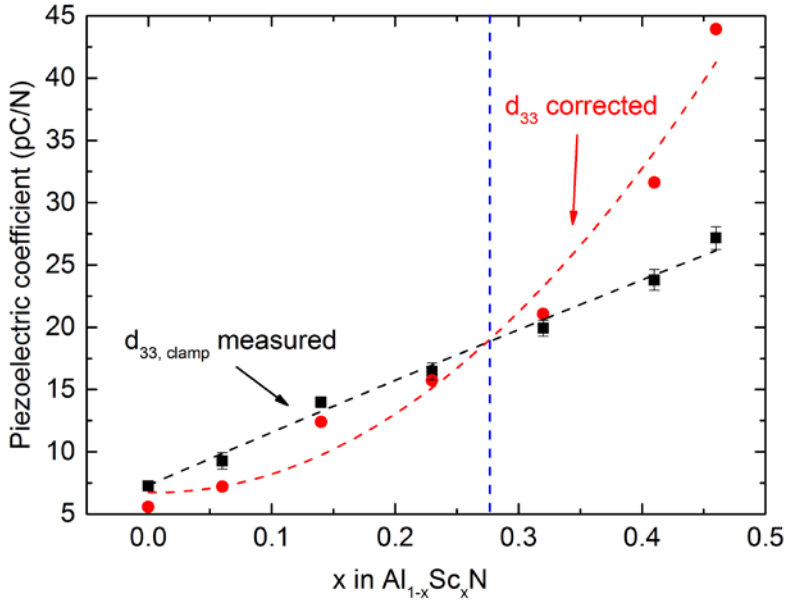

Figure 5-14 Piezoelectric coefficient d_{33} (clamped d_{33} as measured value, marked as red circles and corrected d_{33}, marked as black squares) as a function of Sc concentration x in $Al_{1-x}Sc_xN$, the lines are the guide for the eye. [147]

The calculated d_{33} is also plotted as a function of Sc concentration in Figure 5-14. Compared to the $d_{33,\,clamp}$, the d_{33} value for AlN is 5.5 pC/N and it is fitting to the theoretical value [53]. According to the trend and the guide line, the corrected values intersect the measured values at around x = 0.27, and corrected value experience a strong increase when x > 0.4. The achieved d_{33} after the correction for the $Al_{0.54}Sc_{0.46}N$ is 44 pC/N.

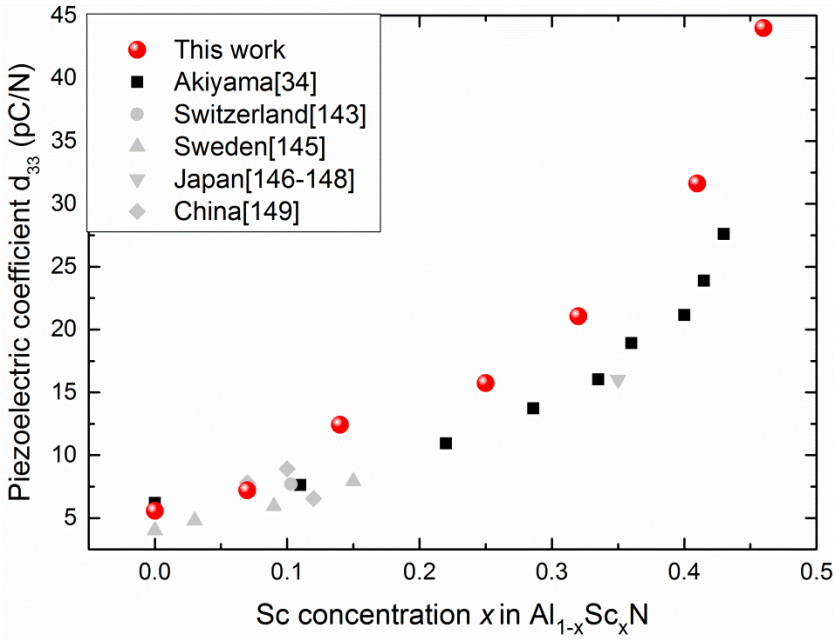

Figure 5-15 Piezoelectric coefficient d_{33} as a function of Sc concentration and comparison to the literature values, including the data from Switzerland [148], Sweden [149], Japan [3,150], China [151–153], Germany [103], Austria [154].

In Figure 5-15 the piezoelectric coefficient measured in this work is compared with part of the experimental value in the literature. Concerning the Sc concentration, the AlScN in this work is the with highest Sc concentration among the reported in the literature, and still with c-axis crystallographic orientation. Furthermore, the piezoelectric coefficient are much higher than the AlScN synthesized by

other research groups around the world. However, it is not explained whether the similar corrections is made in the literature values. The comparison of the absolute piezoelectric coefficient should be down by verifying the experimental and calculation methods mentioned in the literature. Therefore the AlScN/Si with high Sc concentration synthesized in this work already reach the standard of state-of-the-art, and the optimization of the sputtering parameter has proven as an effective approach.

5.3 AlScN on Al_2O_3 (0001) substrates

The $Al_{1-x}Sc_xN$ grown on the Si(001) showed the columnar growth from the cross-section SEM image. However, due to the large in-plane lattice mismatch, $Al_{1-x}Sc_xN$ and Si(001) will not have epitaxial relationship. Literatures reported that the sputtered AlN on Al_2O_3 shows epitaxial relationship and relatively high crystalline quality [89]. Furthermore, the electro-acoustic devices based on Al_2O_3 also shows better performance and unique properties because of the improved crystalline quality of AlN and high hardness of the Al_2O_3 substrate [60]. Therefore the $Al_{1-x}Sc_xN$ with Sc concentration variation x up to 0.46 is thus grown on the Al_2O_3(0001) substrates and their properties are evaluated.

Table 5-4 Overview of the sputtering parameter of the AlScN/Al_2O_3

Parameter	Value
$P_{Al} + P_{Sc}$	1000 W
Process pressure	9.5×10^{-4} mbar
Target-to-substrate distance	65 mm
$N_2 / (Ar + N_2)$	100%
Heater temperature	300-400 °C
Thin film thickness	1000 nm

The sputtering parameters are shown in Table 5-4. The partial power variation to achieve the specific Sc concentration in the $Al_{1-x}Sc_xN$ is the same as $Al_{1-x}Sc_xN$/Si mentioned in Figure 5-9. Here the heater temperature needs to be noticed. Because of the risk of the cracks to sputter on the Al_2O_3(0001) substrate, the heater temperature is tuned. As the plotted figure of the intrinsic stress measured by laser profiler for $Al_{1-x}Sc_xN/Al_2O_3$ in Figure 5-16, a higher tensile stress for the $Al_{1-x}Sc_xN/Al_2O_3$ with corresponding Sc concentration is observed to have 250-500 MPa higher than $Al_{1-x}Sc_xN$/Si, which could be the reason of the risk of the cracks for $Al_{1-x}Sc_xN/Al_2O_3$. When the Sc concentration is increasing, the AlN/Al_2O_3 and $Al_{0.54}Sc_{0.46}N/Al_2O_3$ showed 1074 MPa and -670 MPa, respectively. The differences of these two Sc concentrations are larger than that on the Si, which showed 545 and -1016 MPa, respectively. Both the stress in $Al_{1-x}Sc_xN$/Si and $Al_{1-x}Sc_xN/Al_2O_3$ is decreasing with the increasing Sc concentration, which is caused by introduction of more Sc atoms and thus the lager lattice parameter. The stress, could come from the microstructure, crystalline quality (will be shown later), lattice mismatch, thermal strain (especially here the heater temperature for the sputtering is different) and so on, which is so difficult to argue the dominating effect here.

Considering also the effect of the phase separation of the high Sc concentration in the AlScN/Si system, as well as the high tensile stress of $Al_{1-x}Sc_xN/Al_2O_3$, the actual heater temperature is set as 400°C (Sc concentration x = 0, 6, 14, 23, 32) and 300°C (Sc concentration x = 0.41 and 0.46)

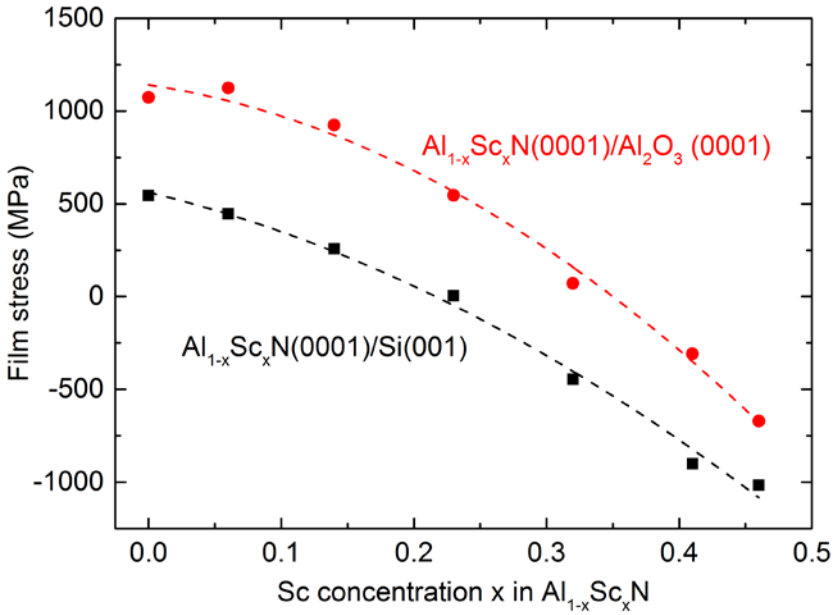

Figure 5-16 Intrinsic stress of $Al_{1-x}Sc_xN/Al_2O_3$ as a function of Sc concentration compared to $Al_{1-x}Sc_xN$/Si, the lines are guides for the eye. [147]

XRD $2\theta/\theta$ scans of the $Al_{1-x}Sc_xN/Al_2O_3$ are shown in the Figure 5-17. Only AlScN 000*l* (*l* = 2, 4) reflections and Al_2O_3 000*l* (*l* = 6, 9) in the measured range of the 2θ can be seen. No extra reflection indicates that all thin films of $AlScN/Al_2O_3$ are c-axis oriented, including the AlScN with Sc concentration over x = 0.4. The peak position of the $Al_{1-x}Sc_xN$ 0002 and Al_2O_3 0006 are at around 2θ = 36° and 42°, respectively, similar to the value reported in the literature [104,155]. However, there is not a clear trend of the peak shift for the $Al_{1-x}Sc_xN$ 0002 with respect to the Sc concentration, e.g. The 2θ = 36.11°, 35.99° and 36.19° are for AlN, $Al_{0.87}Sc_{0.13}N$ and $Al_{0.54}Sc_{0.46}N$, respectively. The peak shift in a non-linear behavior is similar to the $Al_{1-x}Sc_xN/Si$, that the non-linear evolution of c-lattice parameter is the reason. Also the relationship of the peak position and the c-lattice parameter is not straightforward, due to the effect of the thermal strain, lattice strain and other effects during the sputtering.

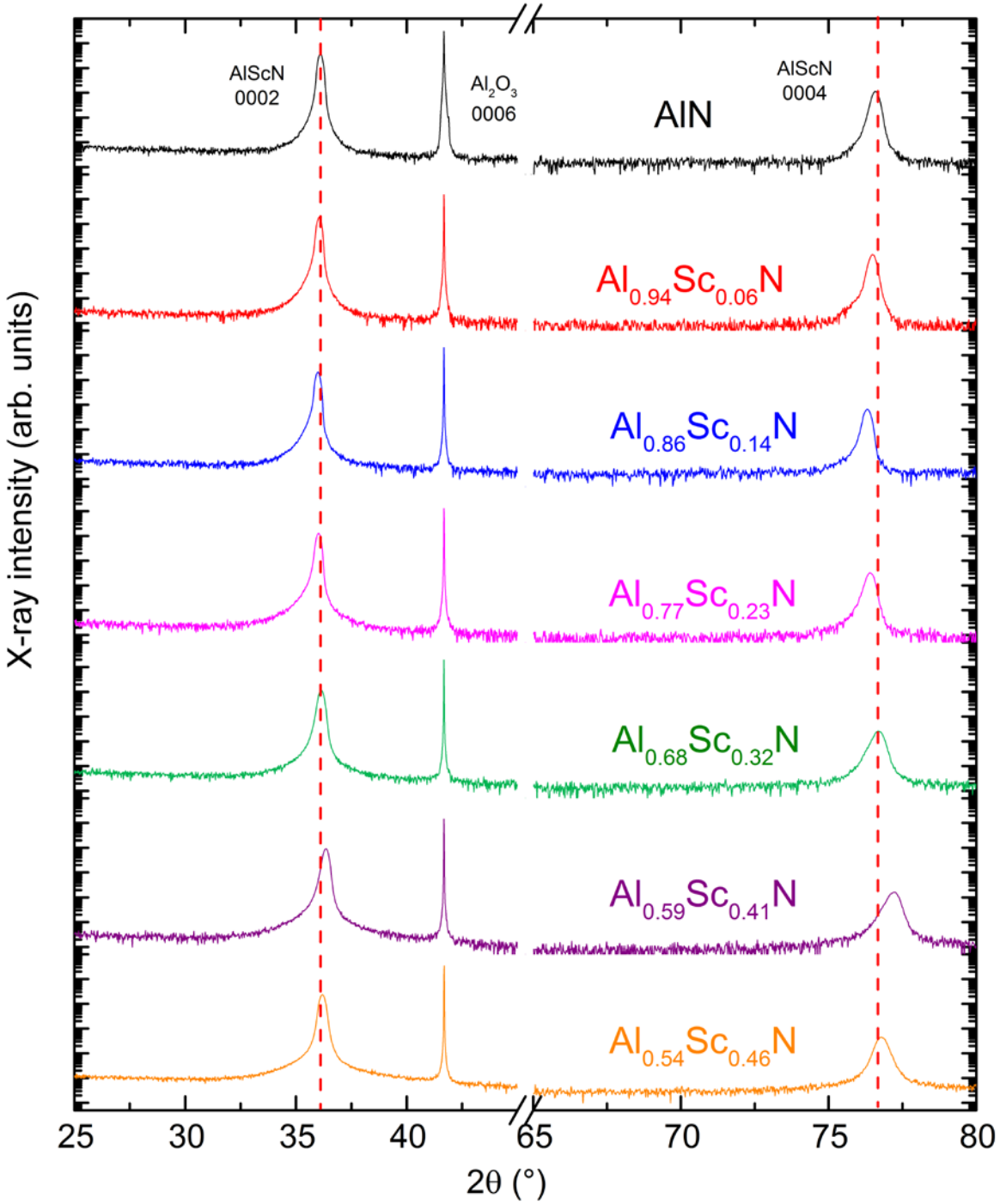

Figure 5-17 XRD 2θ/θ scans for the $Al_{1-x}Sc_xN/Al_2O_3$ up to x = 0.46, measurements was at the center on the wafer from AlScN 0002 reflections to AlScN 0004 reflections.

Texture analysis (XRD pole figure measurements) was done at wurtzite-type AlN $10\bar{1}1$ reflection position (Figure 5-18 (a) and (b)). For all $Al_{1-x}Sc_xN$/Si samples, a closed ring is seen at the polar angle $\psi = 62°$ which indicates fiber textured material with no preferential orientation in-plane [36,57] and for $Al_{1-x}Sc_xN/Al_2O_3$ the 6-fold symmetry was observed with the rotation of 30° between the substrate and the film, typical for epitaxial growth of group-III nitrides on Al_2O_3 substrates [89,156] where the epitaxial relationship can be defined $[10\bar{1}0]_{AlScN}//[11\bar{2}0]_{sapphire}$ and $(0001)_{AlScN}//(0001)_{sapphire}$.

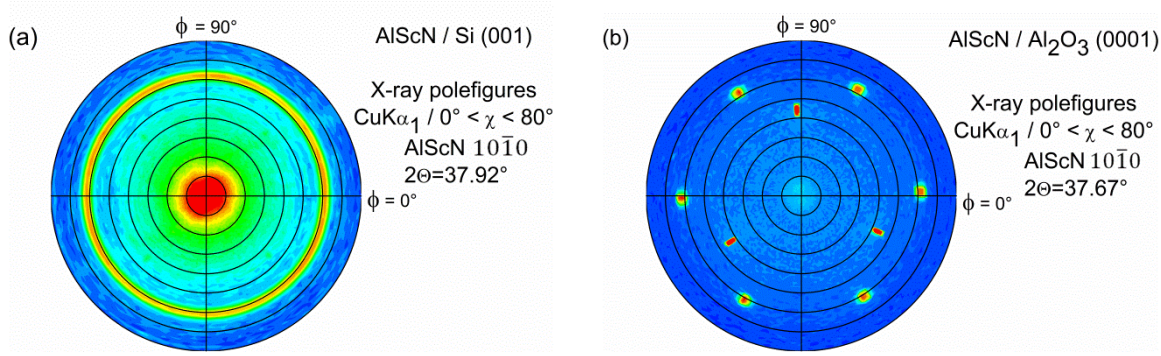

Figure 5-18 XRD pole figures for $Al_{0.68}Sc_{0.32}N$ sputtered on (a)Si (001) (b)Al_2O_3 (0001). [147]

The rocking curve FWHM of $Al_{1-x}Sc_xN$ 0002 are shown in Figure 5-19. The AlN/Al_2O_3 shows low FWHM of 0.7°, which indicates a very good crystalline quality. As the Sc concentration is increasing, the value goes up to 1.66° in the $Al_{0.54}Sc_{0.46}N$. Compared to the value of $Al_{1-x}Sc_xN/Si$, the $Al_{1-x}Sc_xN/Al_2O_3$ thin films have generally lower FWHM, which stands for a better crystalline quality when the $Al_{1-x}Sc_xN$ is sputtered on the Al_2O_3 instead of Si. However, the evolution trend shows different behavior of these two substrates.

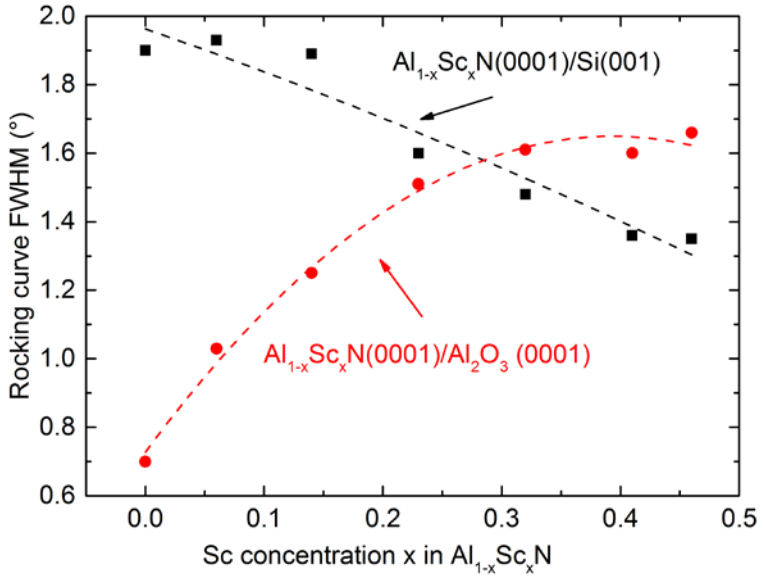

Figure 5-19 Rocking curve FWHM of AlScN 0002 as a function of x in $Al_{1-x}Sc_xN$ thin film sputtered on Si (001) (black square) substrate and Al_2O_3 (0001) (red circle), the lines are guides for the eye. [147]

As mentioned previously that the value goes down for the Si samples, but it goes up with the increasing Sc concentration for the Al_2O_3 samples. This is possibly due to the fiber texture of the $Al_{1-x}Sc_xN/Si$ and epitaxial growth of the $Al_{1-x}Sc_xN/Al_2O_3$. When the incorporated Sc concentration is increasing, the expected lattice parameter is also increasing due to the larger atomic size of the Sc. In the case of $Al_{1-x}Sc_xN/Si$, there is no in-plane alignment due to the confirmed fiber texture by the pole figure, the relaxation could happen and it will reduce the intrinsic stress. However, in the case of the $Al_{1-x}Sc_xN/Al_2O_3$, due to the epitaxial relationship confirmed by the 6-fold symmetric pole figure, there is no possibility of the relaxation when the Sc concentration is going up. Therefore the higher overall tensile stress and more sensible evolution trend with respect to the Sc concentration are observed.

5.4 Discussion and summary

In this chapter, the procedure of optimizing $Al_{1-x}Sc_xN$ sputtering in a large Sc concentration range on both Si(001) and Al_2O_3(0001) were discussed.

First the nitrogen ratio (N_2 / (Ar + N_2)) for thin film $Al_{1-x}Sc_xN$ sputtering is investigated for the study of misoriented grains. Randomly oriented AlN or $Al_{1-x}Sc_xN$ grains are not detected in XRD $2\theta/\theta$ scans when they are in a low density due to the small volume compared to substrate. Mapping of the piezo-domains in PFM reveal that those grains is possibly without piezoelectricity, therefore they are influencing the macroscopic piezoelectric performance of the $Al_{1-x}Sc_xN$ layer when the density of the misoriented grains is high. The density of the misoriented grains will decrease when: 1) the N_2 concentration is increasing, 2) the TSD is decreasing; and the N_2 concentration is more important for the density of the misoriented grains. Using 100% N_2 concentration could eliminate the existence of the misoriented grains. Regarding films without misoriented grains, the surface roughness R_{rms} of the $Al_{1-x}Sc_xN$ is as low as 1.5 nm. The non-existence of the misoriented grains can be double-checked with GIXRD, in this configuration the X-ray path into the $Al_{1-x}Sc_xN$ is much increased, thus the sensitivity for the surface microstructure and crystallographic orientation, the only drawback is the long measuring time. However, for the preliminary check of the thin film quality considering misoriented grains, SEM cross-section and planar images are sufficient.

After the effects of misoriented grains were reduced or eliminated in the $Al_{1-x}Sc_xN$ thin films, the Sc concentration was increased with tuning partial power of the Al and Sc (P_{Al} and P_{Sc}). Sc concentration was determined by EDX, based on reference SIMS samples. To solve the phase-instability of the $Al_{1-x}Sc_xN$ in higher Sc concentration ($x > 0.4$ in $Al_{1-x}Sc_xN$), the heater temperature was decreased at 400°C to maintain the wurtzite structure of the $Al_{1-x}Sc_xN$, while the films with lower Sc concentration were sputtered still at 500°C to achieve high crystalline quality. In this work the $Al_{1-x}Sc_xN$ with Sc concentration up to $x = 0.46$ is successfully synthesized, it is by far the $Al_{1-x}Sc_xN$ with highest Sc concentration with hexagonal wurtzite c-axis orientation. The piezoelectric coefficient d_{33} reached 44 pC/N, the highest value already exceed the literature value 27.6 pC/N achieved by Akiyama *et al.* in 2009. Furthermore, $Al_{1-x}Sc_xN$ with Sc concentration variation was also grown on the Al_2O_3(0001) substrates, and the heater temperature has been optimized to reduce the risk of macro cracks of AlScN. The $Al_{1-x}Sc_xN/Al_2O_3$ has higher crystalline quality regarding the corresponding Sc concentration on the Si(001), also from the pole figure, the $Al_{1-x}Sc_xN/Al_2O_3$ layers were grown epitaxially, with epitaxial relationship defined as $[10\bar{1}0]_{AlScN}//[11\bar{2}0]_{sapphire}$ and $(0001)_{AlScN}//(0001)_{sapphire}$. The epitaxial $Al_{1-x}Sc_xN/Al_2O_3$ reached better quality and unique properties of $Al_{1-x}Sc_xN$ enable more potential applications for $Al_{1-x}Sc_xN$.

In this chapter, the XRD $2\theta/\theta$ scans of $Al_{1-x}Sc_xN/Si$ and $Al_{1-x}Sc_xN/Al_2O_3$ were showing the same trend, that 2θ angle of AlScN 0002 and 0004 reflections first decreased and increased as a function of Sc concentration. The c-lattice parameters reported in the literature [52] is indicating similar non-linear trend, that is supporting the trend of peak shift of XRD in this work.

6 Mechanical and optical properties of AlScN

The hexagonal c-axis oriented $Al_{1-x}Sc_xN$ thin films up to x = 0.46 were synthesized on Si(001) and Al_2O_3(0001). In this chapter, the mechanical and optical properties of the $Al_{1-x}Sc_xN$ are investigated. First, the elastic modulus and the coefficient of thermal expansion will be determined by thermal cycling method. These two material parameters are evolving with Sc concentration and are very important regarding the design and fabrication of the electro-acoustic devices, and the device performance, thermal stability and long-term stability will be strongly influenced. This work was published and became the first systematic experimental study of the coefficient of thermal expansion of AlScN [147]. Secondly, the Raman spectroscopy is used to determine the Sc concentration dependent phonon vibration modes. It is the first time to observe the E_2(high) modes in samples with high Sc concentration due to the high crystalline quality of the $Al_{1-x}Sc_xN/Al_2O_3$. At last the spectroscopic ellipsometry is used to determine the refractive index and band gap of the $Al_{1-x}Sc_xN$.

6.1 Elastic modulus and coefficient of thermal expansion

For MEMS device design the mechanical properties, such as elastic modulus, and coefficient of the thermal expansion (CTE) are important parameters [157]. However, there are only few works which experimentally assess the elastic properties of this novel material and there is only one report on the elastic modulus of $Al_{1-x}Sc_xN$ with relatively high Sc concentration [53]. Moreover, to the best of my knowledge, the CTE of $Al_{1-x}Sc_xN$ thin films has not been reported until now and in addition to providing support for device design it is also a significant parameter for the accurate determination of the pyroelectric coefficient of $Al_{1-x}Sc_xN$ [158].

As reported in the literature, elastic modulus of $Al_{1-x}Sc_xN$ thin films can be locally measured by nanoindentation [6,157]. However, the indentation modulus can be influenced by the indentation depth, the substrate, and other factors [159]. Measuring the temperature-stress relationship of thin films grown on substrates with different CTE is a non-destructive method that not only enables the determination of the elastic modulus, but the CTE as well, as it was previously reported for AlN [36] and other materials [160,161]. The temperature-induced stress σ_T can be described by the following equations [162]:

$$\sigma_T = \frac{E_f}{(1-\nu_f)} \int_{T_2}^{T_1} (\alpha_s - \alpha_f) dT, \qquad 6\text{-}1$$

where $E_f/(1-\nu_f)$ is the biaxial elastic modulus and E_f and ν_f are Young's modulus and Poisson ratio of the film, respectively. α_s and α_f stand for the CTE of the substrate and the film, respectively. The CTE of the film α_f can also be described by:

$$\alpha_f = \frac{\alpha_{s1} - k\alpha_{s2}}{1-k}, \qquad 6\text{-}2$$

here $k = (\Delta\sigma_{s1}/\Delta T)/(\Delta\sigma_{s2}/\Delta T)$ is a ratio of stress-temperature slopes, which are calculated based on temperature-induced stress as a function of temperature on substrates "s1" with CTE α_{s1} and "s2" with CTE α_{s2}.

The CTE and biaxial elastic modulus of $Al_{1-x}Sc_xN$ are extracted based on Equation 6-1 and 6-2 by analyzing thin films deposited on Ø=100 mm Si(001) and Al_2O_3(0001) substrates. The sputtering parameters and the crystalline quality were already descripted in the Chapter 4. To determine the film stress in as-deposited $Al_{1-x}Sc_xN$, first the film thickness was measured by ellipsometry (SENTECH SE800), the wafer curvature before and after the sputtering was measured by FSM 500TC laser profiler, and then the in-plane stress σ was calculated by using Stoney-equation [163]:

$$\sigma = \frac{E_s d_s^2}{6(1-\nu_s)d_f}\left(\frac{1}{R} - \frac{1}{R_0}\right), \qquad 6\text{-}3$$

here the $E_s/(1-\nu_s)$ is biaxial elastic modulus of the substrate and d_f and d_s are the thicknesses of the film and substrate, respectively. R_0 and R stand for the radius of curvature before and after the film deposition. In order to determine the CTE and the biaxial elastic modulus of $Al_{1-x}Sc_xN$, the temperature-induced stress was measured under N_2 atmosphere, in the same laser profiler experimental set-up. First, thermal cycling for $Al_{1-x}Sc_xN$/Si and $Al_{1-x}Sc_xN/Al_2O_3$ samples was done between room temperature and 400°C with heating and cooling rate of 2 K/min, where every 25 K the temperature was held constant for 5 min before the wafer curvature measurement was performed. However, $Al_{1-x}Sc_xN/Al_2O_3$ samples with x = 0.06 and 0.14 were prone to cracking at elevated temperatures and thus the maximum temperature in the thermal cycling experiments was reduced to 125 °C with 2 K/min heating and cooling rate and the wafer curvature was recorded every 10 K for improved accuracy.

6.1.1 Elastic modulus and CTE as a function of Sc concentration

Additional thermal cycling experiments under the same conditions were also performed for $Al_{1-x}Sc_xN$/Si samples and the stress-temperature slopes did not show any significant difference from the original thermal cycling series up to 400 °C, thus the original measurement data was used. To investigate the possible film quality degradation or structural changes before and after the thermal cycling, FWHM of $Al_{1-x}Sc_xN$ 0002 reflection rocking curve were compared and showed ±0.1° difference for all investigated samples; sample composition recorded in EDX varied only within the measurement error; surface roughness R_{rms} <1.5 nm was measured by AFM both before and after the thermal cycling, indicating that the samples did not undergo any irreversible changes in their microstructural or crystalline properties.

For calculation of the $Al_{1-x}Sc_xN$ CTE and biaxial elastic modulus, CTE was assumed to be constant in the temperature range 25-400°C, and the following literature values were used for Si(001): biaxial elastic modulus $E_s/(1-\nu_s)$ = 180 GPa [164], CTE α = 3.57×10^{-6} K^{-1} [34] and for Al_2O_3(0001) [165]: biaxial elastic modulus $E_s/(1-\nu_s)$ = 472.6 GPa, CTE α = 5.23 ×10^{-6} K^{-1}.

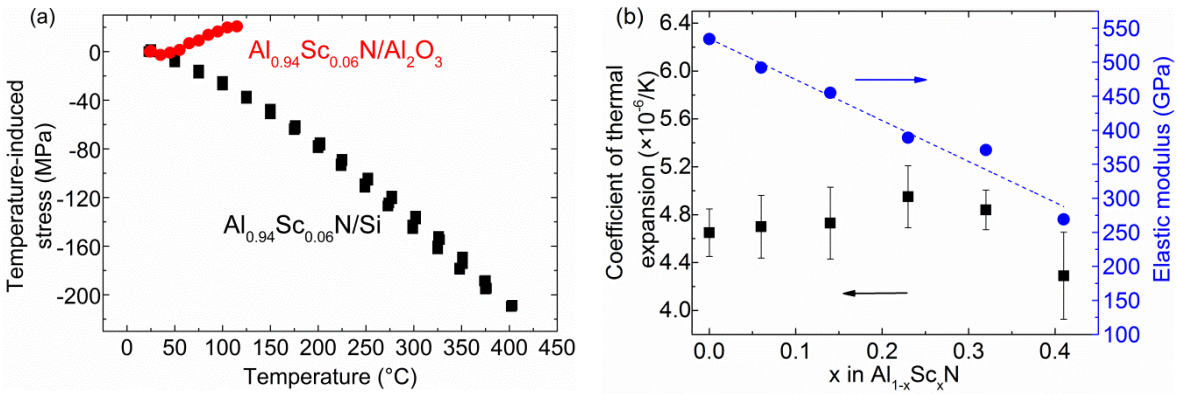

Figure 6-1 (a) Temperature-induced stress as a function of temperature in $Al_{0.94}Sc_{0.06}N$ grown on Si(001) (black squares) and on Al_2O_3 (0001) (red circles); (b) Biaxial elastic modulus (blue circles) and average coefficient of thermal expansion (black squares) as a function of Sc concentration in $Al_{1-x}Sc_xN$, lines are a guide for the eye. [147]

Due to the different substrate CTE the $Al_{1-x}Sc_xN$/Si films become more compressive stressed and the $Al_{1-x}Sc_xN/Al_2O_3$ more tensile, as an example the temperature-induced stress curves recorded for $Al_{0.94}Sc_{0.06}N$ are shown in Figure 6-1 (a). Using Equation 6-1 and 6-2 the average CTE and biaxial elastic modulus were calculated and the results are shown in Figure 6-1 (b), here the error originates from scattering of the data when fitting the stress-temperature slope and increases with the Sc concentration. CTE of AlN was determined to be $\alpha = 4.65 \pm 0.20 \times 10^{-6}$ K^{-1} (black squares) while values in the literature range from 2.56 to 5.27 $\times 10^{-6}$ K^{-1} [158,166,167] and biaxial elastic modulus of 535 GPa (blue circles) while 450-489 GPa has been reported previously [36,53]. With increasing Sc concentration the CTE of $Al_{1-x}Sc_xN$ is first increasing and reaches the highest value of $\alpha = 4.95 \pm 0.26 \times 10^{-6}$ K^{-1} at $x = 0.23$ and then decreases down to $a = 4.29 \pm 0.36 \times 10^{-6}$ K^{-1} for $x = 0.41$. The biaxial elastic modulus of $Al_{1-x}Sc_xN$ as a function of Sc decreases linearly by $E_f / (1 - \nu_f) = 534.77 - x \cdot 601.36$ The findings are in good agreement with theoretically predicted and experimentally determined biaxial elastic modulus by Caro *et al.* [53]. The non-linear behavior of CTE could be explained by the non-linear evolution of lattice parameter *c* [3,50,54] suggesting that the shape of the unit cell is changing non-linearly as a function of Sc concentration.

6.1.2 Temperature dependent CTE

In addition, temperature-dependent CTE of AlN and $Al_{0.68}Sc_{0.32}N$ were calculated by using temperature-dependent stress data (Figure 6-2 (a)) as well as temperature-dependent Si(001) and Al_2O_3(0001) CTE every 50°C [34,165]. The calculation of temperature-dependent CTE not only helps optimization of mechanical properties during film deposition but also the design of the temperature-compensated devices [168,169]. Figure 6-2 (b) shows the CTE of AlN (black squares) and $Al_{0.68}Sc_{0.32}N$ (blue triangles) as a function of temperature.

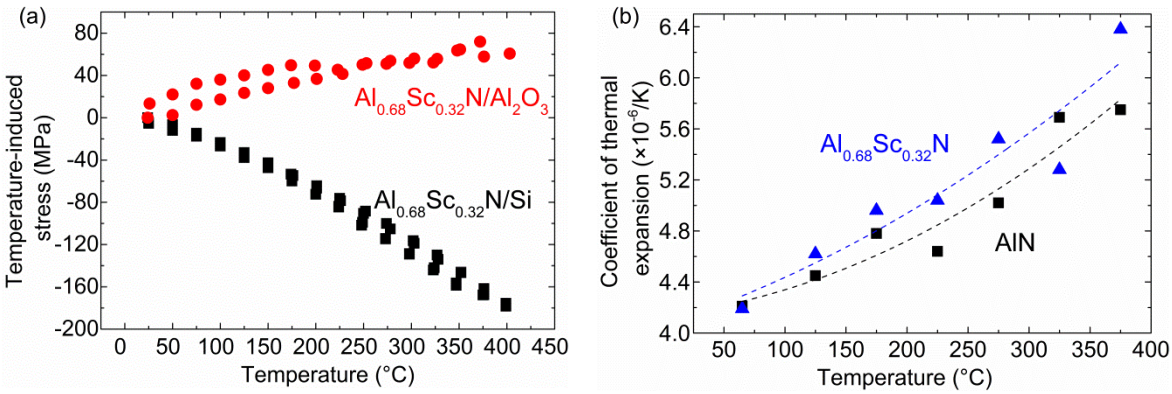

Figure 6-2 (a) Temperature-induced stress as a function of temperature in $Al_{0.68}Sc_{0.32}N$ grown on Si(001) (black squares) and on Al_2O_3 (0001) (red circles); (b) Temperature-dependent coefficient of thermal expansion of AlN (black squares) and $Al_{0.68}Sc_{0.32}N$ (blue triangles) as a function of temperature, lines are a guide for the eye. [147]

The CTE increases with temperature from 4.21 × 10^{-6} K^{-1} at 65°C to 5.75 × 10^{-6} K^{-1} at 400°C for AlN and from 4.18 × 10^{-6} K^{-1} at 65°C to 6.38 × 10^{-6} K^{-1} at 400 °C for $Al_{0.68}Sc_{0.32}N$. Similar trends in literature can be seen in previous studies of temperature-dependent CTE in AlN [34,35]. Summary of experimentally determined average CTE and elastic modulus as a function of Sc concentration, as well as calculated values based on literature are summarized in Table 6-1:

Table 6-1 Experimental CTE, elastic modulus, and theoretical elastic modulus of $Al_{1-x}Sc_xN$

Sc concentration x	CTE (×10^{-6} K^{-1})	Elastic modulus (GPa)	Elastic modulus in literature [53] (GPa)
0 (AlN)	4.65 ± 0.20	535	490
0.06	4.70 ± 0.26	492	452
0.14	4.73 ± 0.30	456	415
0.23	4.95 ± 0.26	389	367
0.32	4.84 ± 0.17	371	317
0.41	4.29 ± 0.36	270	261

6.1.3 Discussion

The CTE of $Al_{1-x}Sc_xN$ has a non-linear trend as a function of Sc concentration, although the elastic modulus is decreasing linearly. The atomic structure of $Al_{1-x}Sc_xN$ with different Sc concentration is shown in Figure 6-3. Two effects should be considered when more and more Al atoms are replaced by Sc atoms.

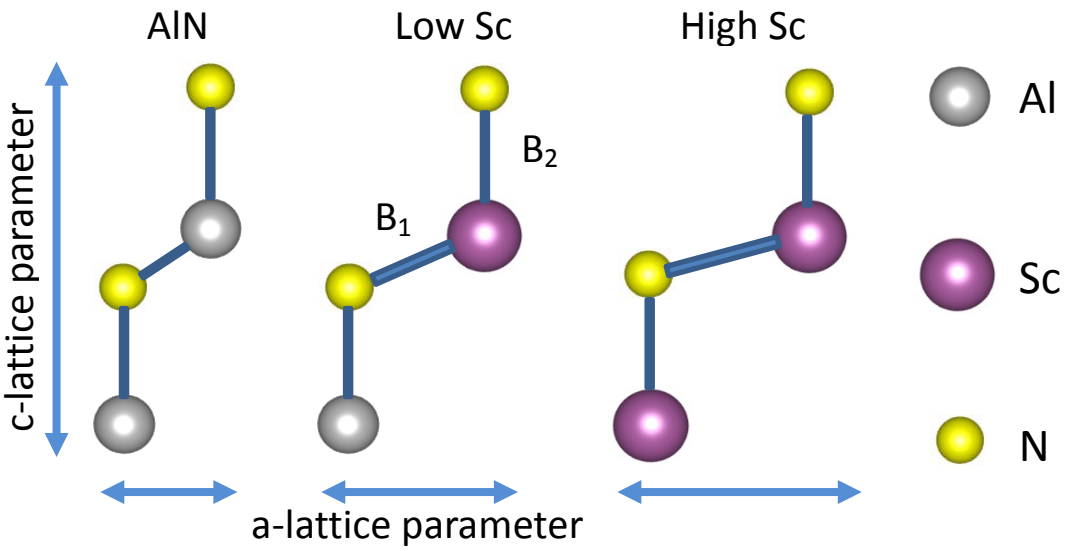

Figure 6-3 Atomic structure of AlN, AlScN (low Sc concentration) and AlScN (high Sc concentration), B_1 and B_2 stand for different Al(Sc)-N bond.

1. Bond length and strength: B_1 and B_2 are the Al(Sc)-N bonds. If considering a larger atom radius of Sc (230 pm) compared to Al (184 pm), replacing Al by Sc atoms leads to larger bond length of both B_1 and B_2. Therefore, the bond strength of B_1 and B_2 is generally weaker at high Sc concentration.
2. Bond angle of B_1: Considering the non-linear evolution of c-lattice parameter and increasing a-lattice parameter in the theoretical prediction [52], bond angle of B_1 is increasing. As a result, B_1 contributes more in the a-lattice parameter and less in the c-lattice parameter.

The non-linear of trend CTE change as a function of Sc concentration can be explained by combining these two effects. The CTE is calculated by thermal-induced biaxial stress, therefore it is affected by in-plane crystal lattice parameter. The competition is happening between weak bond strength and large bond angle, it finally results in non-linear behavior of CTE in a-direction. Similarly, CTE in c-direction is much weaker as Sc concentration is increased. The reason is reduced strength in both B_2 and B_1, and B_1 bond is affecting less in c-direction.

6.2 Phonon modes

Raman spectroscopy measures the phonon vibrational information, which can be used to determine the crystalline quality, the stress, compositional information and so on[32]. It was reported in the literature that the E_2(high) peak of the AlN is used to determine the stress of the AlN/Si wafer[106]. The first Raman spectroscopy measurement for $Al_{1-x}Sc_xN/Al_2O_3$ was reported by Deng *et al.* [109], the optical phonon modes E_2(High) and A_1(LO) is identified in the AlScN, however the results were only up to x = 0.16 due to the material quality and signal-to-noise ratio.

In this work 1 um thick $Al_{1-x}Sc_xN/Al_2O_3$ and $Al_{1-x}Sc_xN$/Si up to x = 0.41 were used for Raman. The measurement was done with Renishaw Invia Raman Microscope. The Si calibration sample was used before measurement, to correct the peak shift and peak intensity. The measurement points were in the

center of the 100 mm $Al_{1-x}Sc_xN/Al_2O_3$ wafer using 5% of the laser power and 200 accumulations. First, the stress mapping of AlN/Si will be introduced, to determine the average stress of the 100 mm wafer and also to map the localized stress of AlN/Si and AlN/Al_2O_3 in macroscopic range. Secondly, the Raman mode of $Al_{1-x}Sc_xN$ $/Al_2O_3$ in higher Sc concentration is recorded, due to the high crystalline quality it is the first time to observe the phonon modes in Sc concentration x > 0.2.

6.2.1 Stress determination of AlN

In the normal procedure of stress determination, the thickness of the wafer is characterized by spectroscopic ellipsometry using Cauchy-equation with Urbach tail. Afterwards, the average wafer curvature of 100 mm wafer could be calculated by the Stoney equation[163]. However, the stress determined by wafer curvature is could not describe the local stress, especially to analyzed the relaxed area with macro cracks, e.g. If the cracks could be observed on the surface of the AlN/Al_2O_3 in the micro- and macro range from SEM or optical microscopy, the tensile stress measured by laser-profiler is already the stress value after the relaxation. In order to evaluate the local stress in the AlN/Al_2O_3, Raman spectroscopy is used for the determination. Based on characterization methods described by [106,170], AlN E_2 peak position in the Raman spectra as a function of average film stress is shown in Figure 6-4.

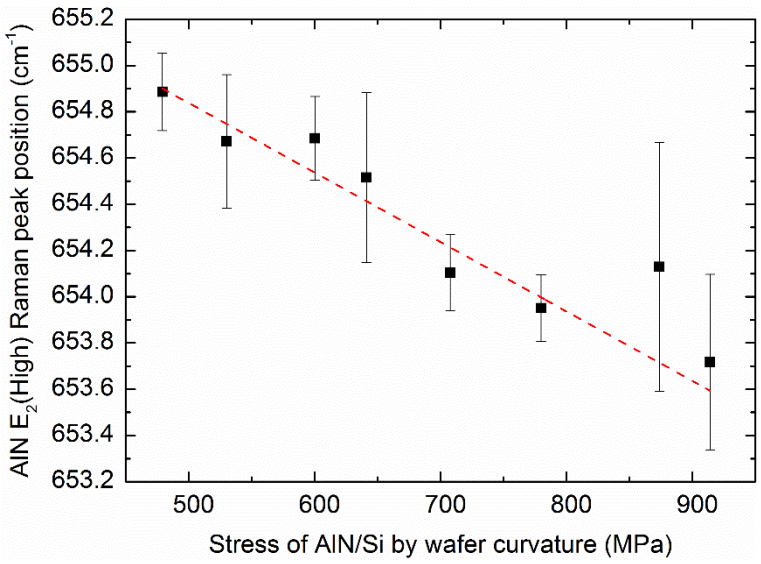

Figure 6-4 AlN/Si E_2(High) peak position as a function of intrinsic stress measured by laser profiler, the line is a guide for the eye.

In Figure 6-4 shows the reflection at peak position of the 653 cm^{-1} for AlN E_2 (high) phonon mode [32], the peak position of the E_2 (high) is dependent on the stress of the film, therefore a correlation is established to the stress measured by laser-profiler. It could be observed that E_2 (High) peak position is proportional to the stress measured and calculated by the wafer curvature. The calculated slope is 3.55 ± 0.55 GPa/cm^{-1}, close to the literature value 3.7 ± 0.3 GPa/cm^{-1}[170].

By doing mapping of the Raman spectra of the desired local area, the local stress of the AlN/Al_2O_3 thin film with cracks can be easily estimated (Figure 6-5). Although the stress from wafer curvature shows an average value of 400 MPa, in the stress mapping by the Raman spectra it is ranging from -125 MPa to 1360 MPa. The area with larger size between the cracks experience high tensile stress up to 1360 MPa in the center of the mapping, while the area with smaller size between the

cracks have the stress approaching to zero, likely relaxed. From this local stress mapping, the as-deposited AlN/Al_2O_3 determined by the laser profiler as slightly tensile-stressed is not reliable due to the relaxation of the cracks. The real stress could be higher than 1000 MPa and it causes crack after the sputtering.

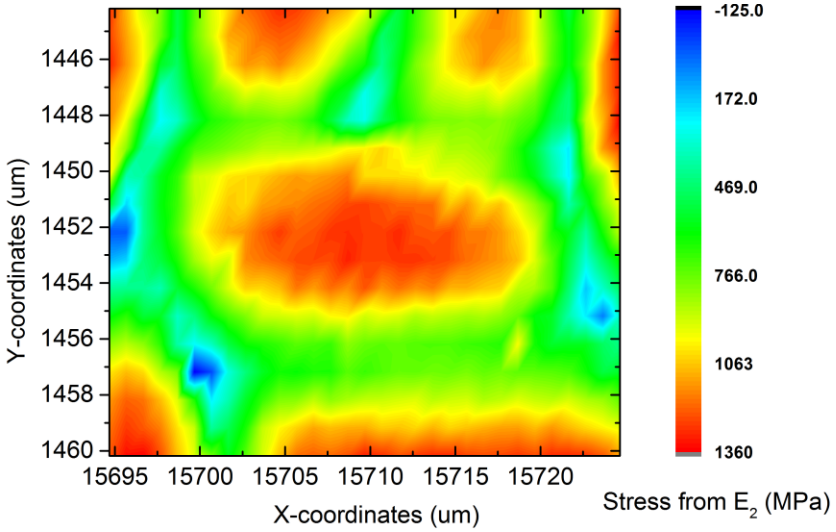

Figure 6-5 Stress mapping evaluated from the E_2(high) peak of the AlN/Al_2O_3 from Raman spectroscopy, sputtered under 500°C.

6.2.2 Phonon modes in the AlScN/Al_2O_3

The stress-E_2(High) peak position relations of AlN is already introduced. However, the reader may ask why it is applied only for AlN/Si instead of $Al_{1-x}Sc_xN$. When there is no Sc incorporated, the E_2(High) peak shift is mainly caused by the strain. However, when the Sc is incorporated, it is hard to determine whether the peak shift is from the stress or from the Sc concentration. Also, in this work the $Al_{1-x}Sc_xN$/Si had very low Raman intensity, and with Sc concentration x > 0.14 it is hard to distinguish it from the background noise. Therefore the $Al_{1-x}Sc_xN/Al_2O_3$ was investigated, and the Raman spectra with different Sc concentrations are listed in Figure 6-6.

As shown in Figure 6-6, the E_2(High), A_1(LO) and E_1(LO) are marked in the Raman spectra. First the E_2(High) has a peak shift to the lower wavenumbers: AlN shows E_2(High) at 651.06 cm^{-1} and it shifted to the 581.20 cm^{-1} in the $Al_{0.59}Sc_{0.41}N$. However the peak intensity in the $Al_{0.59}Sc_{0.41}N$ is much lower and the peak is much wider than that in the AlN, but it still can be recognized. The E_2(High) is shifted to the lower wavenumbers also due to the stress change, which was discussed in Chapter 5.3. However, if considering the stress in the stress-E_2(High) peak position relations of AlN having the trend 3.55 ± 0.55 GPa/cm^{-1}, the peak shift is not only caused by the stress in the $Al_{1-x}Sc_xN$ thin film, in that case the wavenumbers of $Al_{0.59}Sc_{0.41}N$ should be around the 645 cm^{-1}. Apparently, the measured E_2(High) has a much lower wavenumber and it is caused by the incorporation of the Sc. The width of the E_2(High) is increasing of the increasing Sc concentration, indicating more degraded crystalline quality in the higher Sc concentration.

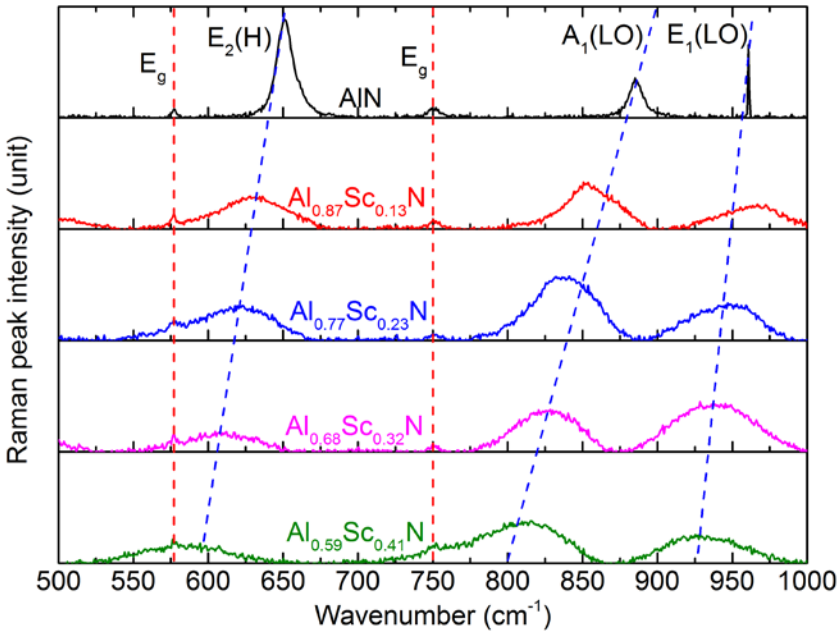

Figure 6-6 Raman scattering for AlScN/Al_2O_3 with x = 0-0.41. The red dash lines are indicating the E_g modes of Al_2O_3(0001) substrate, and the blue dash lines are indicating AlScN E_2(High), A_1(LO) and E_1(LO) modes.

The degraded crystalline quality in AlScN/Al_2O_3 is confirmed by the XRD rocking curve FWHM in the Chapter 5.3. Deng *et al.* reported a more than 14x wider E_2(High) peak as in the AlN, explained with a bond softening caused by substantially incorporation of Sc [109]. The A_1(LO) peak is shifting to the small wavenumber, as well. The A_1(LO) peak is at 885 cm^{-1} for AlN and 812 cm^{-1} for $Al_{0.59}Sc_{0.41}N$, which fits the 890 cm^{-1} for AlN in the literature [109]. It is reported that the A_1(LO) peak position is affected by the composition in the $Al_{1-x}Ga_xN$ [32]. The similar trend is also found in the $Al_{1-x}Sc_xN$ (Figure 6-7). The trend is similar to the linear behavior, the correlation of the wavelength of Raman A_1(LO) peak position $\omega_{A1(LO)}$ and Sc concentration x can be expressed as: $\omega_{A1(LO)} = 883 - 184x$. The trend of A_1(LO) is similar to the reported data [109].

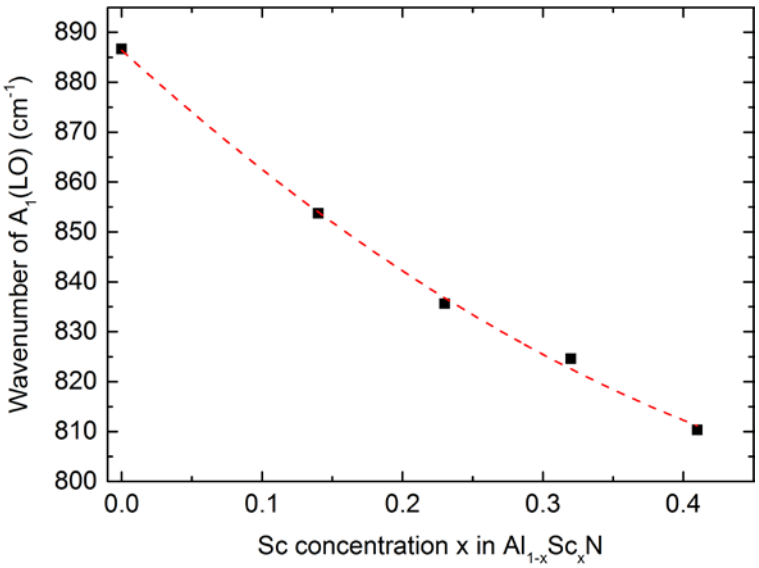

Figure 6-7 Wavenumber of the A_1(LO) peak in the Raman spectra of AlScN/Al_2O_3 as a function of the Sc concentration, the line is a guide for the eye.

6.2.3 Discussion

In this section, the Raman spectroscopy was used to determine the phonon modes A_1(LO) and E_2(High) in $Al_{1-x}Sc_xN/Al_2O_3$. The wavenumber of the both phonon modes were decreased to lower values as a function of Sc concentration, which is fitting the trend of reported values up to $Al_{0.85}Sc_{0.15}N$ [109].

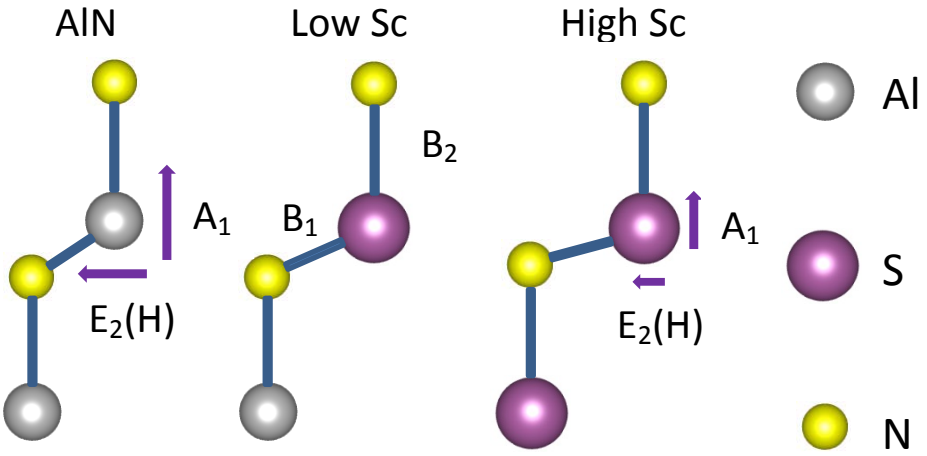

Figure 6-8 Atomic structure of AlN, AlScN (low Sc concentration) and AlScN (high Sc concentration), B_1 and B_2 stand for different Al(Sc)-N bond and arrows are showing A_1 and E_2(High) phonon modes

The schematic figure of the $Al_{1-x}Sc_xN$, similar to the one in Chapter 6.1.3, in Figure 6-3 is showing the vibrating of the A_1(LO) and E_2(High). The atomic mass of Sc than Al, 45 and 27 g/mol, respectively. The atomic mass of the metal atoms in the film m_{metal} is expressed as $m_{metal} = (1 - x)\, m_{Al} + m_{Sc}$, which is statistically increasing as a function of Sc concentration. The increased atomic mass leads to a vibration at lower frequency in both A_1(LO) and E_2(High), as measured in the Raman spectroscopy. However, because the A_1(TO) peak is missing in the Raman spectra, the covalent bond strength for $Al_{1-x}Sc_xN$ is not quantitatively determined.

6.3 Band gap of AlScN

Due to the band gap engineering for optoelectronics, there are quite a lot of works on III-metal-N compounds [171]. Zhang *et al.* [52] calculated the band gap of AlScN up to Sc concentration x = 0.5 when the structure is still wurtzite. Later on, Deng *et al.* determined the band gap up to Sc concentration x < 0.2. In this part, the spectroscopic ellipsometry measurements for $Al_{1-x}Sc_xN/Al_2O_3$ up to Sc concentration x = 0.41 will be described.

The epitaxial grown $Al_{1-x}Sc_xN/Al_2O_3$ up to x = 0.41 were measured by Woollam V.A.S.E. Furthermore, additional samples with Sc concentration x = 0.09 and 0.17 were fabricated to show better trend of the band gap evolution as function of Sc concentration. During the measurements, the incident angle is set at 65°, 70°, 75° and the detailed data are based on 65°. Optical constant of Cauchy-fitting with Urbach tail of Al_2O_3 is based on the result of Yao *et al.* [172]. In Figure 6-6, the reflection spectra of the $Al_{1-x}Sc_xN/Al_2O_3$ up to x = 0.41 is shown. The Fresnel fringes are observed in a lower energy range and the amplitude is decreasing with increasing energy and then disappears, which indicates a

strong absorption when the energy of the light is approaching the band gap. The absorption energy is decreasing with the increasing Sc concentration, it shows band gap energy E_g is 5.8 eV in the AlN and 4.4 eV in the $Al_{0.59}Sc_{0.41}N$. The E_g in the AlN is lower than the value in the literature, which is around 6.2 eV [52,171,173], and the E_g of $Al_{0.59}Sc_{0.41}N$ is higher than the measured value [171] and the theoretical prediction [52].

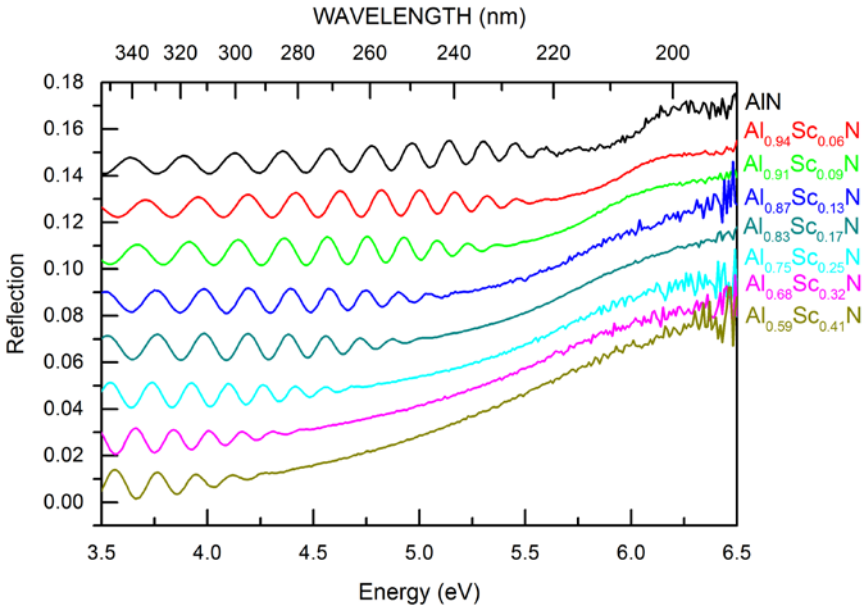

Figure 6-9 Reflection spectra from spectroscopic ellipsometry, from AlScN up to Sc concentration x = 0.41. [174]

Later, based on the spectroscopic ellipsometry spectra amplitude ratio Ψ(E) and phase difference Δ(E), as well as the reflection spectra, absorption coefficient and Tauc plot is extracted. These results are showing AlN with band gap around 6.2 eV, and $Al_{0.59}Sc_{0.41}N$ with band gap between 4.6-4.8 eV. Compared to the theoretical band gap from Zhang *et al.* [52], the experimental determined band gap is fitting to the calculated value very well, showing the good material quality of sputtered AlScN. The more detailed discussion of the accuracy as well as combination of other determination to analyze the band gap of AlScN is discussed in [174].

6.4 Summary

In this chapter, the characterization of the $Al_{1-x}Sc_xN$ mechanical and optical properties were described.

The elastic modulus and coefficient of thermal expansion coefficient were successfully determined by thermal cycling method and first reported in this work. Elastic modulus is decreasing as the increasing Sc concentration, from 535 GPa in AlN to 270 GPa in $Al_{0.59}Sc_{0.41}N$. Furthermore, the CTE of the $Al_{1-x}Sc_xN$ showed non-linear behavior regarding the increasing Sc concentration, which could be caused by anisotropic evolution of crystal dimensions. Temperature dependent CTE of $Al_{0.68}Sc_{0.32}N$ was determined and had similar increasing trend with temperature as reported value for AlN in the literature[35]. The measurement and analysis of these effects was possible because the high crystalline quality and highly c-axis oriented $Al_{1-x}Sc_xN$ achieved at Fraunhofer IAF. The elastic modulus and CTE will help the design of the electro-acoustic device in predicting device performance at the elevated temperatures.

Afterwards, the optical measurements such as Raman spectroscopy and spectroscopic ellipsometry were carried out. The peak shift of the E_2(High) and A_1(LO) are first observed in the higher Sc concentration, both are correlated to the Sc concentration and crystalline quality. In the Raman spectroscopy the correlation between AlN E_2(High) peak shift and stress was made, the established relationship was used to find the macrocracks in the optimization of the AlN/Al_2O_3 sputtering deposition. Thanks to the developed stress-management, the epitaxial $Al_{1-x}Sc_xN/Al_2O_3$ thin films as well as high Sc concentration were achieved.

In order to determine band gap with respect to the Sc concentration in the AlScN, spectroscopic ellipsometry measurement is done by analyzing $Al_{1-x}Sc_xN/Al_2O_3$ up to x = 0.41. However, determination based on the absorption of the reflectance spectra still have higher deviation regarding to the existing value in the theoretical prediction [52] and parts of the measurement [171]. Therefore the further AlScN/Al_2O_3 with transparent substrate are under preparation and more measurements are being organized. The plan is to precisely determine the band gap of the $Al_{1-x}Sc_xN$ to confirm the capability of band gap engineering by adjusting Sc concentration, which makes $Al_{1-x}Sc_xN$ a material with great potential for the optoelectronic applications.

7 AlScN based SAW resonators

In this chapter, surface acoustic wave (SAW) resonators were fabricated and characterized to determine the material properties and guides the further optimization of the sputtering deposition. $Al_{1-x}Sc_xN$ film in the SAW serves as piezoelectric material, therefore the properties of the SAW resonators, such as resonance frequency, electro-mechanical coupling coefficient are also the important parameters to describe the material. The highest resonance frequency achieved by the SAW is around 2 GHz with the smallest wavelength of 2 um, which proves the application of $Al_{1-x}Sc_xN$ in the frequency range of the 5G telecommunications.

The $Al_{1-x}Sc_xN$ thin films were deposited on the 100 mm diameter Si (001) substrates with the resistivity 3000-10000 Ohm·cm, different from the common Si (001) in the previous material development with resistivity 1-5 Ohm·cm. Clement et al.[175] reported that the distorted response and low in-band insertion loss in the AlN-based SAW structure sputtered on conductive Si (001) substrates. Therefore the $Al_{1-x}Sc_xN$ thin films up to Sc concentration x = 0.32 on high-resistivity Si (001) are sputtered under the following parameters:

Table 7-1 Sputtering parameter of the AlScN/High-resistivity Si(001)

Parameter	Value
$P_{Al} + P_{Sc}$	1000 W
Process pressure	9.5×10^{-4} mbar
Target-to-substrate distance	65 mm
$N_2 / (Ar + N_2)$	100%
Heater temperature	400-500 °C
Thin film thickness	1000 nm

The sputtering parameters listed in Table 7-1 are similar to the parameters in Chapter 5. The P_{Al} and P_{Sc} were set to 1000/0, 800/200 and 625/325 to achieve the Sc concentration x = 0, 0.14 and 0.32. The heater temperature is 400°C and 500°C for x = 0 and 0.14, respectively, to control the wafer curvature. Other details such as pre-sputtering, TSD and process pressure are same as the recipe in Chapter 5.

The crystallographic orientation and crystalline quality are determined by XRD $2\theta/\theta$ scan and ω-scan, which is shown in Figure 7-1. First, all the $Al_{1-x}Sc_xN$ thin films showed $000l$ (l = 2, 4) in the $2\theta/\theta$ scan, no extra reflections, indicating the c-axis orientation in the $Al_{1-x}Sc_xN$ thin film. Compared to the samples in Chapter 5.2 the preferred orientation didn't change under the different resistivity of the Si substrate. The peak shift towards lower 2θ was observed with increasing Sc concentration, which is caused

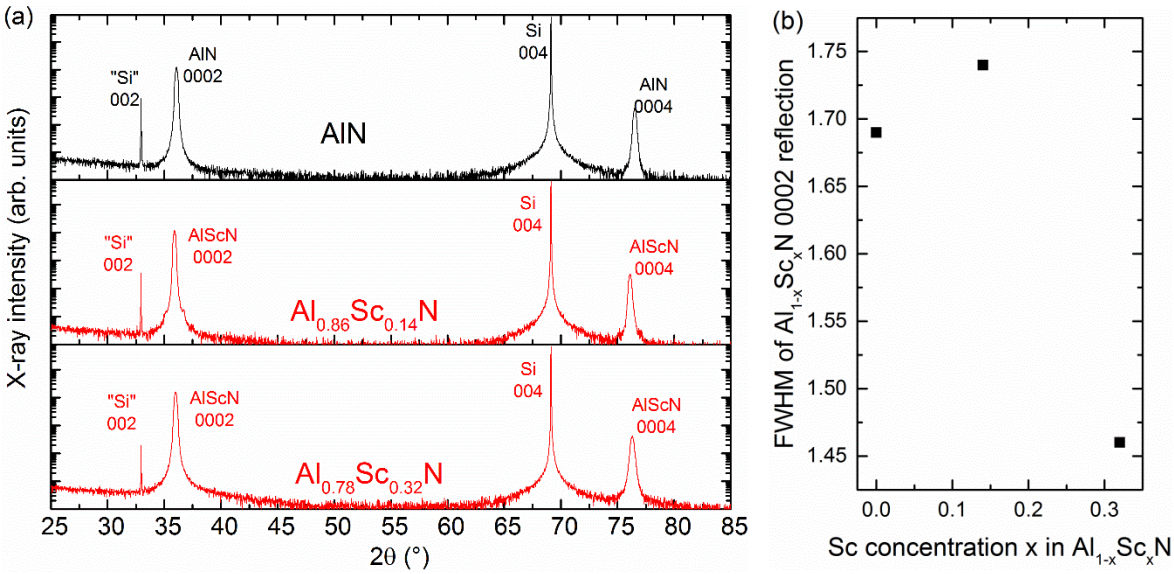

Figure 7-1 (a) XRD 2θ/θ scan of the AlScN/High-resistivity Si substrate (b) rocking curve FWHM of AlScN 0002 as a function of Sc concentration

by the lattice strain due to Sc incorporation. The FWHM of $Al_{1-x}Sc_xN$/High-resistivity Si 0002 rocking curve was characterized by XRD ω-scan, FWHM increases to 1.74° in the $Al_{0.86}Sc_{0.14}N$ from 1.69° in the AlN, and with further decrease to 1.47° in $Al_{0.68}Sc_{0.32}N$. The similar trend when the $Al_{1-x}Sc_xN$ in deposited on lower resistivity substrates in the chapter 5.4 was shown, that in the low Sc concentration ranging from x = 0 to 0.14 the FWHM is only fluctuating in ± 0.5°, and it decreases drastically when the Sc concentration is larger than x = 0.23, indicating the better crystalline quality in the higher Sc concentration.

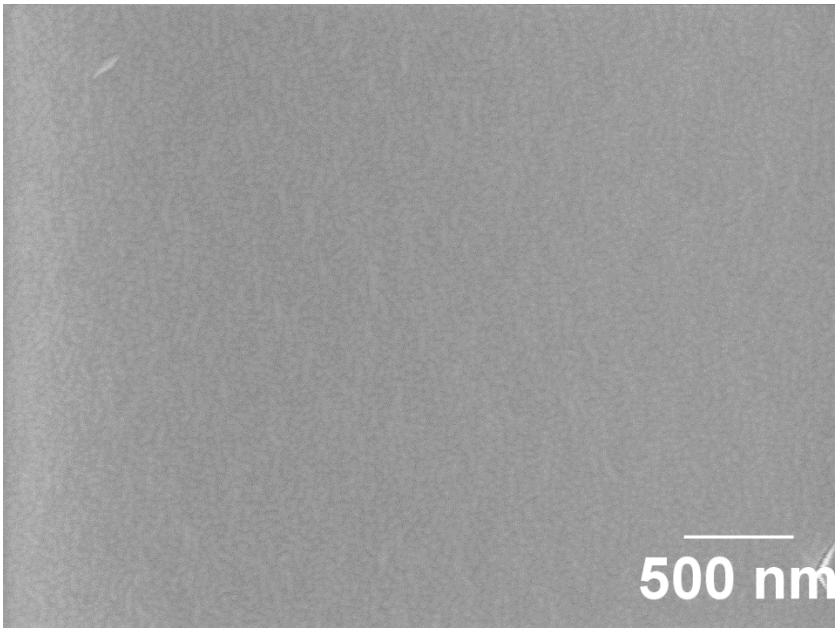

Figure 7-2 Surface morphology of $Al_{0.68}Sc_{0.32}N$/High-resistivity Si measured by SEM.

Concerning that the existence of the misoriented grains mentioned in the Chapter 5.1, the height of the misoriented grains was up to 100 nm out of the surface and caused influence in the fabrication. Change the resistivity of the substrate can influence the charge condition on the substrate, and the kinetic energy of the incoming species can be correspondingly altered. The surface morphology was

characterized by SEM, image was taken in planar view, and the surface of the $Al_{0.68}Sc_{0.32}N$/High-resistivity Si is shown in the Figure 7-2. The $Al_{0.68}Sc_{0.32}N$ shows homogeneous pebble-like surface morphology as it is grown on the low resistivity Si wafers. The amount of the visible misoriented grains in the image is almost zero, confirming the quality of the AlScN on the high-resistivity wafer is suitable for fabrication of SAW resonators.

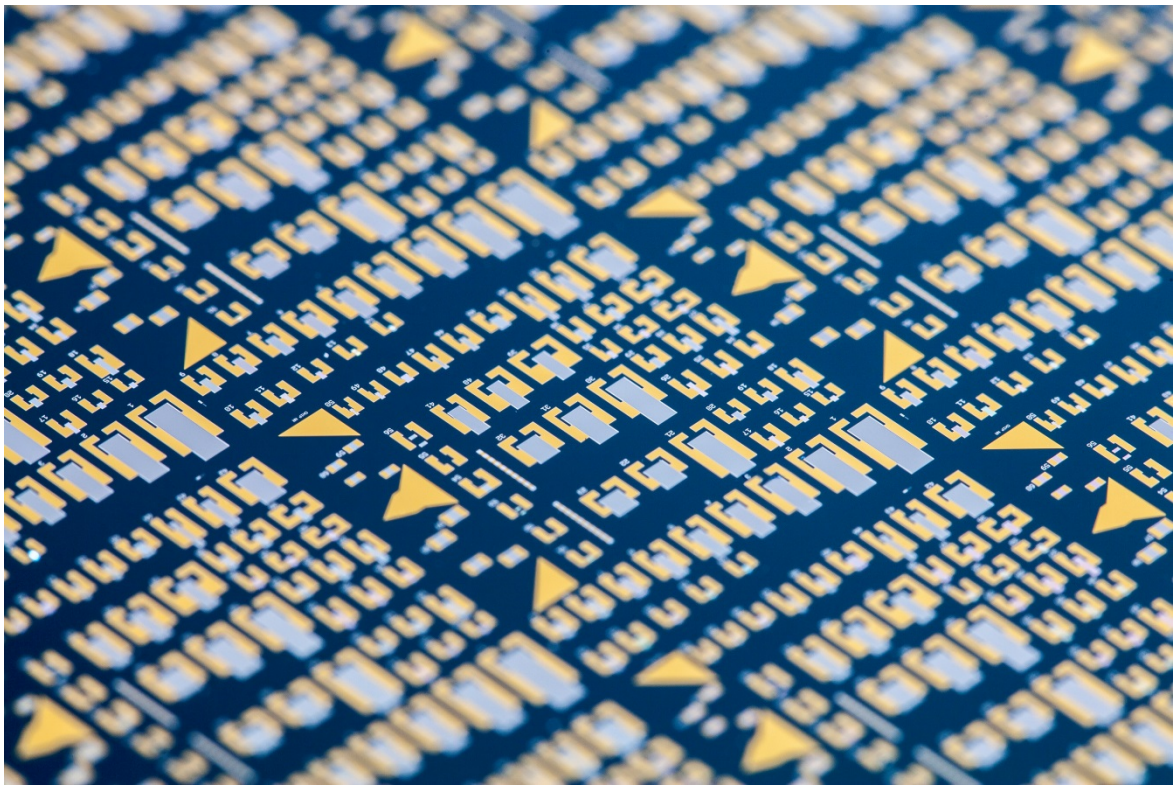

Figure 7-3 Photo of the AlScN based SAW resonators, copyright © Fraunhofer IAF

The $Al_{1-x}Sc_xN$ based SAW resonators were fabricated to evaluate the benefit of the $Al_{1-x}Sc_xN$ compared to AlN. The SAW resonators are using platinum(Pt) as IDT fingers and reflectors, better electro-mechanical coupling is expected here by using heavier mass loading of Pt instead of light metal like Al[176]. The parameter of the SAW resonators are listed in the following table, other parameter and fabrication process are reported elsewhere[177]:

Table 7-2 Parameter of the AlScN based SAW

Sc concentration x	0(AlN), 0.14, 0.32
Wavelength λ	2-24 um
Aperture W	30 λ
Number of IDT finger pairs	50
Number of reflector finger pairs	20
Thickness of IDT and reflectors electrodes	100 nm

The frequency response of the SAW resonators was characterized by Agilent E5061B network analyzer with Cascade Air Coplanar probes (350 um pitch). An open-short-load calibration with a reference sample was utilized to obtain the best precision.

7.1 Results and discussion

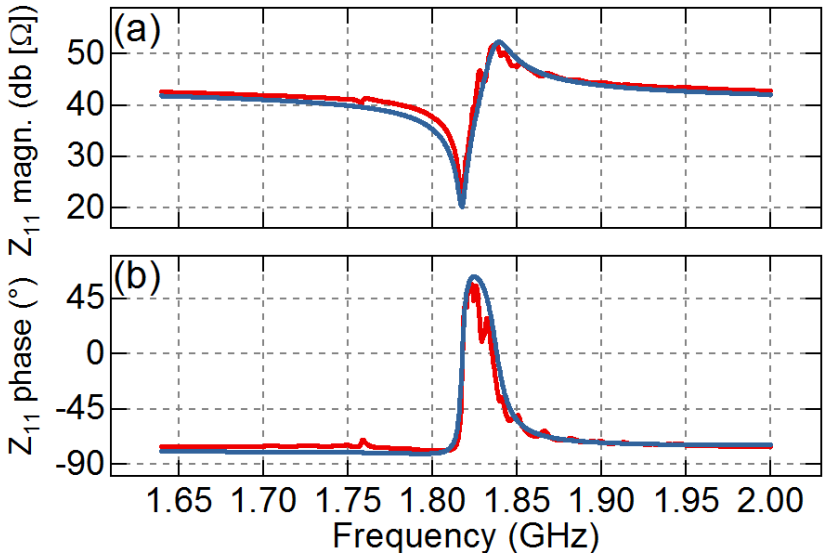

Figure 7-4 (a) Admittance and (b) phase change of the $Al_{0.68}Sc_{0.32}N$ SAW resonator with wavelength λ = 2 um(bold, blue line), fitted with modified Butterworth-Van Dyke (mBVD) model (red line) [177]

The admittance plot of the $Al_{0.68}Sc_{0.32}N$ based SAW resonator with wavelength λ = 2 um is shown in the Figure 7-4, the series resonance frequency f_s is around 1.82 GHz, according to the formula 2-16, the effective electro-mechanical coupling k_{eff}^2 is 2.2%. The resonance frequency and the coupling of the resonators with same wavelength but different Sc concentrations are listed in the following table:

Table 7-3 Resonance frequency and effective electro-mechanical coupling of AlScN based SAW

Sc concentration x	f_s (GHz)	k_{eff}^2 (%)
0(AlN)	2.08	0.5
0.14	1.97	0.9
0.32	1.82	2.2

The series resonance frequency is decreasing as the Sc concentration is increasing, from 2.08 GHz in the AlN to 1.82 GHz in the $Al_{0.68}Sc_{0.32}N$, decreased 12.5%. The decreasing of the resonance frequency is mainly due to the softening of the AlScN. According to the calculations of the elastic modulus in the Chapter 6.1, it decreases from the 535 GPa for AlN to 371 GPa in $Al_{0.68}Sc_{0.32}N$ by 31%. In the literature the decrease of the phase velocity or resonance frequency for $Al_{1-x}Sc_xN$ is also reported [178–180]. On the other hand, the effective electro-mechanical coupling is increasing from 0.5% in the AlN to the 2.2% in the $Al_{0.68}Sc_{0.32}N$, a 440% increase compared to AlN.

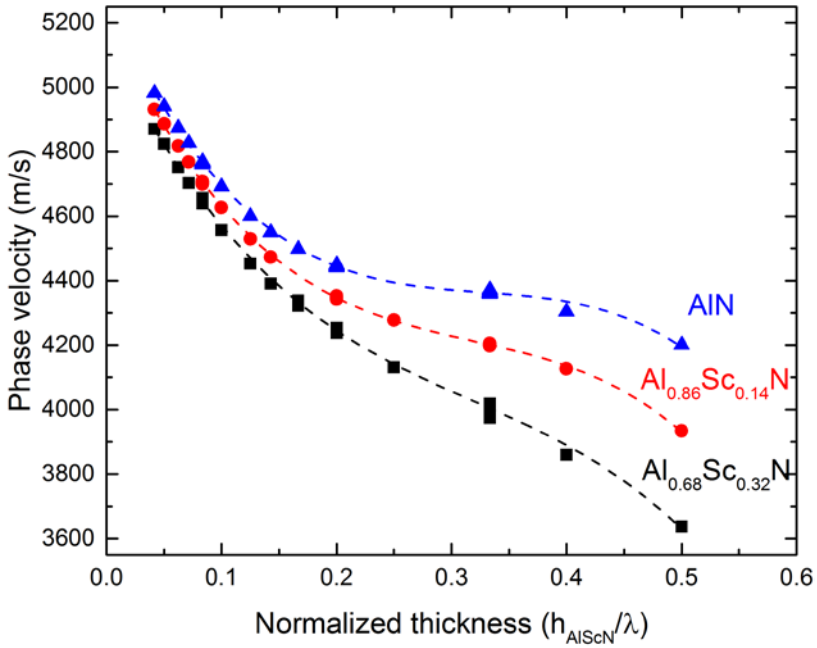

Figure 7-5 Phase velocity dispersion curve of the AlScN based SAW resonators (Sc concentration x = 0, 0.14, 0.32) as a function of normalized thickness [177]**.**

In the next step, all the resonator with wavelength λ from 2-24 um are characterized, and it is plotted as a function of normalized thickness (h_{AlScN}/λ, h_{AlScN} stands for the thickness of $Al_{1-x}Sc_xN$ layer). The phase velocity measured in h_{AlScN}/λ = 0.04 to 0.15 region is affected by the substrate due to higher penetration depth. When h_{AlScN}/λ increased further, acoustic wave is confined in the $Al_{1-x}Sc_xN$ layer due to the relatively small wavelength λ. In this case, the dispersion curves of Sc concentration from x = 0 to 0.32 differ from each other, this behavior is mainly caused by the more and more incorporation of Sc. The dispersion curve reported in [61] also indicated the decreasing phase velocity as increasing normalized thickness further until h_{AlScN}/λ reached 1.2, where the SAW resonator is based on IDT/ $Al_{1-x}Sc_xN$/single crystalline diamond.

The combination of the decrease of the resonance frequency and the increase of the electro-mechanical coupling limits the electro-acoustic application of the $Al_{1-x}Sc_xN$ based resonators. However, if we compare the 12.5% decrease in frequency exchange for the 440% increase in the coupling, and it is further increasing with even higher Sc concentration, like the Sc concentration x = 0.41 - 0.46 deposited in this work, this behavior of $Al_{1-x}Sc_xN$ will enhance the response of the resonator drastically. Meanwhile, other methods to improve the resonance frequency of $Al_{1-x}Sc_xN$ based resonator are also necessary to overcome the material softening issue, e.g. The IDT/$Al_{1-x}Sc_xN$/single crystalline diamond layer structure will have higher order modes and enjoy higher resonance frequency[61]; using ion beam to achieve smaller pitch leading to shorter wavelengths of IDT.

7.2 Summary

In this part the $Al_{1-x}Sc_xN$ thin films were sputtered on the 100 mm high resistivity Si (001) wafers and $Al_{1-x}Sc_xN$-based SAW resonators were fabricated to assess the performance of the material. The sputtered films showed 000l (l = 2, 4) peaks in the XRD $2\theta/\theta$ scan without extra reflections and rocking

curve FWHM of $Al_{1-x}Sc_xN$ 0002 peak lower than 2°, indicating the wurtzite c-axis orientation $Al_{1-x}Sc_xN$ with good crystalline quality on the high-resistivity Si wafer. The SEM planar view confirmed low density of the misoriented grains on the surface, guaranteeing appropriate surface for propagating of the SAW and convenience for the fabrication processes. The fabricated $Al_{1-x}Sc_xN$-based SAW resonators showed resonance frequency 1.82 GHz with Sc concentration x = 0.32, wavelength λ = 2 um, decreased 12.5% compared 2.09 GHz in the AlN. On the other hand the effective mechanical coupling coefficient k_{eff}^2 increased 440% than that in AlN and reached 2.2%. The high performance in the electro-mechanical coupling gives AlScN a huge potential in the high frequency application, but method to compensate the material softening issue in the high Sc concentration should be considered in the future.

8 Conclusion and outlook

8.1 Conclusion

In this dissertation the development of wurtzite $Al_{1-x}Sc_xN$ thin films with homogenous microstructure and high crystalline quality up to Sc concentration x = 0.46 was accomplished. The results achieved in this work are concluded concerning three keywords already mentioned in the beginning: microstructure, crystalline quality and piezoelectric response.

Microstructure:

The SEM images revealed a dense columnar microstructure in cross-section and pebble-like surface morphology for $Al_{1-x}Sc_xN$/Si thin films up to Sc concentration x = 0.46. All the columns in the cross-section were densely packed, well aligned to the substrate normal direction, V-shape, tilt columns or misoriented grains were eliminated by optimizing the deposition process. Models connecting microstructure, process pressure, and TSD were established based on co-sputtering geometry.

Crystalline quality:

The sputtered wurtzite$Al_{1-x}Sc_xN$ thin films are grown with c-axis orientation on both Si(001) and Al_2O_3(0001) substrates, FWHM < 2° for all compositions indicates a good crystalline quality. Misoriented grains and phase separation was not found in the optimized $Al_{1-x}Sc_xN$ thin film up to Sc concentration x = 0.46. XRD pole figures indicate fiber textured $Al_{1-x}Sc_xN(0002)/Si(001)$ and epitaxial relationship in $Al_{1-x}Sc_xN(0002)/Al_2O_3(0001)$, the epitaxial relationship was defined as $[10\bar{1}0]_{AlScN}//[11\bar{2}0]_{sapphire}$ and $(0001)_{AlScN}//(0001)_{sapphire}$.

Piezoelectric response:

$Al_{1-x}Sc_xN$/Si thin films are showing homogenous piezoelectric domains with N-polarity. The piezoelectric coefficient d_{33} = 44 pC/N is achieved by $Al_{0.54}Sc_{0.46}N$/Si, the value was obtained by correcting for different hardness of AlScN and Si substrate. It is also fitting the theoretical calculation and higher than reported value in the state-of-the-art.

To determine the mechanical properties of the AlScN for better designing of the electro-acoustic resonators, elastic modulus and coefficient of thermal expansion (CTE) of the AlScN were determined by thermal cycling method for AlScN/Si and AlScN/Al_2O_3. The elastic modulus decreased from 535 GPa for AlN to 270 GPa for $Al_{0.59}Sc_{0.41}N$, while the CTE evolved non-linearly regarding increasing Sc concentration. Preliminary results of spectroscopic ellipsometry showed the absorption in the reflectance spectra for the Sc concentration variation, indicating evolution of band gap from 5.8 eV in AlN to 4.4 eV in $Al_{0.59}Sc_{0.41}N$.

AlScN-based surface acoustic wave (SAW) resonators were fabricated to evaluate the performance of the material. $Al_{1-x}Sc_xN$ with Sc concentration up to x = 0.32 was sputtered on the high resistivity Si(001) wafers with FWHM < 2° and smooth surface. The SAW resonators with wavelength λ = 2-24 um with Pt as electrode and reflector material were fabricated. The $Al_{0.68}Sc_{0.32}N$ based SAW

resonators with λ = 2 um reached resonance frequency 1.82 GHz and electro-mechanical coupling 2.2%, respectively. As a comparison, AlN reached resonance frequency 2.09 GHz and electro-mechanical coupling 0.5%. The $Al_{0.68}Sc_{0.32}N$-based resonators showed 13.5% decrease in the resonance frequency but 440% increase in the electro-mechanical coupling, which indicates the great potential of AlScN in the electro-acoustic applications.

Last but not least, future research directions will be discussed in the next section. Besides analysis of the optical properties, other research plans include the novel material graphene: SAW resonator using $Al_{1-x}Sc_xN$ as piezoelectric material and graphene as top electrode; the growth of the $Al_{1-x}Sc_xN$ on Bragg-mirror (multiple layer structure to reflect acoustic waves) with Mo as bottom electrode and graphene as top electrode, for BAW to achieve higher resonator performance by combining high piezoelectric performance of $Al_{1-x}Sc_xN$ and mass-free electrode graphene.

8.2 Outlook

In this dissertation, the development and characterization of AlScN for electro-acoustic application was presented. The sputtered AlScN thin films on Si and Al_2O_3 were also used for the fabrication of the surface acoustic wave (SAW) resonators. At Fraunhofer IAF, the designing and fabrication of AlScN-based SAW resonators was done by A. Ding and N. Kurz. Besides, the author was also interested in combining AlScN with other material in the acoustic applications, such as graphene to fabricate the electrodes of the bulk acoustic wave (BAW) resonators. Thanks to the massless top electrode graphene, the BAW resonators achieved higher resonance frequency than the resonators with conventional Ti/Au pads[181]. As already mentioned the softening of the material by incorporation of the Sc [147], which could lead to lower resonance frequency of the electro-acoustic resonators[60,179,180]. Combining AlScN and graphene in electro-acoustic resonator could help to reach high resonance frequency as well as high electro-mechanical coupling.

Furthermore, the Sc is rare earth element, the source to obtain high purity Sc or AlSc target for sputtering is limited and normally the price of high quality Sc or AlSc target is expensive. Under such circumstances, other transition metals such as Y, Cr were also considered to the wurtzite AlN for higher piezoelectric coefficient. The potential of these alternatives were studied in the literature concerning the predicted piezoelectric coefficient and phase stability of the wurtzite structure, discussed in below.

8.2.1 AlScN-based SAW resonators with laser patterned graphene IDT

The idea to use graphene as electrode in the sensor application has drawn a lot of the attention in the recent years. Qian et al reported infrared detector combining graphene and AlN to reach the higher electro mechanical coupling and Mayorov *et al.* successfully used graphene as IDT in SAW resonators [182]. To prove the concept of the graphene-AlScN based SAW, the sketch of the shadow mask for the metal deposition and the graphene patterning was designed base on and shown below (Figure 8-1):

First, the AlScN would be sputtered and the CVD graphene would be transferred from Cu foil to the surface of the AlScN. From preliminary results, the reflectors are working when it is made by metal

with larger mass, therefore the reflectors are not made from graphene. Afterwards, the graphene is removed by the laser, there the IDT and the isolation is formed.

The fabrication of the graphene-AlScN SAW resonators was to planned investigated phase velocity thus the resonance frequency from the graphene IDT would be evaluated and the performance analyzed. When the concept is proven, the photolithography [183,184] as well as electron-beam etching could be also used to achieve higher resonance frequency. Additionally using diamond as substrate to improve the resonance frequency as well as the electro-mechanical coupling is reported [65]. However, the conductivity of the graphene should be high enough to avoid losses [185].

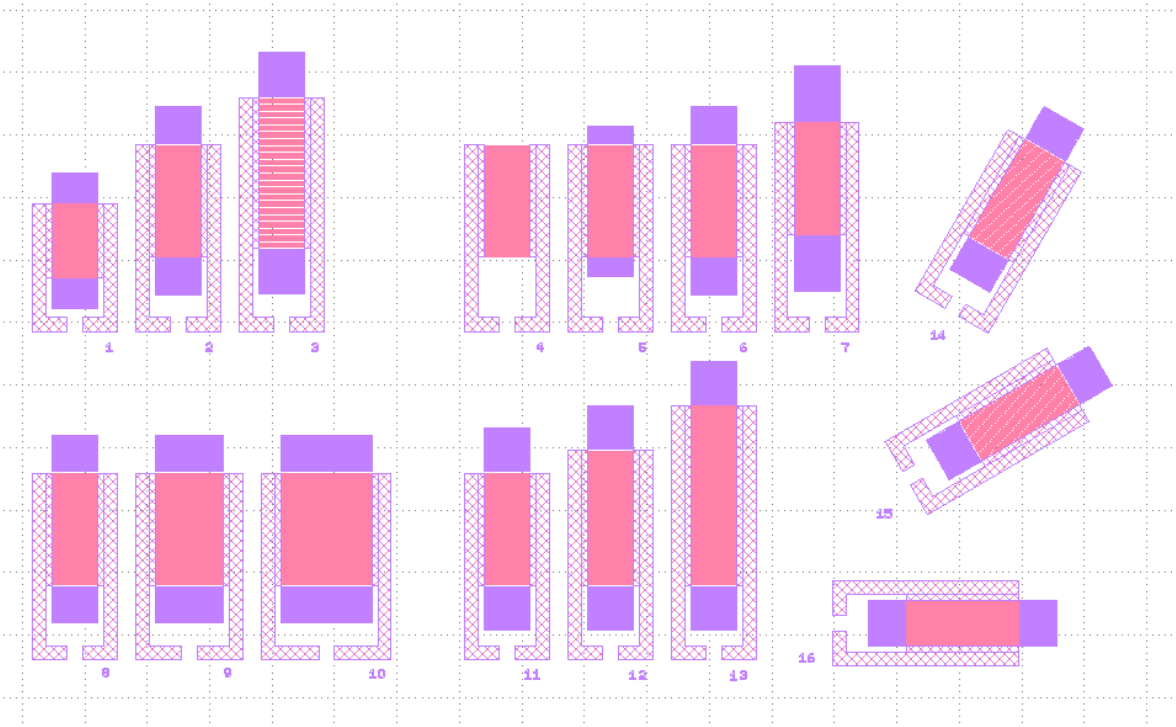

Figure 8-1 Mask of the SAW resonator with graphene as IDT and metal busbar, the purple grid parts stand for the metal busbar and purple solid parts stand for the reflectors, while the red part are covered with graphene.

8.2.2 AlScN-based BAW resonators with AlScN and graphene top electrode

The bulk acoustic wave (BAW) devices are widely used in the 3G/4G communication industry. Due to the higher electro-mechanical coupling, and higher resonance frequency [186]. Normally, the AlN-based BAW shows electro-mechanical coupling around 7%, while the $Al_{0.7}Sc_{0.3}N$ is showing 15% although the crystalline quality is degraded[4,17]. Compared to the SAW, BAW is travelling along the thickness direction, therefore it is necessary to combine bottom electrode and the top electrode. Therefore, the growth recipe of the AlScN must be adjusted to adapt to the bottom electrode, such as Mo or Pt. Literature shows [10] a distorted crystalline quality and misoriented grains in AlScN can be caused by poor quality of the bottom electrode. It makes the optimization so challenging due to the substrate and also very interesting to investigate the electro-mechanical coupling of the AlScN when the $x > 0.4$.

The proof-of-concept structure is shown in the Figure 8-2, on the Si substrate the W/SiO_2 Bragg-mirror. The aim of the Bragg-mirror is to reflect the acoustic energy back to the resonator [186]. AlScN/Mo structure with higher Sc concentration would be sputtered and the graphene would be transferred on the AlScN, as top electrode. Because the transferring of the graphene needs a smooth and homogenous layer, the surface morphology of AlScN is the key point for the optimization. In the future, the thickness of the AlScN and the Bragg-mirror could be further adjusted to achieve even higher resonance frequency and benefit from the advanced electro-mechanic coupling [187].

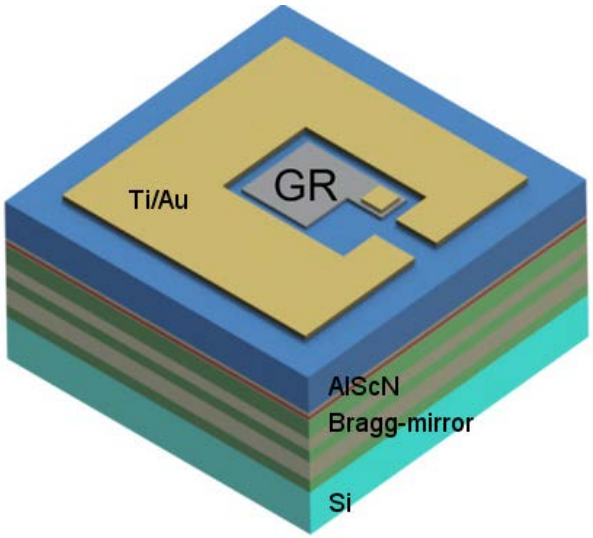

Figure 8-2 Structure of the BAW combined with AlScN and graphene, modified from [181]**. The AlScN is grown on the Mo bottom electrode. Underneath is the Si and Bragg-mirror, for reflecting the acoustic wave. The active top electrode is graphene with Au/Ti as a contact pad.**

8.2.3 Other AlN-based material

The researchers are still looking for other elements incorporating the AlN and achieve higher piezoelectric properties, including Cr and Y. The idea of synthesize AlCrN as piezoelectric material is even earlier than AlScN, in 2002 AlCrN was deposited and analyzed due to the magnetic properties [188]. Later, Manna *et al.* [189] calculated the piezoelectric response and phase stability of the AlCrN, $Al_{0.75}Cr_{0.25}N$ could reach piezoelectric coefficient d_{33} = 16.45 pC/N. However, the wurtzite structure is lost when Cr concentration is larger than x = 0.25, but it makes AlCrN still promising piezoelectric material with small Cr concentration. Žukauskaitė *et al.* [190] first reported the YAlN thin film by magnetron sputtering on Si and Al_2O_3 substrates and calculated mixing enthalpy as a function of Y concentration, indicating the wurtzite structure up to Y content of x = 0.75; Mayrhofer *et al.* [79] measured the increasing d_{33} from 3.2 pm/V in $Y_{0.01}Al_{0.99}N$ to 3.7 pm/V in $Y_{0.059}Al_{0.941}N$.

References

[1] B. Drafts, Acoustic wave technology sensors, IEEE Trans. Microw. Theory Tech. 49 (2001) 795–802. doi:10.1109/22.915466.

[2] C. Malaquin, 5G impact on RF Front End Modules & Connectivity for Cellphones 2018 report (2018).

[3] M. Akiyama, T. Kamohara, K. Kano, A. Teshigahara, Y. Takeuchi, N. Kawahara, Enhancement of Piezoelectric Response in Scandium Aluminum Nitride Alloy Thin Films Prepared by Dual Reactive Cosputtering, Adv. Mater. 21 (2009) 593–596. doi:10.1002/adma.200802611.

[4] G. Wingqvist, F. Tasnádi, A. Žukauskaitė, J. Birch, H. Arwin, L. Hultman, Increased electromechanical coupling in w-$Sc_xAl_{1-x}N$, Appl. Phys. Lett. 97 (2010) 112902. doi:10.1063/1.3489939.

[5] C. Höglund, J. Bareño, J. Birch, B. Alling, Z. Czigány, L. Hultman, Cubic $Sc_{1-x}Al_xN$ solid solution thin films deposited by reactive magnetron sputter epitaxy onto ScN(111), J. Appl. Phys. 105 (2009) 113517. doi:10.1063/1.3132862.

[6] M. Reusch, S. Cherneva, Y. Lu, A. Žukauskaitė, L. Kirste, K. Holc, M. Datcheva, D. Stoychev, V. Lebedev, O. Ambacher, Microstructure and mechanical properties of stress-tailored piezoelectric AlN thin films for electro-acoustic devices, Appl. Surf. Sci. 407 (2017) 307–314. doi:10.1016/j.apsusc.2017.02.147.

[7] S. Mishin, D.R. Marx, B. Sylvia, V. Lughi, K.L. Turner, D.R. Clarke, Sputtered AlN thin films on Si and electrodes for MEMS resonators: relationship between surface quality microstructure and film properties, in: IEEE Symp. Ultrason. 2003, IEEE, 2003: pp. 2028–2032. doi:10.1109/ULTSYM.2003.1293316.

[8] J. Olivares, S. González-Castilla, M. Clement, A. Sanz-Hervás, L. Vergara, J. Sangrador, E. Iborra, Combined assessment of piezoelectric AlN films using X-ray diffraction, infrared absorption and atomic force microscopy, Diam. Relat. Mater. 16 (2007) 1421–1424. doi:10.1016/j.diamond.2006.11.065.

[9] C.S. Sandu, F. Parsapour, S. Mertin, V. Pashchenko, R. Matloub, T. LaGrange, B. Heinz, P. Muralt, Abnormal Grain Growth in AlScN Thin Films Induced by Complexion Formation at Crystallite Interfaces, Phys. Status Solidi. 216 (2019) 1800569. doi:10.1002/pssa.201800569.

[10] S. Fichtner, N. Wolff, G. Krishnamurthy, A. Petraru, S. Bohse, F. Lofink, S. Chemnitz, H. Kohlstedt, L. Kienle, B. Wagner, Identifying and overcoming the interface originating c-axis instability in highly Sc enhanced AlN for piezoelectric

micro-electromechanical systems, J. Appl. Phys. 122 (2017) 035301. doi:10.1063/1.4993908.

[11] T. Kamohara, M. Akiyama, N. Ueno, M. Sakamoto, K. Kano, A. Teshigahara, N. Kawahara, N. Kuwano, Influence of sputtering pressure on polarity distribution of aluminum nitride thin films, Appl. Phys. Lett. 89 (2006) 10–13. doi:10.1063/1.2405849.

[12] R.F. Mould, Pierre Curie, 1859-1906, Curr. Oncol. 14 (2007) 74–82. doi:10.3747/co.2007.110.

[13] P. Dineva, D. Gross, R. Müller, T. Rangelov, Dynamic Fracture of Piezoelectric Materials, 212 (2014). doi:10.1007/978-3-319-03961-9.

[14] W. Voigt, Lehrbuch der Kristallphysik, 1966. doi:10.1007/978-3-663-15884-4.

[15] A. Arnau, D. Soares, Fundamentals of Piezoelectricity, in: Piezoelectric Transducers Appl., Springer Berlin Heidelberg, Berlin, Heidelberg, 2008: pp. 1–38. doi:10.1007/978-3-540-77508-9_1.

[16] O. Ambacher, J. Majewski, C. Miskys, A. Link, M. Hermann, M. Eickhoff, M. Stutzmann, F. Bernardini, V. Fiorentini, V. Tilak, B. Schaff, L.F. Eastman, Pyroelectric properties of Al(In)GaN/GaN hetero- and quantum well structures, J. Phys. Condens. Matter. 14 (2002) 3399–3434. doi:10.1088/0953-8984/14/13/302.

[17] G. Wingqvist, Electro-acoustic sensors based on AlN thin film: Possibilities and limitations, SPIE. 8066 (2011). doi:10.1117/12.890662.

[18] G. Wingqvist, F. Tasnádi, A. Žukauskaitė, J. Birch, H. Arwin, L. Hultman, Increased electromechanical coupling in w-$Sc_xAl_{1-x}N$, Appl. Phys. Lett. 97 (2010) 112902. doi:10.1063/1.3489939.

[19] G. Piazza, V. Felmetsger, P. Muralt, R.H. Olsson III, R. Ruby, Piezoelectric aluminum nitride thin films for microelectromechanical systems, MRS Bull. 37 (2012) 1051–1061. doi:10.1557/mrs.2012.268.

[20] F. Bernardini, V. Fiorentini, D. Vanderbilt, Spontaneous polarization and piezoelectric constants of III-V nitrides, Phys. Rev. B. 56 (1997) 4. doi:10.1103/PhysRevB.56.R10024.

[21] O. Ambacher, J. Smart, J.R. Shealy, N.G. Weimann, K. Chu, M. Murphy, W.J. Schaff, L.F. Eastman, R. Dimitrov, L. Wittmer, M. Stutzmann, W. Rieger, J. Hilsenbeck, Two-dimensional electron gases induced by spontaneous and piezoelectric polarization charges in N- and Ga-face AlGaN/GaN heterostructures, J. Appl. Phys. 85 (1999) 3222. doi:10.1063/1.369664.

[22] V. Fuflyigin, E. Salley, A. Osinsky, P. Norris, Pyroelectric properties of AlN, Appl. Phys. Lett. 77 (2000) 3075–3077. doi:10.1063/1.1324726.

[23] M. Akiyama, T. Kamohara, K. Kano, A. Teshigahara, N. Kawahara, Influence of oxygen concentration in sputtering gas on piezoelectric response of aluminum nitride thin films, Appl. Phys. Lett. 93 (2008) 2008–2010. doi:10.1063/1.2957654.

[24] M. Noorprajuda, M. Ohtsuka, H. Fukuyama, Polarity inversion of AlN film grown on nitrided a-plane sapphire substrate with pulsed DC reactive sputtering Polarity inversion of AlN film grown on nitrided a -plane sapphire substrate with pulsed DC reactive sputtering, AIP Advances. 045124 (2018). doi:10.1063/1.5024996.

[25] E. Milyutin, S. Harada, D. Martin, J.F. Carlin, N. Grandjean, V. Savu, O. Vaszquez-Mena, J. Brugger, P. Muralt, Sputtering of (001)AlN thin films: Control of polarity by a seed layer, J. Vac. Sci. Technol. B Microelectron. Nanom. Struct. 28 (2010) L61. doi:10.1116/1.3501117.

[26] J. Bjurström, G. Wingqvist, I. Katardjiev, Synthesis of textured thin piezoelectric AlN films with a nonzero c-axis mean tilt for the fabrication of shear mode resonators, Proc. - IEEE Ultrason. Symp. 1 (2005) 321–324. doi:10.1109/ULTSYM.2005.1602859.

[27] M. DeMiguel-Ramos, T. Mirea, M. Clement, J. Olivares, J. Sangrador, E. Iborra, Optimized tilted c-axis AlN films for improved operation of shear mode resonators, Thin Solid Films. 590 (2015) 219–223. doi:10.1016/j.tsf.2015.08.010.

[28] W.M. Yim, E.J. Stofko, P.J. Zanzucchi, J.I. Pankove, M. Ettenberg, S.L. Gilbert, Epitaxially grown AlN and its optical band gap, J. Appl. Phys. 44 (1973) 292–296. doi:10.1063/1.1661876.

[29] K. Kornitzer, W. Limmer, K. Thonke, R. Sauer, D.G. Ebling, L. Steinke, K.W. Benz, AlN on sapphire and on SiC: CL and Raman study, J. Cryst. Growth. 201 (1999) 441–443. doi:10.1016/S0022-0248(98)01371-2.

[30] V.Y. Davydov, Y.E. Kitaev, I.N. Goncharuk, a N. Smirnov, J. Graul, O. Semchinova, D. Uffmann, M.B. Smirnov, a P. Mirgorodsky, R. a Evarestov, Phonon dispersion and Raman scattering in hexagonal GaN and AlN, Phys. Rev. B. 58 (1998) 12899–12907. doi:10.1103/PhysRevB.58.12899.

[31] A. Sarua, M. Kuball, J.E. Van Nostrand, Deformation potentials of the E_2 (high) phonon mode of AlN, Appl. Phys. Lett. 2 (2008) 10–13. doi:10.1063/1.1501762.

[32] M. Kuball, Raman spectroscopy of GaN, AlGaN and AlN for process and growth monitoring/control, Surf. Interface Anal. 31 (2001) 987–999. doi:10.1002/sia.1134.

[33] H. Iwanaga, A. Kunishige, S. Takeuchi, Anisotropic thermal expansion in wurtzite-type crystals, J. Mater. Sci. 35 (2000) 2451–2454. doi:10.1023/A:1004709500331.

[34] W.M. Yim, R.J. Paff, Thermal expansion of AlN, sapphire, and silicon, J. Appl. Phys. 45 (1974) 1456–1457. doi:10.1063/1.1663432.

[35] S. Figge, H. Kröncke, D. Hommel, B.M. Epelbaum, Temperature dependence of the thermal expansion of AlN, Appl. Phys. Lett. 94 (2009) 101915. doi:10.1063/1.3089568.

[36] R.E. Sah, L. Kirste, M. Baeumler, P. Hiesinger, V. Cimalla, V. Lebedev, H. Baumann, H.-E. Zschau, Residual stress stability in fiber textured stoichiometric AlN film grown using rf magnetron sputtering, J. Vac. Sci. Technol. A Vacuum, Surfaces, Film. 28 (2010) 394–399. doi:10.1116/1.3360299.

[37] E. Ruiz, S. Alvarez, P. Alemany, Electronic structure and properties of AlN, Phys. Rev. B. 49 (1994) 7115–7123. doi:10.1103/PhysRevB.49.7115.

[38] G. F. Iriarte, AlN thin film electroacoustic devices(Doctoral disseration), 2003. doi:10.5369/JSST.2014.23.2.94.

[39] M. Alevli, C. Ozgit, I. Donmez, N. Biyikli, Structural properties of AlN films deposited by plasma-enhanced atomic layer deposition at different growth temperatures, Phys. Status Solidi. 209 (2012) 266–271. doi:10.1002/pssa.201127430.

[40] K. Tonisch, V. Cimalla, C. Foerster, H. Romanus, O. Ambacher, D. Dontsov, Piezoelectric properties of polycrystalline AlN thin films for MEMS application, Sensors Actuators A Phys. 132 (2006) 658–663. doi:10.1016/j.sna.2006.03.001.

[41] X. Bai, M.E. Kordesch, Structure and optical properties of ScN thin films, Appl. Surf. Sci. 175-176 (2001) 499–504.

[42] J.P. Dismukes, W.M. Yim, V.S. Ban, Epitaxial growth and properties of semiconducting ScN, J. Cryst. Growth. 13-14 (1972) 365–370. doi:10.1016/0022-0248(72)90185-6.

[43] M. A. Moram, Z.H. Barber, C.J. Humphreys, The effect of oxygen incorporation in sputtered scandium nitride films, Thin Solid Films. 516 (2008) 8569–8572. doi:10.1016/j.tsf.2008.05.050.

[44] H. Al-Brithen, A.R. Smith, Molecular beam epitaxial growth of atomically smooth scandium nitride films, Appl. Phys. Lett. 77 (2000) 2485. doi:10.1063/1.1318227.

[45] M.A. Moram, C.F. Johnston, M.J. Kappers, C.J. Humphreys, Defect reduction in nonpolar and semipolar GaN using scandium nitride interlayers, J. Cryst. Growth. 311 (2009) 3239–3242. doi:10.1016/j.jcrysgro.2009.03.029.

[46] M. A. Moram, Z.H. Barber, C.J. Humphreys, T.B. Joyce, P.R. Chalker, Young's modulus, Poisson's ratio, and residual stress and strain in (111)-oriented scandium nitride thin films on silicon, J. Appl. Phys. 100 (2006). doi:10.1063/1.2217106.

[47] R. Deng, AlN , ScN , and Al-Sc-N Ternary Alloys : Structural , Optical , and Electrical Properties(Doctoral dissertation), (2013).

[48] N. Farrer, L. Bellaiche, Properties of hexagonal ScN versus wurtzite GaN and InN, Phys. Rev. B - Condens. Matter Mater. Phys. 66 (2002) 2012031–2012034. doi:10.1103/PhysRevB.66.201203.

[49] V. Ranjan, L. Bellaiche, E.J. Walter, Strained hexagonal ScN: a material with unusual structural and optical properties., Phys. Rev. Lett. 90 (2003) 257602. doi:10.1103/PhysRevLett.90.257602.

[50] C. Höglund, J. Birch, B. Alling, J. Bareño, Z. Czigány, P.O.Å. Persson, G. Wingqvist, A. Žukauskaitė, L. Hultman, Wurtzite structure $Sc_{1-x}Al_xN$ solid solution films grown by reactive magnetron sputter epitaxy: Structural characterization and first-principles calculations, J. Appl. Phys. 107 (2010) 123515. doi:10.1063/1.3448235.

[51] M. Akiyama, K. Kano, A. Teshigahara, Influence of growth temperature and scandium concentration on piezoelectric response of scandium aluminum nitride alloy thin films, Appl. Phys. Lett. 95 (2009) 2009–2011. doi:10.1063/1.3251072.

[52] S. Zhang, D. Holec, W.Y. Fu, C.J. Humphreys, M.A. Moram, Tunable optoelectronic and ferroelectric properties in Sc-based III-nitrides, J. Appl. Phys. 114 (2013) 133510. doi:10.1063/1.4824179.

[53] M.A. Caro, S. Zhang, T. Riekkinen, M. Ylilammi, M.A. Moram, O. Lopez-Acevedo, J. Molarius, T. Laurila, Piezoelectric coefficients and spontaneous polarization of ScAlN, J. Phys. Condens. Matter. 27 (2015) 245901. doi:10.1088/0953-8984/27/24/245901.

[54] S. Zhang, W.Y. Fu, D. Holec, C.J. Humphreys, M.A. Moram, Elastic constants and critical thicknesses of ScGaN and ScAlN, J. Appl. Phys. 114 (2013) 243516. doi:10.1063/1.4848036.

[55] M.A. Moram, S. Zhang, ScGaN and ScAlN: emerging nitride materials, J. Mater. Chem. A. 2 (2014) 6042–6050. doi:10.1039/C3TA14189F.

[56] A. Zukauskaite, G. Wingqvist, J. Palisaitis, J. Jensen, P.O.Å. Persson, R. Matloub, P. Muralt, Y. Kim, J. Birch, L. Hultman, Microstructure and dielectric properties of piezoelectric magnetron sputtered w-Sc x Al 1−x N thin films, J. Appl. Phys. 111 (2012) 093527. doi:10.1063/1.4714220.

[57] P.M. Mayrhofer, C. Eisenmenger-Sittner, M. Stöger-Pollach, H. Euchner, A. Bittner, U. Schmid, The impact of argon admixture on the c-axis oriented growth of direct current magnetron sputtered Sc x Al 1−x N thin films, J. Appl. Phys. 115 (2014) 193505. doi:10.1063/1.4876260.

[58] P.M. Mayrhofer, H. Euchner, A. Bittner, U. Schmid, Circular test structure for the determination of piezoelectric constants of $Sc_xAl_{1-x}N$ thin films applying Laser Doppler Vibrometry and FEM simulations, Sensors Actuators, A Phys. 222 (2015) 301–308. doi:10.1016/j.sna.2014.10.024.

[59] V.V. Felmetsger, Sputter technique for deposition of AlN, ScAlN, and Bragg reflector thin films in mass production, in: 2017 IEEE Int. Ultrason. Symp., IEEE, 2017. 1–5. doi:10.1109/ULTSYM.2017.8092612.

[60] M. Gillinger, K. Shaposhnikov, T. Knobloch, M. Schneider, M. Kaltenbacher, U. Schmid, Impact of layer and substrate properties on the surface acoustic wave velocity in scandium doped aluminum nitride based SAW devices on sapphire, Appl. Phys. Lett. 108 (2016). doi:10.1063/1.4953259.

[61] K. Hashimoto, T. Fujii, S. Sato, T. Omori, C. Ahn, High Q Surface Acoustic Wave Resonators in 2-3 GHz Range Using ScAlN / Single Crystalline Diamond Structure, (2012) 1926–1929.

[62] Q.Z. Zhang, T. Han, W.B. Wang, K.Y. Hashimoto, J. Chen, Surface acoustic wave propagation characteristics of ScAlN/diamond structure with buried electrode, Proc. 2014 Symp. Piezoelectricity, Acoust. Waves Device Appl. SPAWDA., 2014. 271–274. doi:10.1109/SPAWDA.2014.6998578.

[63] V. Pashchenko, R. Matloub, F. Parsapourkolour, P. Muralt, S. Ballandras, K. Haffner, Hybrid BAW/SAW AlN and AlScN thin film resonator, IEEE Int. Ultrason. Symp. IUS. 2016. 1–4. doi:10.1109/ULTSYM.2016.7728649.

[64] B. Heinz, S. Mertin, O. Rattunde, M.A. Dubois, S. Nicolay, G. Christmann, M. Tschirky, P. Muralt, Sputter deposition technology for Al(1-x)ScxN films with high Sc concentration, China Semicond. Technol. Int. Conf. 2017, CSTIC 2017. 2 2017. 5–7. doi:10.1109/CSTIC.2017.7919885.

[65] Q. Zhang, T. Han, J. Chen, W. Wang, K. Hashimoto, Enhanced coupling factor of surface acoustic wave devices employing ScAlN/diamond layered structure with embedded electrodes, Diam. Relat. Mater. 58 (2015) 31–34. doi:10.1016/j.diamond.2015.06.001.

[66] V. Felmetsger, M. Mikhov, M. Demiguel-Ramos, M. Clement, J. Olivares, T. Mirea, E. Iborra, Sputtered $Al_{1-x}Sc_xN$ thin films with high areal uniformity for mass production, 2015 Jt. Conf. IEEE Int. Freq. Control Symp. Eur. Freq. Time Forum, FCS 2015 - Proc. 2015. 117–120. doi:10.1109/FCS.2015.7138803.

[67] R. Matloub, M. Hadad, A. Mazzalai, N. Chidambaram, G. Moulard, C.S. Sandu, T. . Metzger, P. Muralt, Piezoelectric Al1-xScxN thin films: A semiconductor compatible solution for mechanical energy harvesting and sensors, Appl. Phys. Lett. 102 (2013) 10–13. doi:10.1063/1.4800231.

[68] M.T. Hardy, B.P. Downey, N. Nepal, D.F. Storm, D.S. Katzer, D.J. Meyer, Epitaxial ScAlN grown by molecular beam epitaxy on GaN and SiC substrates, Appl. Phys. Lett. 110 (2017) 162104. doi:10.1063/1.4981807.

[69] A. Dittmar, C. Hartmann, J. Wollweber, M. Bickermann, M. Schmidbauer, D. Klimm, Physical Vapor Transport Growth of bulk $Al_{1-x}Sc_xN$ Single Crystals, J. Cryst. Growth. 500 (2018) 74-79 doi:10.1016/j.jcrysgro.2018.07.022.

[70] W.R. Grove, On the Electro-Chemical Polarity of Gases, Philos. Trans. R. Soc. London. 142 (1852) 87–101. doi:10.1098/rstl.1852.0008.

[71] D.J. Christie, W.D. Sproul, D. Carter, Mid-Frequency Dual Magnetron Reactive Co-sputtering for Deposition of Customized Index Optical Films, 46th Annu. Tech. Conf. Proc. 2003. 393–398.

[72] P.J. Kelly, R.. D. Arnell, Magnetron sputtering: a review of recent developments and applications, Vacuum. 56 (2000) 159–172. doi:10.1016/S0042-207X(99)00189-X.

[73] R.F. Bunshah, Handbook of Deposition Technolgies for Films and Coatings, 1994.

[74] D. Depla, S. Mahieu, J. Greene, Sputter deposition processes, Handb. Depos. Technol. Film. Coatings. 281 (1991) 253–296. doi:10.1016/B978-0-8155-2031-3.00005-3.

[75] K.P. Almtoft, Structural Characterization of Nanocrystalline Thin Films Grown by Magnetron Sputtering, PhD Thesis. (2006).

[76] H. Lee, Effect of negative bias voltage on the microstructures of AlN thin films fabricated by reactive r.f. magnetron sputtering, J. Mater. Sci. 8 (1997) 385–390.

[77] J.Y. Zhang, H. Kuwano, Q. Wang, Z. Cao, Microstructure and piezoelectric properties of AlN thin films grown on stainless steel for the application of vibration energy harvesting, Micro Nano Lett. 7 (2012) 1170–1172. doi:10.1049/mnl.2012.0545.

[78] R. Miyagawa, S. Yang, H. Miyake, K. Hiramatsu, T. Kuwahara, M. Mitsuhara, N. Kuwano, Microstructure of AlN grown on a nucleation layer on a sapphire substrate, Appl. Phys. Express. 5 (2012) 025501. doi:10.1143/APEX.5.025501.

[79] P.M. Mayrhofer, H. Riedl, H. Euchner, M. Stöger-Pollach, P.H. Mayrhofer, A. Bittner, U. Schmid, Microstructure and piezoelectric response of YxAl1−xN thin films, Acta Mater. 100 (2015) 81–89. doi:10.1016/j.actamat.2015.08.019.

[80] W.J. Liauh, S. Wu, J.L. Huang, D.F. Lii, Z.X. Lin, W.K. Yeh, Microstructure and piezoelectric properties of reactively sputtered highly C-axis $Sc_xAl_{1-x}N$ thin films on diamond-like carbon/Si substrate, Surf. Coatings Technol. (2016). doi:10.1016/j.surfcoat.2016.06.097.

[81] C. V Thompson, Structure Evolution During Processing of Polycrystalline Films, Annu. Rev. Mater. Sci. 30 (2000) 159–190. doi:10.1146/annurev.matsci.30.1.159.

[82] M. Ohring, The Materials Science of Thin Films, Elsevier 1992. doi: 10.1016/B978-0-12-524975-1.X5000-9

[83] S. Mahieu, P. Ghekiere, D. Depla, R. De Gryse, Biaxial alignment in sputter deposited thin films, Thin Solid Films. 515 (2006) 1229–1249. doi:10.1016/j.tsf.2006.06.027.

[84] J.A. Thornton, Structure-Zone Models of Thin Films, Proc. SPIE 0821, 1988. 95–105. doi:10.1117/12.941846.

[85] J.A. Thornton, The microstructure of sputter-deposited coatings, J. Vac. Sci. Technol. A Vacuum, Surfaces, Film. 4 (1986) 3059. doi:10.1116/1.573628.

[86] R. Messier, Revised structure zone model for thin film physical structure, J. Vac. Sci. Technol. A Vacuum, Surfaces, Film. 2 (1984) 500. doi:10.1116/1.572604.

[87] R.C. Ross, R. Messier, Reactive sputtering of amorphous silicon in Ne, Ar, and Kr, J. Appl. Phys. 54 (1983) 5744–5749. doi:10.1063/1.331797.

[88] M. Birkholz, Thin Film Analysis by X-Ray Scattering, Wiley-VCH Verlag GmbH & Co. KGaA, Weinheim, FRG, 2005. doi:10.1002/3527607595.

[89] H. Takeuchi, M. Ohtsuka, H. Fukuyama, Effect of sputtering power on surface characteristics and crystal quality of AlN films deposited by pulsed DC reactive sputtering, Phys. Status Solidi. 252 (2015) 1163–1171. doi:10.1002/pssb.201451599.

[90] J.I. Goldstein, D.E. Newbury, P. Echlin, D.C. Joy, C.E. Lyman, E. Lifshin, L. Sawyer, J.R. Michael, Scanning Electron Microscopy and X-ray Microanalysis, Scanning Electron Microsc. X-Ray Microanal. (2003) 21–32. doi:10.1007/978-1-4615-0215-9.

[91] R. Fitzgerald, K. Keil, K.F.J. Heinrich, Solid-State Energy-Dispersion Spectrometer for Electron-Microprobe X-ray Analysis, Science. 159 (1968) 528–530. doi:10.1126/science.159.3814.528.

[92] P. Carpenter, E. Vicenzi, R. Gauvin, J. Fournelle, The Legacy of Raimond Castaing: A Perspective at 60 Years, Microsc. Microanal. 17 (2011) 546–547. doi:10.1017/S1431927611003606.

[93] G. Binnig, C.F. Quate, C. Gerber, Atomic Force Microscope, Phys. Rev. Lett. 56 (1986) 930–933. doi:10.1103/PhysRevLett.56.930.

[94] P. Eaton, P. West, Atomic Force Microscopy, Oxford University Press, 2010. doi:10.1093/acprof:oso/9780199570454.001.0001.

[95] Nanosensors, PointProbe ® Plus, Product specification, https://www.nanosensors.com/PointProbe-Plus-Non-Contact-Tapping-Mode-High-Resonance-Frequency-Reflex-Coating-afm-tip-PPP-NCHR

[96] P. Güthner, K. Dransfeld, Local poling of ferroelectric polymers by scanning force microscopy, Appl. Phys. Lett. 61 (1992) 1137–1139. doi:10.1063/1.107693.

[97] S. Kalinin, D. Bonnell, Imaging mechanism of piezoresponse force microscopy of ferroelectric surfaces, Phys. Rev. B. 65 (2002) 1–11. doi:10.1103/PhysRevB.65.125408.

[98] S.V. Kalinin, E.A. Eliseev, A.N. Morozovska, Materials contrast in piezoresponse force microscopy, Appl. Phys. Lett. 88 (2006). doi:10.1063/1.2206992.

[99] C. Harnagea, A. Pignolet, M. Alexe, D. Hesse, Piezoresponse Scanning Force Microscopy: What Quantitative Information Can We Really Get Out of Piezoresponse Measurements on Ferroelectric Thin Films, Integr. Ferroelectr. 44 (2002) 113–124. doi:10.1080/713718197.

[100] S. Jesse, B. Mirman, S.V. Kalinin, Resonance enhancement in piezoresponse force microscopy: Mapping electromechanical activity, contact stiffness, and Q factor, Appl. Phys. Lett. 89 (2006). doi:10.1063/1.2221496.

[101] S. Jesse, A.P. Baddorf, S.V. Kalinin, Dynamic behaviour in piezoresponse force microscopy, Nanotechnology. 17 (2006) 1615–1628. doi:10.1088/0957-4484/17/6/014.

[102] P.M. Mayrhofer, E. Wistrela, M. Kucera, A. Bittner, U. Schmid, Fabrication and characterisation of ScAlN-based piezoelectric MEMS cantilevers, 2015 Transducers - 2015 18th Int. Conf. Solid-State Sensors, Actuators Microsystems. (2015) 2144–2147. doi:10.1109/TRANSDUCERS.2015.7181383.

[103] S. Barth, H. Bartzsch, D. Glöß, P. Frach, T. Modes, O. Zywitzki, G. Suchaneck, G. Gerlach, Magnetron sputtering of piezoelectric AlN and AlScN thin films and their use in energy harvesting applications, Microsyst. Technol. 9517 (2016) 1–5. doi:10.1007/s00542-015-2787-x.

[104] P.M. Mayrhofer, P.O.Å. Persson, A. Bittner, U. Schmid, Properties of $Sc_xAl_{1-x}N$ (x = 0.27) thin films on sapphire and silicon substrates upon high temperature loading, Microsyst. Technol. 22 (2016) 1679–1689. doi:10.1007/s00542-015-2798-7.

[105] G. Markys, Characterisation of Ferroelectric Bulk Materials and Thin Films, Springer Netherlands, Dordrecht, 2014. doi:10.1007/978-1-4020-9311-1.

[106] M. Reusch, K. Holc, W. Pletschen, L. Kirste, A. Žukauskaitė, T. Yoshikawa, D. Iankov, O. Ambacher, V. Lebedev, Analysis and optimization of sputter deposited AlN-layers for flexural plate wave devices, J. Vac. Sci. Technol. B, Nanotechnol. Microelectron. Mater. Process. Meas. Phenom. 34 (2016) 052001. doi:10.1116/1.4959580.

[107] F.J. Manjón, D. Errandonea, A.H. Romero, N. Garro, J. Serrano, M. Kuball, Lattice dynamics of wurtzite and rocksalt AlN under high pressure: Effect of compression on the crystal anisotropy of wurtzite-type semiconductors, Phys. Rev. B - Condens. Matter Mater. Phys. 77 (2008) 1–16. doi:10.1103/PhysRevB.77.205204.

[108] H. Harima, Properties of GaN and related compounds studied by means of Raman scattering, J. Phys. Condens. Matter. 14 (2002) R967–R993. doi:10.1088/0953-8984/14/38/201.

[109] R. Deng, K. Jiang, D. Gall, Optical phonon modes in Al1-xScxN, J. Appl. Phys. 115 (2014). doi:10.1063/1.4861034.

[110] J. a. Woollam, B.D. Johs, C.M. Herzinger, J.N. Hilfiker, R. a. Synowicki, C.L. Bungay, Overview of variable-angle spectroscopic ellipsometry (VASE): I. Basic theory and typical applications, 1999. 1029402. doi:10.1117/12.351660.

[111] H. Fujiwara, Spectroscopic Ellipsometry, John Wiley & Sons, Ltd, Chichester, UK, 2007. doi:10.1002/9780470060193.

[112] R. Paniagua-Domínguez, Y.F. Yu, A.E. Miroshnichenko, L.A. Krivitsky, Y.H. Fu, V. Valuckas, L. Gonzaga, Y.T. Toh, A.Y.S. Kay, B. Lukyanchuk, A.I. Kuznetsov, Generalized Brewster effect in dielectric metasurfaces, Nat. Commun. 7 (2016). doi:10.1038/ncomms10362.

[113] J.M. Khoshman, M.E. Kordesch, Optical characterization of sputtered amorphous aluminum nitride thin films by spectroscopic ellipsometry, J. Non. Cryst. Solids. 351 (2005) 3334–3340. doi:10.1016/j.jnoncrysol.2005.08.009.

[114] K.K.S. Lau, J.A. Caulfield, K.K. Gleason, Variable angle spectroscopic ellipsometry of fluorocarbon films from hot filament chemical vapor deposition, J. Vac. Sci. Technol. A Vacuum, Surfaces, Film. 18 (2000) 2404. doi:10.1116/1.1288191.

[115] R. Yusoh, M. Horprathum, P. Eiamchai, P. Chindaudom, K. Aiempanakit, Determination of optical and physical properties of ZrO2 films by spectroscopic ellipsometry, Procedia Eng. 32 (2012) 745–751. doi:10.1016/j.proeng.2012.02.007.

[116] A. Iqbal, F. Mohd-Yasin, Reactive sputtering of aluminum nitride (002) thin films for piezoelectric applications: A review, Sensors (Switzerland). 18 (2018) 1–21. doi:10.3390/s18061797.

[117] G.F. Iriarte, Influence of the magnetron on the growth of aluminum nitride thin films deposited by reactive sputtering, J. Vac. Sci. Technol. A Vacuum, Surfaces Film. 28 (2010) 193–198. doi:10.1116/1.3280174.

[118] J.L. Tang, D. Niu, Y. Yang, D. Zhou, C. Yang, Preparation of ScAlN films as a function of sputtering atmosphere, J. Mater. Sci. Mater. Electron. 27 (2016) 4788–4793. doi:10.1007/s10854-016-4359-y.

[119] Y. Chen, R. Wang, B. Wang, T. Xing, X. Song, M. Zhu, H. Yan, Effects of mean free path on the preferentially orientated growth of AlN thin films, J. Cryst. Growth. 283 (2005) 315–319. doi:10.1016/j.jcrysgro.2005.06.007.

[120] M. Clement, E. Iborra, J. Sangrador, A. Sanz-Hervás, L. Vergara, M. Aguilar, Influence of sputtering mechanisms on the preferred orientation of aluminum nitride thin films, J. Appl. Phys. 94 (2003) 1495–1500. doi:10.1063/1.1587267.

[121] M. Ishihara, S. Li, H. Yumoto, K. Akashi, Y. Ide, Control of preferential orientation of AlN films prepared by the reactive sputtering method, Thin Solid Films. 316 (1998) 152–157. doi:10.1016/S0040-6090(98)00406-4.

[122] H.C. Lee, G.H. Kim, S.K. Hong, K.Y. Lee, Y.J. Yong, C.H. Chun, J.Y. Lee, Influence of sputtering pressure on the microstructure evolution of AlN thin films prepared by reactive sputtering, Thin Solid Films. 261 (1995) 148–153. doi:10.1016/S0040-6090(95)06530-X.

[123] M. Schneider, A. Bittner, F. Patocka, M. Stöger-Pollach, E. Halwax, U. Schmid, Impact of the surface-near silicon substrate properties on the microstructure of sputter-deposited AlN thin films, Appl. Phys. Lett. 101 (2012) 221602. doi:10.1063/1.4768951.

[124] J. Prakash, G. Bose, Aluminum Nitride (AlN) Film Based Acoustic Devices: Material Synthesis and Device Fabrication, Acoust. Waves - From Microdevices to Helioseismology. (2011). doi:10.5772/20840.

[125] Z. Vashaei, T. Aikawa, M. Ohtsuka, H. Kobatake, H. Fukuyama, S. Ikeda, K. Takada, Influence of sputtering parameters on the crystallinity and crystal orientation of AlN layers deposited by RF sputtering using the AlN target, J. Cryst. Growth. 311 (2009) 459–462. doi:10.1016/j.jcrysgro.2008.09.046.

[126] Y. Lu, M. Reusch, N. Kurz, A. Ding, T. Christoph, L. Kirste, V. Lebedev, A. Žukauskaitė, Surface Morphology and Microstructure of Pulsed DC Magnetron Sputtered Piezoelectric AlN and AlScN Thin Films, Phys. Status Solidi. A. 215 (2018) 1700559. doi:10.1002/pssa.201700559.

[127] V.V. Felmetsger, M.K. Mikhov, Reactive sputtering of highly c-axis textured Ti-doped AlN thin films, IEEE Int. Ultrason. Symp. IUS. (2012) 782–785. doi:10.1109/ULTSYM.2012.0195.

[128] R. Deng, P. Muralt, D. Gall, Biaxial texture development in aluminum nitride layers during off-axis sputter deposition, J. Vac. Sci. Technol. A Vacuum, Surfaces, Film. 30 (2012) 051501. doi:10.1116/1.4732129.

[129] F. Martin, P. Muralt, M.A. Dubois, A. Pezous, Thickness dependence of the properties of highly c-axis textured AIN thin films, J. Vac. Sci. Technol. A Vacuum, Surfaces Film. 22 (2004) 361–365. doi:10.1116/1.1649343.

[130] X.H. Xu, H.S. Wu, C.J. Zhang, Z-H. Jin, Morphological properties of AlN piezoelectric thin films deposited by DC reactive magnetron sputtering, Thin Solid Films. 388 (2001) 62–67. doi:10.1016/S0040-6090(00)01914-3.

[131] A. Ababneh, U. Schmid, J. Hernando, J.L. Sánchez-Rojas, H. Seidel, The influence of sputter deposition parameters on piezoelectric and mechanical properties of AlN thin films, Mater. Sci. Eng. B. 172 (2010) 253–258. doi:10.1016/j.mseb.2010.05.026.

[132] H.E. Cheng, T.C. Lin, W.C. Chen, Preparation of [002] oriented AlN thin films by mid frequency reactive sputtering technique, Thin Solid Films. 425 (2003) 85–89. doi:10.1016/S0040-6090(02)01137-9.

[133] D. Depla, R. De Gryse, Target poisoning during reactive magnetron sputtering : Part I the influence of ion implantation, Surf. Coat. Technol. 281 (2003).

[134] E. Iborra, M. Clement, J. Sangrador, A. Sanz-Hervás, L. Vergara, M. Aguilar, Effect of Particle Bombardment on the Orientation and the Residual Stress of Sputtered AlN Films for SAW Devices, IEEE Trans. Ultrason. Ferroelectr. Freq. Control. 51 (2004) 352–358. doi:10.1109/TUFFC.2004.1295415.

[135] M. Akiyama, T. Kamohara, N. Ueno, M. Sakamoto, K. Kano, A. Teshigahara, N. Kawahara, Polarity inversion in aluminum nitride thin films under high sputtering power, Appl. Phys. Lett. 90 (2007) 151910. doi:10.1063/1.2721865.

[136] E. Iborra, M. Clement, J. Capilla, J. Olivares, V. Felmetsger, Low-thickness high-quality aluminum nitride films for super high frequency solidly mounted resonators, Thin Solid Films. 520 (2012) 3060–3063. doi:10.1016/j.tsf.2011.11.007.

[137] A. Sanz-Hervás, M. Clement, E. Iborra, L. Vergara, J. Olivares, J. Sangrador, Degradation of the piezoelectric response of sputtered c-axis AlN thin films with traces of non-(0002) x-ray diffraction peaks, Appl. Phys. Lett. 88 (2006) 161915. doi:10.1063/1.2191425.

[138] S. Fichtner, T. Reimer, S. Chemnitz, F. Lofink, B. Wagner, Stress controlled pulsed direct current co-sputtered $Al_{1-x}Sc_xN$ as piezoelectric phase for micromechanical sensor applications, APL Mater. 3 (2015) 116102. doi:10.1063/1.4934756.

[139] S.J. Abramoff, M.D. Magelhaes, P.J. Ram, Image Processing with ImageJ, Biophotonics Int. 11 (2004) 36–42. doi:10.1117/1.3589100.

[140] M. Moreira, J. Bjurström, I. Katardjev, V. Yantchev, Aluminum scandium nitride thin-film bulk acoustic resonators for wide band applications, Vacuum. 86 (2011) 23–26. doi:10.1016/j.vacuum.2011.03.026.

[141] S. Takayanagi, M. Matsukawa, T. Yanagitani, Shear mode properties of c-axis parallel oriented $Sc_xAl_{1-x}N$ films grown by RF bias sputtering, 2015 IEEE Int. Ultrason. Symp., 2015. 1–4. doi:10.1109/ULTSYM.2015.0537.

[142] F. Tasnádi, B. Alling, C. Höglund, G. Wingqvist, J. Birch, L. Hultman, I.A. Abrikosov, Origin of the Anomalous Piezoelectric Response in Wurtzite ScAlN Alloys, Phys. Rev. Lett. 104 (2010) 137601. doi:10.1103/PhysRevLett.104.137601.

[143] O. Zywitzki, T. Modes, S. Barth, H. Bartzsch, P. Frach, Effect of scandium content on structure and piezoelectric properties of AlScN films deposited by reactive pulse magnetron sputtering, Surf. Coatings Technol. 309 (2017) 417–422. doi:10.1016/j.surfcoat.2016.11.083.

[144] S. Mertin, B. Heinz, O. Rattunde, G. Christmann, M.A. Dubois, S. Nicolay, P. Muralt, Piezoelectric and structural properties of c-axis textured aluminium scandium nitride thin films up to high scandium content, Surf. Coatings Technol. 343 (2018) 2–6. doi:10.1016/j.surfcoat.2018.01.046.

[145] K.R. Talley, S.L. Millican, J. Mangum, S. Siol, C.B. Musgrave, B. Gorman, A.M. Holder, A. Zakutayev, G.L. Brennecka, Implications of heterostructural alloying for enhanced piezoelectric performance of (Al,Sc)N, Phys. Rev. Mater. 2 (2018) 063802. doi:10.1103/PhysRevMaterials.2.063802.

[146] K. Lefki, G.J.M. Dormans, Measurement of piezoelectric coefficients of ferroelectric thin films, J. Appl. Phys. 76 (1994) 1764–1767. doi:10.1063/1.357693.

[147] Y. Lu, M. Reusch, N. Kurz, A. Ding, T. Christoph, M. Prescher, L. Kirste, O. Ambacher, A. Žukauskaitė, Elastic modulus and coefficient of thermal expansion of piezoelectric $Al_{1-x}Sc_xN$ (up to x = 0.41) thin films, APL Mater. 6 (2018) 076105. doi:10.1063/1.5040190.

[148] R. Matloub, M. Hadad, P. Muralt, Piezoelectric coefficients of AlScN thin films in comparison, in: 2016 IEEE Int. Freq. Control Symp. IFCS 2016 - Proc., 2016. 2–3. doi:10.1109/FCS.2016.7546740.

[149] M.A. Moreira, J. Bjurström, V. Yantchev, I. Katardjiev, Synthesis and characterization of highly c-textured $Al_{1-x}Sc_xN$ thin films in view of telecom applications, IOP Conf. Ser. Mater. Sci. Eng. 41 (2012) 012014. doi:10.1088/1757-899X/41/1/012014.

[150] T.K. and T.F. Keiichi Umeda, H. Kawai, A. Honda, M. Akiyama, Piezoelectric properties of ScAlN thin films for piezo-MEMS device BAW fabrication process, MEMS 2013 Taiwan. (2013) 733–736.

[151] J.C. Yang, X.Q. Meng, C.T. Yang, Y. Zhang, Influence of sputtering power on crystal quality and electrical properties of Sc-doped AlN film prepared by DC magnetron sputtering, Appl. Surf. Sci. 287 (2013) 355–358. doi:10.1016/j.apsusc.2013.09.155.

[152] S. Wu, M.Y. Wu, J.L. Huang, D.F. Lii, Characterization and piezoelectric properties of reactively sputtered (Sc, Al)N thin films on diamond structure, Int. J. Appl. Ceram. Technol. 11 (2014) 894–900. doi:10.1111/ijac.12068.

[153] X. Li, Y. Yang, D. Zhou, C. Yang, F. Feng, J. Yang, Q. Hu, Preparation of ScAlN films as a function of power density on Si and flexible substrate by dc reactive magnetron sputtering, J. Mater. Sci. Mater. Electron. (2015) 2–7. doi:10.1007/s10854-015-3733-5.

[154] P.M. Mayrhofer, A. Bittner, U. Schmid, High temperature stability of $Sc_xAl_{1-x}N$ (x=0.27) thin films, Proc. of SPIE, (2015) 95171C. doi:10.1117/12.2178503.

[155] Y. Zhang, W. Zhu, D. Zhou, Y. Yang, C. Yang, Effects of sputtering atmosphere on the properties of c-plane ScAlN thin films prepared on sapphire substrate, J. Mater. Sci. Mater. Electron. 26 (2014) 472–478. doi:10.1007/s10854-014-2423-z.

[156] H. Fukuyama, H. Miyake, G. Nishio, S. Suzuki, K. Hiramatsu, Impact of high-temperature annealing of AlN layer on sapphire and its thermodynamic principle, Jpn. J. Appl. Phys. 55 (2016) 05FL02. doi:10.7567/JJAP.55.05FL02.

[157] A. Žukauskaitė, E. Broitman, P. Sandström, L. Hultman, J. Birch, Nanoprobe mechanical and piezoelectric characterization of $Sc_xAl_{1-x}N$(0001) thin films, Phys. Status Solidi. 212 (2015) 666–673. doi:10.1002/pssa.201431634.

[158] N. Kurz, Y. Lu, L. Kirste, M. Reusch, A. Žukauskaitė, V. Lebedev, O. Ambacher, Temperature Dependence of the Pyroelectric Coefficient of AlScN Thin Films, Phys. Status Solidi. (2018) 1700831. doi:10.1002/pssa.201700831.

[159] J. Menk, Uncertainties and Errors in Nanoindentation, in: Nanoindentation Mater. Sci., InTech, 2012. doi:10.5772/50002.

[160] T.C. Chen, W.J. Lin, D.L. Chen, Effect of temperature gradient on simultaneously experimental determination of thermal expansion coefficients and elastic modulus of thin film materials, J. Appl. Phys. 96 (2004) 3800–3806. doi:10.1063/1.1789629.

[161] R. Knepper, S.P. Baker, Coefficient of thermal expansion and biaxial elastic modulus of β phase tantalum thin films, Appl. Phys. Lett. 90 (2007) 181908. doi:10.1063/1.2734468.

[162] T.F. Retajczyk, A.K. Sinha, Elastic stiffness and thermal expansion coefficients of various refractory silicides and silicon nitride films, Thin Solid Films. 70 (1980) 241–247. doi:10.1016/0040-6090(80)90364-8.

[163] G.G. Stoney, The tension of metallic films deposited by electrolysis, Proc. R. Soc. A Math. Phys. Eng. Sci. 82 (1909) 172–175. doi:10.1098/rspa.1909.0021.

[164] M.A. Hopcroft, W.D. Nix, T.W. Kenny, What is the Young's modulus of silicon?, J. Microelectromechanical Syst. 19 (2010) 229–238. doi:10.1109/JMEMS.2009.2039697.

[165] V. Pishchik, L.A. Lytvynov, E.R. Dobrovinskaya, Sapphire: Material, Manufacturing, Application, Springer US, Boston, MA, 2009. doi:10.1007/978-0-387-85695-7.

[166] Y. Kurokawa, K. Utsumi, H. Takamizawa, T. Kamata, S. Noguchi, A1N Substrates with High Thermal Conductivity, IEEE Trans. Components, Hybrids, Manuf. Technol. 8 (1985) 247–252. doi:10.1109/TCHMT.1985.1136500.

[167] G.A. Slack, S.F. Bartram, Thermal expansion of some diamondlike crystals, J. Appl. Phys. 46 (1975) 89–98. doi:10.1063/1.321373.

[168] C.M. Lin, T.T. Yen, Y.J. Lai, V.V. Felmetsger, M.A. Hopcroft, J.H. Kuypers, A.P. Pisano, Temperature-compensated aluminum nitride lamb wave resonators., IEEE Trans. Ultrason. Ferroelectr. Freq. Control. 57 (2010) 524–32. doi:10.1109/TUFFC.2010.1443.

[169] G. Wingqvist, L. Arapan, V. Yantchev, I. Katardjiev, A micromachined thermally compensated thin film Lamb wave resonator for frequency control and sensing applications, J. Micromechanics Microengineering. 19 (2009) 035018. doi:10.1088/0960-1317/19/3/035018.

[170] V. Lughi, D.R. Clarke, Defect and stress characterization of AlN films by Raman spectroscopy, Appl. Phys. Lett. 89 (2006) 1–4. doi:10.1063/1.2404938.

[171] R. Deng, S.R. Evans, D. Gall, Bandgap in $Al_{1-x}Sc_xN$, Appl. Phys. Lett. 102 (2013) 112103. doi:10.1063/1.4795784.

[172] H. Yao, C.H. Yan, Anisotropic optical responses of sapphire (α-Al2O3) single crystals, J. Appl. Phys. 85 (1999) 6717–6722. doi:10.1063/1.370184.

[173] N. Nepal, K.B. Nam, M.L. Nakarmi, J.Y. Lin, H.X. Jiang, J.M. Zavada, R.G. Wilson, Optical properties of the nitrogen vacancy in AlN epilayers, Appl. Phys. Lett. 84 (2004) 1090–1092. doi:10.1063/1.1648137.

[174] M. Baeumler, Y. Lu, N. Kurz, L. Kirste, T. Christoph, A. Zukauskaite, Oliver Ambacher, Optical constants and bandgap of wurtzite $Al_{1-x}Sc_xN/Al_2O_3$ prepared by magnetron sputter epitaxy for Sc concentration up to x = 0.4, (2019) accepted in Jour. Appl. Phys.

[175] M. Clement, L. Vergara, J. Sangrador, E. Iborra, a. Sanz-Hervás, SAW characteristics of AlN films sputtered on silicon substrates, Ultrasonics. 42 (2004) 403–407. doi:10.1016/j.ultras.2004.01.034.

[176] G. Tang, T. Han, A. Teshigahara, T. Iwaki, K.Y. Hashimoto, Enhancement of effective electromechanical coupling factor by mass loading in layered surface acoustic wave device structures, Jpn. J. Appl. Phys. 55 (2016). doi:10.7567/JJAP.55.07KD07.

[177] A. Ding, M. Reusch, **Y. Lu**, N. Kurz, R. Lozar, T. Christoph, R. Driad, O. Ambacher, and A. Zukauskaite, Investigation of Temperature Characteristics and Substrate Influence on AlScN-Based SAW Resonators, in 2018 IEEE Int. Ultrason. Symp.2018. 1–9. doi: 10.1109/ULTSYM.2018.8579751

[178] H. Ichihashi, T. Yanagitani, M. Suzuki, S. Takayanagi, M. Matsukawa, Effect of Sc concentration on shear wave velocities in ScAlN films measured by micro-Brillouin scattering technique, IEEE Int. Ultrason. Symp. IUS. (2014) 2521–2524. doi:10.1109/ULTSYM.2014.0629.

[179] W. Wang, P.M. Mayrhofer, X. He, M. Gillinger, Z. Ye, X. Wang, A. Bittner, U. Schmid, J.K. Luo, High performance AlScN thin film based surface acoustic wave

devices with large electromechanical coupling coefficient, Appl. Phys. Lett. 105 (2014). doi:10.1063/1.4896853.

[180] G. Tang, T. Han, Q. Zhang, K. Yamazaki, T. Omori, K. Hashimoto, Validity evaluation of Sc x Al 1− x N material constants based on SAW characteristics, J. Micromechanics Microengineering. 26 (2016) 115002. doi:10.1088/0960-1317/26/11/115002.

[181] M. Knapp, R. Hoffmann, V. Lebedev, V. Cimalla, O. Ambacher, Graphene as an active virtually massless top electrode for RF solidly mounted bulk acoustic wave (SMR-BAW) resonators, Nanotechnology. 29 (2018) 105302. doi:10.1088/1361-6528/aaa6bc.

[182] A.S. Mayorov, N. Hunter, W. Muchenje, C.D. Wood, M. Rosamond, E.H. Linfield, A.G. Davies, J.E. Cunningham, Surface acoustic wave generation and detection using graphene interdigitated transducers on lithium niobate, Appl. Phys. Lett. 104 (2014) 083509. doi:10.1063/1.4866273.

[183] E. Climent-Pascual, M. García-Vélez, Á.L. Álvarez, C. Coya, C. Munuera, X. Díez-Betriu, M. García-Hernández, A. De Andrés, Large area graphene and graphene oxide patterning and nanographene fabrication by one-step lithography, Carbon N. Y. 90 (2015) 110–121. doi:10.1016/j.carbon.2015.04.018.

[184] J. Feng, W. Li, X. Qian, J. Qi, L. Qi, J. Li, Patterning of graphene, Nanoscale. 4 (2012) 4883. doi:10.1039/c2nr30790a.

[185] M. Knapp, R. Hoffmann, V. Cimalla, O. Ambacher, Wettability Investigations and Wet Transfer Enhancement of Large-Area CVD-Graphene on Aluminum Nitride, Nanomaterials. 7 (2017) 226. doi:10.3390/nano7080226.

[186] R. Ruby, Review and comparison of bulk acoustic wave FBAR, SMR technology, Proc. - IEEE Ultrason. Symp. (2007) 1029–1040. doi:10.1109/ULTSYM.2007.262.

[187] F. Martin, M.E. Jan, B. Belgacem, M.A. Dubois, P. Muralt, Shear mode coupling and properties dispersion in 8 GHz range AlN thin film bulk acoustic wave (BAW) resonator, Thin Solid Films. 514 (2006) 341–343. doi:10.1016/j.tsf.2006.03.005.

[188] S.G. Yang, A.B. Pakhomov, S.T. Hung, C.Y. Wong, Room-temperature magnetism in Cr-doped AlN semiconductor films, Appl. Phys. Lett. 81 (2002) 2418–2420. doi:10.1063/1.1509475.

[189] S. Manna, K.R. Talley, P. Gorai, J. Mangum, A. Zakutayev, G.L. Brennecka, V. Stevanović, C. V. Ciobanu, Enhanced Piezoelectric Response of AlN via CrN Alloying, Phys. Rev. Appl. 9 (2018) 034026. doi:10.1103/PhysRevApplied.9.034026.

[190] A. Žukauskaite, C. Tholander, J. Palisaitis, P.O. Persson, V. Darakchieva, N. Ben Sedrine, F. Tasnádi, B. Alling, J. Birch, L. Hultman, $Y_xAl_{1-x}N$ thin films, J. Phys. D. Appl. Phys. 45 (2012). doi:10.1088/0022-3727/45/42/422001.

Publications

Journal papers related to this work

1. M. Reusch, S. Cherneva, **Y. Lu**, A. Žukauskaitė, L. Kirste, K. Holc, M. Datcheva, D. Stoychev, V. Lebedev, and O. Ambacher, Microstructure and mechanical properties of stress-tailored piezoelectric AlN thin films for electro-acoustic devices, Appl. Surf. Sci. 407, 307 (2017).
2. **Y. Lu**, M. Reusch, N. Kurz, A. Ding, T. Christoph, L. Kirste, V. Lebedev, and A. Žukauskaitė, Surface Morphology and Microstructure of Pulsed DC Magnetron Sputtered Piezoelectric AlN and AlScN Thin Films, Phys. Status Solidi (A) 215, 1700559 (2018).
3. N. Kurz, **Y. Lu**, L. Kirste, M. Reusch, A. Žukauskaitė, V. Lebedev, and O. Ambacher, Temperature Dependence of the Pyroelectric Coefficient of AlScN Thin Films, Phys. Status Solidi 1700831 (2018).
4. **Y. Lu**, M. Reusch, N. Kurz, A. Ding, T. Christoph, M. Prescher, L. Kirste, O. Ambacher, and A. Žukauskaitė, Elastic modulus and coefficient of thermal expansion of piezoelectric $Al_{1-x}Sc_xN$ (up to x = 0.41) thin films, APL Mater. 6, 076105 (2018).
5. A. Ding, M. Reusch, **Y. Lu**, N. Kurz, R. Lozar, T. Christoph, R. Driad, O. Ambacher, and A. Žukauskaitė, Investigation of Temperature Characteristics and Substrate Influence on AlScN-Based SAW Resonators, in 2018 IEEE Int. Ultrason. Symp. (IEEE, Kobe, 2018), pp. 1–9.
6. N. Kurz, D.F. Urban, A. Ding, **Y. Lu**, L. Kirste, N.M. Feil, A. Žukauskaitė, and O. Ambacher, Experimental determination of the electro-acoustic properties of thin film AlScN using surface acoustic wave resonators (accepted to Journal of Applied Physics 2019).
7. M. Baeumler, **Y. Lu**, N. Kurz, L. Kirste, T. Christoph, A. Žukauskaitė, and O. Ambacher, Optical constants and bandgap of wurtzite $Al_{1-x}Sc_xN/Al_2O_3$ prepared by magnetron sputter epitaxy for Sc concentration up to x = 0.4 (accepted to Journal of Applied Physics 2019).

Conference contributions

1. **Y. Lu**, M. Reusch, A. Žukauskaitė, N. Kurz, L. Kirste, O. Ambacher, and V. Lebedev, Reactive magnetron sputtering of stress-controlled piezoelectric AlScN thin film,
   Oral presentation, DPG spring meeting of the Condensed Matter Section, Mar. 06-11, 2016, Regensburg, Germany
2. **Y. Lu**, M. Reusch, N. Kurz, A. Ding, T. Christoph, L. Kirste, V. Lebedev, and A. Žukauskaitė, Surface Morphology and Microstructure of Pulsed DC Magnetron Sputtered Piezoelectric AlN and AlScN Thin Films,
   Poster, 12th International Conference on Nitride Semiconductors (ICNS12), Jul 24-28, 2017 Strasbourg, France

3. **Y. Lu**, M. Reusch, N. Kurz, A. Ding, T. Christoph, L. Kirste, V. Lebedev, and A. Žukauskaitė, Thermal expansion coefficient and elastic modulus of reactive pulsed-DC magnetron co sputtered piezoelectric AlScN thin films,
   Oral presentation, PiezoMEMS workshop 2018, Jan 15-16, 2018, Orlando, USA
4. **Y. Lu**, M. Reusch, N. Kurz, A. Ding, T. Christoph, L. Kirste, V. Lebedev, and A. Žukauskaitė, Thermal expansion coefficient and elastic modulus of reactive pulsed-DC magnetron co sputtered piezoelectric AlScN thin films,
   Oral presentation, 15th European Vacuum Conference, Jun 17-22, 2018, Geneva, Switzerland

Acknowledgements

First, I would like to express my sincere gratitude to my advisor and mentor Prof. Dr. Oliver Ambacher for the scientific support during my PhD studies. He gave me complete freedom in my path to pursue my research interest, furthermore, the scientific discussion with him is always very inspiring and it makes science so interesting.

My special thanks are dedicated to Dr. Agnė Žukauskaitė. As one of the pioneer in the AlScN with a lot of experience, she gave me lots of practical tips for my PhD study. Furthermore, as a team leader she leads us to seek the excellence and perfection, it is because of this spirit that we could go further and look deeper. I will never forget the motto of our team "Yes, you can!"

I would also like to thank Dr. Markus Reusch for the discussion of the scientific topics as well as the life issues during almost the whole period of my PhD life. He guided me with his all knowledge and passion, it was really a pleasure to cooperate with him to solve some scientific questions.

As an old and current colleague in the Freiburg Materials Research Center and Fraunhofer IAF, I want to say thank you to Dr. Sebastian Schütt. His support for my scientific work as well as the guidance of my life is inspiring me.

Many thanks to Dr. Martina Baeumler, her curiosity and passion for the science inspired me in the further scientific study even my PhD is going to finish. To find, to explore, to dig deeper, they are not the spirits only for the scientists, but for everyone.

Furthermore, I would like to thank Dr. Lutz Kirste and Mario Prescher for carrying out the XRD analysis, measuring and analyzing so many samples always fast and reliable. Also as an old colleague of the Uni-Freiburg Crystallography Institute, I can share so much old times during my master period with Lutz.

Without Robert Iannucci and Dr. Christian Giese I could never learn how to use the SEM properly without destroying it, thank you for your tolerance.

Unforgettable time with Dr. Fang Gao and Dr. Taro Yoshikawa was great, we had so many good memories when we were in the same department as PhD students. I hope all of us could have a great life and bright future, and thank you for those moments.

I would like to thank the PiTrans team, T. Christoph, A. Ding, N. Kurz and N. Feil. It is an honor to work with you guys, and all of you are very talented scientists. This work could not be achieved without your help.

Additionally, I want to thank all my colleagues, at Fraunhofer IAF for the fruitful and interesting discussions. Also during the team building activities and lunch time we had a lot of great memories and moments.

Finally, I would like to thank my friends in Freiburg and my family in Shanghai, China for supporting my studies in Germany from master to PhD; especially to my girlfriend Joyce, for the unconditional support of my PhD during the times of depression and difficulties.